

Characterisation of the Background in the KATRIN Experiment

(Charakterisierung des Untergrunds im
KATRIN Experiment)

Master thesis
of

Fabian Block

at the Institute of Experimental Particle Physics (ETP)

Reviewer:	Prof. Dr. G. Drexlin
Second Reviewer:	Prof. Dr. G. Quast
Advisor:	Dr. F. M. Fränkle
Second Advisor:	M.Sc. M. Machatschek
Third Advisor:	Dr. F. Harms

10.04.2017 – 10.04.2018

Erklärung zur Selbstständigkeit

Ich versichere, dass ich diese Arbeit selbstständig verfasst habe und keine anderen als die angegebenen Quellen und Hilfsmittel benutzt habe, die wörtlich oder inhaltlich übernommenen Stellen als solche kenntlich gemacht und die Satzung des KIT zur Sicherung guter wissenschaftlicher Praxis in der gültigen Fassung vom 27.11.2014 beachtet habe.

Karlsruhe, den 06.04.2018, _____
Fabian Block

Als Ansichtsexemplar genehmigt von

Karlsruhe, den 06.04.2018, _____
Prof. Dr. G. Drexlin

Abstract

Neutrinos are electrically neutral particles, which exist in a large density in the universe as relics from the big bang (336 cm^{-3} [LP12]). They are assumed massless in the standard model of particle physics. In contrast, the discovery of neutrino oscillation requires that at least two of the three neutrino mass eigenstates have a non-vanishing rest mass. The access to the absolute neutrino mass scale is of high interest for cosmology, particle and astroparticle physics, however oscillation experiments only allow for the investigation of the difference of the squared masses of the neutrino mass eigenstates. The **K**arlsruhe **T**ritium **N**eutrino experiment (KATRIN) is a large-scale tritium β -decay experiment to determine the effective mass of the electron antineutrino. A high-luminosity windowless gaseous tritium source paired with a high-resolution MAC-E filter enables the precise spectroscopy of the β -electrons at the endpoint of tritium. KATRIN aims to push the existing limits on the effective neutrino mass from 2.05 eV^1 (95 % CL) [P⁺16] to an unprecedented sensitivity of 0.2 eV (90 % CL) [KAT05].

To achieve this sensitivity, it is of fundamental importance to determine the statistical and systematic uncertainties of KATRIN. By analysing multiple commissioning measurement phases, this thesis contributes to the quantification of the following sources of systematic uncertainties: rate estimation with the KATRIN detector, retarding potential dependence of the background rate near the endpoint of tritium and misalignments of KATRIN components relative to the detector. Additionally, the background rate as dominant component of the statistical uncertainty is characterised in the context of this thesis.

Pile-up, charge-sharing and backscattering of electrons at the detector cause a systematic uncertainty on the estimation of the rate. By applying different rate estimation methods on the data of the 2017 krypton campaign, the systematic uncertainty of rate estimation is determined to be between 5.89 % and 0.32 % for a rate range of 10 to 10^4 cps.

The influence of a voltage dependence of the main spectrometer background rate near the endpoint of tritium on the squared neutrino mass is investigated. Results of a long-term measurement indicate a background rate dependence of 10 mcps/keV , which might be explained by changing storage conditions for background electrons with varying retarding potential. The rate dependence causes a systematic uncertainty on the squared neutrino mass of 0.015 eV^2 , which is nearly as large as the total KATRIN systematic uncertainty budget of 0.017 eV^2 [KAT05]. However, sensitivity studies performed in this thesis, which are based on the latest background measurements, show that the KATRIN sensitivity is dominated by the statistical uncertainty due to an elevated background rate compared to the design report assumption. As a consequence, the influence of a voltage dependence of the main spectrometer background rate near the endpoint of tritium on the sensitivity is below 3 meV . However, an up to now unexplained significant increase of the total background rate of 30 mcps and a corresponding change of the voltage dependence indicate, that some of the background characteristics are currently not reproducible. Consequently,

¹In the context of this thesis natural units ($\hbar = c = 1$) are used.

the given sensitivity estimates can only be valid for the analysed measurements, however, the necessary tools and models for future analyses have been stated in this thesis.

Background properties are characterised in an electric and 6 G magnetic field setting similar to the one used in future neutrino mass measurements. Compared to the 6 G measurement, former background measurements show 23 % less volume-normalised rate for the flux tube of the 6 G setting.

Hypothesis tests indicate an instability of the rate on small time scales, which cannot entirely be explained by statistical fluctuations. Furthermore, the rate instability does not seem to be random in its time development, however the distribution of the total measured rate can be described by a Poissonian. The time development and large fluctuations cannot be explained by instabilities of the relevant hardware parameters, which are shown to fulfil the required stability criteria during the two weeks of the long-term measurement.

Two existing methods to quantify the alignment of the magnetic flux tube and the inner electrode comb structure relative to the detector are applied on the data of the recent measurement phase. In addition, a new method to determine the misalignment of the spectrometer vessel relative to the detector is developed in the course of this thesis.

All tested components show significant misalignments, which need to be taken into account for the neutrino mass measurements. The centre of the flux tube on the detector is shifted by (1.7 ± 0.1) mm relative to the detector centre, the inner electrode system by (2.8 ± 0.1) mm. The misalignment of the spectrometer vessel relative to the detector amounts to a shift of (58.5 ± 0.3) cm, measured in the analysing plane of the main spectrometer.

Contents

Abstract	v
1. Neutrino Physics	1
1.1. The Postulation and Discovery of Neutrinos	1
1.1.1. The Project Poltergeist Experiments	1
1.1.2. Discovery of ν_μ and ν_τ	2
1.2. Neutrinos in the Standard Model of Particle Physics	2
1.3. Neutrino Oscillation	4
1.3.1. Theory of Neutrino Oscillation	4
1.3.2. Experimental Investigation of Neutrino Oscillation	5
1.4. Determination of the Neutrino Mass	8
1.4.1. Time-of-Flight Measurements of Supernovae	8
1.4.2. Cosmological Limits	9
1.4.3. Neutrino-Less Double β -Decay	10
1.4.4. Single β -Decay	11
2. The KATRIN Experiment	15
2.1. The Source and Transport Section	15
2.1.1. Rear Section	15
2.1.2. Windowless Gaseous Tritium Source	15
2.1.3. Transport Section	17
2.2. The Spectrometer and Detector Section	18
2.2.1. Operating Principle of MAC-E Filters	18
2.2.2. Pre-Spectrometer	20
2.2.3. Main Spectrometer	20
2.2.4. Monitor Spectrometer	21
2.2.5. Focal Plane Detector	21
2.3. Neutrino Mass Analysis with KATRIN	21
2.3.1. Confidence Interval and Level	22
2.3.2. Region-of-Interest Cut	22
2.3.3. KATRIN Likelihood	23
2.3.4. Statistical and Systematic Uncertainty Budget	24
3. Systematic Uncertainties of Rate Estimation	27
3.1. Conversion Electrons of ^{83m}Kr	27
3.2. Physics Processes and Read-Out Artefacts in the Focal Plane Detector	28
3.3. Methods for Rate Estimation	29
3.3.1. Event Counting Divided by Measurement Time	29
3.3.2. Determination via Multiplicity Plot	30
3.3.3. Determination via Inter-Arrival Time Distribution	30
3.3.4. Comparison of the Methods	30

3.4.	Systematic Uncertainties without Region-of-Interest Cut	32
3.4.1.	Ratio for Rates below 100 cps	34
3.4.2.	Ratio for Rates higher than 10 kcps	35
3.4.3.	Summarising Table	36
3.5.	Systematic Uncertainties in the Region of Interest	37
3.5.1.	Summarising Table	39
3.6.	Underestimation of the Rate by R1 below 100 cps	39
3.7.	Conclusions	39
4.	The KATRIN Background Model	41
4.1.	Magnetically Stored Electrons	42
4.2.	Cosmic Muons	43
4.3.	Penning Traps	43
4.4.	Radon Decay	44
4.5.	Natural Radioactivity	45
4.6.	Rydberg Atoms	45
4.7.	Intrinsic Detector Background	46
4.8.	Conclusions	47
5.	Voltage Dependence of the Main Spectrometer Background near the End-point of Tritium	49
5.1.	Voltage Dependence in the Design Report	49
5.2.	Model for Voltage Dependence	50
5.3.	Measurement of October 2017	53
5.4.	Measurements of January 2018	54
5.4.1.	Experimental Results	54
5.4.2.	Possible Explanations for Inconsistencies in the January Measurements	56
5.5.	Methods to Treat the Voltage Dependence and the Influence on the Sensitivity	58
5.5.1.	Neglecting Voltage Dependence	58
5.5.2.	Including Voltage Dependence as Fixed Value	60
5.5.3.	Treating Voltage Dependence as Free Fit Parameter	61
5.5.4.	Comparison of Sensitivity	63
5.6.	Conclusions	64
6.	Investigation of SDS-IIIc Long-Term Background Measurement	67
6.1.	Background Rate in the Electron ROI	67
6.1.1.	Comparison with Former Background Measurements	67
6.1.2.	Time Development and Statistical Model of the Rate	70
6.2.	Correlation of Rate with Slow-Control Parameters	73
6.3.	Energy Spectrum	74
6.4.	Pixel Distribution	76
6.4.1.	Pixel Distribution in the Ion ROI	77
6.4.2.	Pixel Distribution in the Electron ROI	78
6.5.	Conclusions	81
7.	Alignment Studies	83
7.1.	Alignment of the Flux Tube	83
7.2.	Alignment of the Retarding Potential	86
7.3.	Alignment of the Main Spectrometer Vessel	88
7.3.1.	Quantification of Misalignment	88
7.3.2.	Cross-Check with Background Model	91
7.4.	Conclusions	92

8. Summary and Outlook	95
Appendix	97
A. Background in Measurements with the Condensed Krypton Source	97
A.1. The Condensed Krypton Source	97
A.2. Background Rate with Injected CKrS	97
A.3. Long-term Background Investigation	100
A.4. Background after Extraction of CKrS	101
A.5. Conclusions	104
B. KATRIN Numbers of Slow-Control Parameters	105
Bibliography	107
Acknowledgements	121

List of Figures

1.1.	The standard model of particle physics.	3
1.2.	The simulated solar neutrino flux plotted versus the neutrino energy.	6
1.3.	Flux of ^8B solar neutrinos of muon and tau flavour versus electron flavour, measured with SNO	7
1.4.	Possible mass hierarchies of neutrinos	9
1.5.	Feynman graph and expected decay spectrum for the neutrino-less double β -decay.	11
1.6.	Simulated decay spectrum of the single β -decay for several neutrino masses.	12
2.1.	The schematical KATRIN set-up with an overview of applied magnetic field and retarding potential	16
2.2.	Schematical operating principle of the main spectrometer	18
2.3.	Measurement time distribution for the integrated β -spectrum	25
3.1.	Decay scheme of ^{83}Rb into ^{83}Kr	28
3.2.	Two methods to estimate the rate shown by example for run 33015	30
3.3.	Rate estimation for run 33144	31
3.4.	Ratios R1/R2 versus the estimated rate	33
3.5.	Distribution of ratios R1/R2 for each order of magnitude of the rate	33
3.6.	Distribution of ratios R1/R2 for rates below 100 cps after exclusion of the outer detector rings	34
3.7.	The ratio plotted versus the rate for rates above 10 kcps with applied multi-pixel cut	35
3.8.	Ratios R1/R2 versus the estimated rate with applied ROI cut	37
3.9.	Distribution of ratios R1/R2 for each order of magnitude of the rate with applied ROI cut	38
3.10.	The probability for backscattering and charge-sharing for different electron energies	40
4.1.	Overview of the known sources of background in the main spectrometer.	41
5.1.	The background electron energy spectrum in the main spectrometer, determined in dipole measurements	50
5.2.	θ_{max} as function of kinetic energy and retarding potential (upper graph), dependence of θ_{max} on the retarding potential for electron energies at 1.5 eV (lower graph).	52
5.3.	Background Rate versus retarding potential	53
5.4.	Difference of the maximally allowed polar emission angle for background electrons between the October and January measurements.	54
5.5.	Measurements of background dependence on the retarding potential, measured at beginning (upper graph) and end (middle graph) of January '18. The lower line shows both rates in one graph for better comparison	55

5.6.	The estimated squared neutrino mass, if the data contains a voltage dependent background, which is not considered in the background model	58
5.7.	Shift on the squared neutrino mass for 10^3 data sets with different background slopes and an assumed fixed slope in the model	60
5.8.	Correlation matrix of the five parameters fit for the normal (upper graph) and adapted run-time schedule (lower graph)	62
5.9.	Normal measurement time distribution for a four parameters fit (upper graph) and an adapted one for the five parameters fit (lower graph)	63
6.1.	Ring-wise rate normalised with the sensitive flux tube volume plotted versus the radius in the analysing plane	68
6.2.	Measured rate in the electron ROI versus time for the SDS-IIIc long-term background measurement	70
6.3.	Multiplicity plot of the SDS-IIIc long-term background rate fitted with a Poisson distribution	72
6.4.	Energy spectrum of the SDS-IIa long-term background measurement (blue line) and corrected for the intrinsic detector background (black points) . . .	75
6.5.	Energy spectrum of the SDS-IIIc long-term background measurement (blue line) and corrected for the intrinsic detector background (black points) . . .	76
6.6.	Rate distribution in the ion ROI after correcting for the intrinsic detector background	77
6.7.	Energy spectrum of the SDS-IIIc long-term background measurement of pixel 8 (red) and pixel 10 (blue) after correcting for the intrinsic detector background	78
6.8.	Rate distribution in the electron ROI after correcting for the intrinsic detector background	79
6.9.	Energy spectrum of the SDS-IIIc long-term background measurement of pixel 128 (red) and pixel 140 (blue) after correcting for the intrinsic detector background	79
6.10.	Azimuth angle distribution of the SDS-IIIc long-term background measurement	80
7.1.	Trajectory of trapped electrons in the main spectrometer	84
7.2.	Inter-arrival time distribution for a high pressure measurement with warm baffles in the electron ROI	85
7.3.	Positions of the centres of the fitted radon rings	86
7.4.	Ring structure on the detector due to secondary electron emission from the inner electrode comb structure	87
7.5.	Positions of the centres of the circles of the inner electrode comb structure .	87
7.6.	Pixel distribution of the SDS-IIa long-term background measurement (upper graph) and corresponding azimuth angle distribution (lower graph)	89
7.7.	Pixel distribution of the shifted background (upper graph) and corresponding azimuth angle distribution (lower graph)	92
A.1.	Overview plots for run 33497	98
A.2.	Rate versus time for both ROI during the extraction of the CKrS from the beamline	99
A.3.	Ring-wise background rate versus time	100
A.4.	Behaviour of background in the first two hours after the extraction of the CKrS	102
A.5.	Overview plots for run 33302-33311 (2-11 hours after extraction of CKrS from the beamline)	103

List of Tables

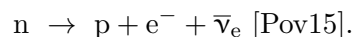
3.1. Estimated systematic uncertainties without ROI cut	32
3.2. Estimated systematic uncertainties without ROI cut for several applied analysis tools	36
3.3. Estimated systematic uncertainties with ROI cut for several applied analysis tools	38
5.1. Analysis of slow-control parameters during the January measurements . . .	57
5.2. Fit results of the squared neutrino mass versus the background slope δ for different background rates	59
5.3. Comparison of sensitivity for the three different methods to treat the slope	64
6.1. Analysis of slow-control parameters during the SDS-IIIc long-term back- ground measurement	74
B.1. Slow-control parameters and the corresponding KATRIN number	105

1. Neutrino Physics

This chapter presents the scientific basis of neutrino physics and the resulting motivation to perform the “Karlsruhe Tritium Neutrino Experiment”. Chapter 1.1 summarises the postulation of the neutrinos and first experiments to prove their existence. The following chapter 1.2 analyses the role of neutrino in the standard model of particle physics. Neutrino oscillation as the experimental proof for a non-vanishing neutrino mass is stated in chapter 1.3. Chapter 1.4 presents several efforts to access the absolute mass scale of neutrinos

1.1. The Postulation and Discovery of Neutrinos

Nuclei with a large surplus of neutrons often convert a neutron into a proton to get to a more favourable lower energetic ground-state. This process is the so-called β^- -decay [Pov15], which was discovered by Rutherford in 1899. Bohr found, that the nucleus ejects an electron in the β^- -decay. Until 1914, it was believed that the β^- -decay was a two body decay of a neutron decaying into a proton and an electron. In 1914, Chadwick measured a continuous β^- -spectrum [Cha14], which could not be unified with the theory of a two body decay and energy conservation [Sue15][MP04]. In 1930, Pauli proposed in a letter the idea of a neutral particle of spin half, which is emitted during the β^- -decay. The additional particle would save the principle of energy conservation [PKW64]. Fermi, who was the first to write down a theoretical form of the β -decay, named this neutral particle neutrino (ν). The β -decay is described in the Fermi theory as a point-like interaction via the weak force [Fer34]. Consequently, the β^- decay can be described as a conversion of a neutron (n) in a proton (p) under the emission of an electron (e^-) and an electron-antineutrino ($\bar{\nu}_e$):



The neutrino was experimentally found by Reines and Cowan in the so-called “Project Poltergeist” experiments in 1956 [Rei97].

1.1.1. The Project Poltergeist Experiments

Based on the Fermi theory, Bethe and Peierls [BP34] suggested that a free neutrino would interact with matter via the inverse β -decay



The Project Poltergeist experiments used a fission reactor as an intense antineutrino source, since the cross-section of the inverse β -decay is small. A liquid scintillator detector interspaced with a water target should detect the inverse β -decay of the antineutrino with a proton of the water target. Following equation 1.1, this interaction produces a neutron and a positron. The positron annihilates with an electron into two γ -rays shortly after its creation. The γ -rays initiate a cascade of electrons that cause the detector material to scintillate. The emitted free neutron of the inverse β -decay wanders around until it is

caught by a nucleus of the detector material. Cadmium was added to the detector material to increase the probability of capturing the neutron. 9 MeV of binding energy is emitted in form of γ rays in the neutron capture process. The γ rays indirectly produce visible light in the detector material a few microseconds later than the first flash of light by the positron-electron-annihilation. This delayed coincidence signature of the inverse β -decay (two flashes of light within a well-known energy range) enables an effective discrimination from background events.

Two experiments were performed with this method until the experimental discovery of the neutrino. The first one was the Hanford Experiment and the second one the Savannah River Experiment. Cosmic rays, which produced neutrino like signals in the experimental set-up, caused problems in the Hanford experiment. The Savannah River experiment used an updated experimental set-up, which allowed a further reduction of background events. The analysis of the measured data determined a significant difference in neutrino-like events when the reactor was on versus when it was off: the antineutrino was found. The experimental cross-section for the inverse β -decay was in accordance with the theoretical prediction of $6.3 \times 10^{-44} \text{ cm}^2$ [Rei97].

1.1.2. Discovery of ν_μ and ν_τ

In 1961, an experiment by Lederman, Schwartz and Steinberger discovered a second type of neutrinos, the muon neutrino ν_μ . A synchrotron accelerated a proton beam towards a target. A shower of boosted π -mesons was produced in the collision. The π -mesons were guided towards a steel wall and decayed in-flight into muons (ν) and muon neutrinos:

$$\pi \rightarrow \mu + \nu_\mu \text{ [Sue15].} \quad (1.2)$$

The steel wall absorbed the muons, whereas the neutrinos passed through it. The muon neutrinos produced muons in an aluminium target, which was placed behind the steel wall. By demonstrating that the induced tracks were caused by muons and not electrons, the existence of a second kind of neutrinos was proven. Lederman, Schwartz and Steinberger received the nobel price in physics for the discovery of the muon neutrino in 1988 [DGG⁺62].

In 1997, the DONut experiment at Fermilab used a 800 GeV proton beam to produce D_s mesons, which decayed in-flight in a tau-lepton τ and tau-neutrino ν_τ . A shielding absorbed the τ , whereas the ν_τ reached the detector behind it. A small number of neutrinos interacted with the detector. Due to its small lifetime, the resulting τ could not be measured directly, but via the location of vertices and the energy of the decay leptons. Nine ν_τ -induced events were measured for an estimated background of 1.5 events, proving the existence of the ν_τ in 2000 [KUA⁺08].

The measured width of the neutral intermediate boson of the weak force (the Z^0) excludes the existence of a further light neutrino [AAA⁺89].

1.2. Neutrinos in the Standard Model of Particle Physics

The standard model of particle physics (see figure 1.1) explains most of the effects in particle physics. It comprises the theory of three elementary interactions: the strong, the electromagnetic and the weak force. The forces are mediated by gauge bosons, which are spin-1 particles. The known particles in the standard model can be distinguished in fermions (spin-half) and bosons (integer spin). The fermions are grouped in three generations, according to their mass and can further be divided in quarks and leptons. As neutrinos have spin-half, they are fermions. Each fermion has a corresponding antifermion, with same mass but opposite electric charge. Neutrinos interact only via the weak force and are therefore leptons.

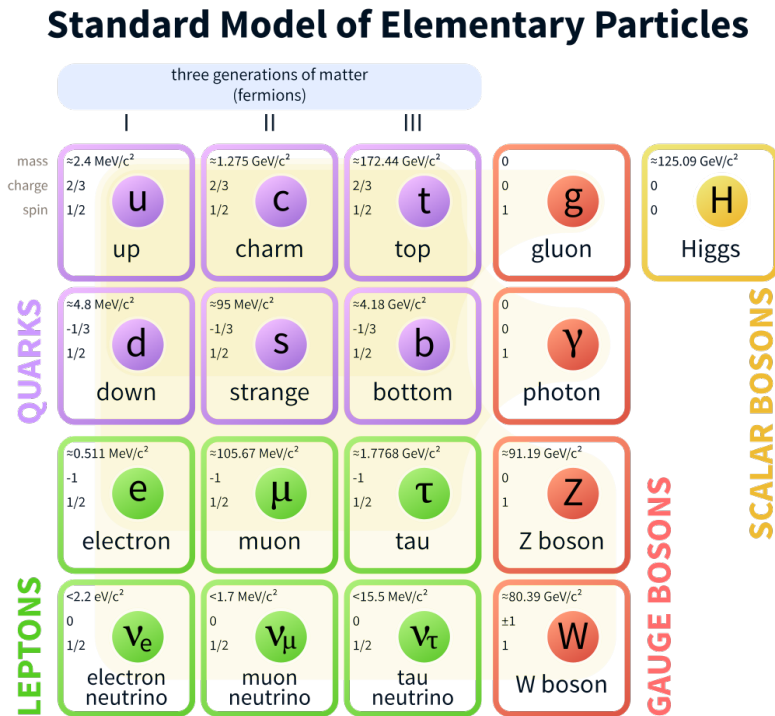


Figure 1.1.: The standard model of particle physics. The quarks (purple) and leptons (green) can be distinguished in three generations depending on their mass. The strong, weak and electromagnetic forces are mediated by the gauge bosons (red). The mass generation of all particles is assumed to be caused by the Higgs boson (yellow) [Wik06].

The W^\pm and Z boson mediate the weak force. The handedness of a particle is important for a coupling to these bosons. The handedness describes the spin orientation (parallel or anti-parallel) relative to its momentum. The gauge bosons of the weak force interact with left-handed particles and right-handed antiparticles. A change of the handedness is only allowed for massive particles via a coupling to the Higgs field, yet this change is suppressed proportional to particle mass divided by its momentum. As the neutrinos are assumed to be massless in the standard model, only a coupling to left-handed neutrinos and right-handed antineutrinos is described [Mar80] [Wei67].

The mass of the particles is expected to be generated via the Higgs mechanism [Hig64], which predicts the spin-0 Higgs boson as quantum excitation of the Higgs field. The Higgs boson couples to all particles with strength proportional to their mass [Pov15].

However, the standard model does not explain all observations in particle physics. In these observations often neutrinos are involved which underlines their key role in physics beyond the standard model.

As mentioned above, the standard model predicts neutrinos as massless. By discovering neutrino flavour oscillation (see chapter 1.3), it is shown, that at least two of the three neutrino generations mass eigenstates possess mass. Nevertheless, the resulting lepton mixing can be described similar to the quark mixing without giving up the standard model [Pov15]. As a consequence of this, the existence of a right-handed sterile neutrino is theoretically allowed [KMMS13].

The electron neutrino has a mass of at least six orders of magnitude smaller than its charged partner, the electron. The electron gains its mass by coupling to the Higgs field. In case of the neutrino there might be further processes responsible for the small mass [Pov15].

Experiments in the search for the neutrino-less double β -decay can answer this question (see chapter 1.4.3).

1.3. Neutrino Oscillation

The discovery of neutrino flavour oscillation implies, that neutrinos have to possess mass. Chapter 1.3.1 gives an overview of the theory of neutrino oscillation for a better understanding of this implication. The ensuing chapter 1.3.2 summarises milestones in the experimental investigation of neutrino oscillation.

1.3.1. Theory of Neutrino Oscillation

Pontecorvo formulated mid of the 20th century the theoretical possibility of neutrino-antineutrino oscillations [Pon68]. Maki, Nakagawa and Sakata proposed flavour mixing of two generations of neutrinos based on the theory of Pontecorvo in 1962 [MNS62]. Neutrino flavour oscillation is the consequence of this proposal. The fundamental assumption of neutrino oscillation is, that flavour states of neutrinos are not equal their mass states. However, the flavour states can be written as an orthogonal linear combination of the mass states

$$\begin{pmatrix} \nu_e \\ \nu_\mu \\ \nu_\tau \end{pmatrix} = \underline{U} \cdot \begin{pmatrix} \nu_1 \\ \nu_2 \\ \nu_3 \end{pmatrix} \quad (1.3)$$

with \underline{U} as the so-called PMNS-matrix [Pov15]. In the following paragraph only two neutrino flavours will be considered for a simplification of the theory of neutrino oscillation.

Two Neutrino Flavour Oscillation

In the assumption of only two neutrino generations, equation 1.3 simplifies to

$$\begin{pmatrix} \nu_e \\ \nu_\mu \end{pmatrix} = \begin{pmatrix} \cos \theta & \sin \theta \\ -\sin \theta & \cos \theta \end{pmatrix} \cdot \begin{pmatrix} \nu_1 \\ \nu_2 \end{pmatrix} .$$

with θ as the mixing angle between flavour and mass states. The electron neutrino flavour is written as a superposition of the mass eigenstates ν_1 and ν_2

$$|\nu_e\rangle = \cos \theta |\nu_1\rangle + \sin \theta |\nu_2\rangle .$$

By applying the time evolution operator $\exp(-itH/\hbar)$ with H as Hamiltonian [CFKS09], the time evolution of the electron neutrino flavour is calculated to

$$|\nu_e(t)\rangle = \exp(-itE_{\nu_1}/\hbar) \cos \theta |\nu_1\rangle + \exp(-itE_{\nu_2}/\hbar) \sin \theta |\nu_2\rangle . \quad (1.4)$$

The neutrino energy E_{ν_i} is approximated to

$$E_{\nu_i} = \sqrt{p^2 c^2 + m_{\nu_i}^2 c^4} \approx pc \left(1 + \frac{1}{2} \frac{m_{\nu_i}^2 c^4}{p^2 c^2} \right) \quad (1.5)$$

with p as the momentum of the neutrino and m_{ν_i} as the mass of the neutrino mass eigenstate ν_i .

The probability to find a neutrino, which was produced in electron flavour, after time t in the same flavour state is $P(\nu_e \rightarrow \nu_e) = |\langle \nu_e(t) | \nu_e \rangle|^2$. By inserting the approximation 1.5 in equation 1.4, the probability $P_{\nu_e \rightarrow \nu_e}$ is calculated to

$$P(\nu_e \rightarrow \nu_e) = 1 - \sin^2 2\theta \sin^2 \left(\frac{1}{4} \frac{\Delta m_{21}^2 c^4}{\hbar c} \frac{L}{pc} \right)$$

with $L = ct$ as the distance between production and detection of the neutrino. $\Delta m_{21}^2 = m_{\nu_2}^2 - m_{\nu_1}^2$ is the difference of the squared masses of the neutrino eigenstates. The probability that an electron neutrino becomes a muon neutrino through oscillation is consequently

$$P(\nu_e \rightarrow \nu_\mu) = 1 - P(\nu_e \rightarrow \nu_e) = \sin^2 2\theta \cdot \sin^2 \left(\frac{1}{4} \frac{\Delta m_{21}^2 c^4 L}{\hbar c pc} \right). \quad (1.6)$$

A neutrino flavour oscillation is thus only possible if the mixing angle between the neutrino flavour states and mass states is non-zero and if the neutrino mass eigenstates have different masses [Pov15] [Sue15].

Three Neutrino Flavour Oscillation

If three neutrino generations are considered, the PMNS-matrix is

$$\underline{U} = \begin{pmatrix} c_{12}c_{13} & s_{12}c_{13} & s_{13}e^{-i\delta} \\ -s_{12}c_{23} - c_{12}s_{23}s_{13}e^{i\delta} & c_{12}c_{23} - s_{12}s_{23}s_{13}e^{i\delta} & s_{23}c_{13} \\ s_{12}s_{23} - c_{12}s_{23}s_{13}e^{i\delta} & -c_{12}s_{23} - s_{12}c_{23}s_{13}e^{i\delta} & c_{23}c_{13} \end{pmatrix}$$

with $c_{ij} = \cos \theta_{ij}$ and $s_{ij} = \sin \theta_{ij}$. The PMNS-matrix contains three mixing angles and one CP violating phase δ . Assuming relativistic neutrinos and CP conservation, the transition probability can be written to

$$P(\nu_\alpha \rightarrow \nu_\beta) = \sum_i |U_{\beta i}|^2 |U_{\alpha i}|^2 + \text{Re} \sum_{i \neq j} U_{\beta i} U_{\beta j}^* U_{\alpha i}^* U_{\alpha j} \exp(-it\delta m_{ij}^2/2E).$$

A three neutrino generation oscillation problem can usually be approximated to a two neutrino generation oscillation due to various mass differences between the neutrino mass eigenstates [Zub98].

1.3.2. Experimental Investigation of Neutrino Oscillation

The first experimental result, which pointed towards neutrino oscillation, was the reduced electron neutrino flux in the so-called ‘‘Solar Neutrino Problem’’ [Pov15].

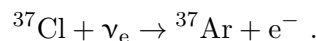
The Solar Neutrino Problem

The sun produces energy via a thermonuclear reactor chain. The standard solar model by Bahcall assumes, that 98 % of the energy is produced in the net reaction



A spectrum of neutrinos arises via several intermediate steps of the net reaction 1.7 (see figure 1.2). The neutrino flux from the sun was measured by different experiments to test the standard solar model [Bah94].

The Homestake experiment in the Homestake Mine was a radiochemical detector for measuring solar neutrinos. The neutrinos were detected via the inverse β -decay with ${}^{37}\text{Cl}$



The threshold for this reaction is 814 keV [Bah94], therefore the detector was sensitive especially to ${}^7\text{Be}$ and ${}^8\text{B}$ neutrinos (see figure 1.2). The ${}^{37}\text{Cl}$ was dissolved in perchloroethylene (C_2Cl_4). After the inverse β -decay, a helium purge removed the ${}^{37}\text{Ar}$ from the tank. The argon atoms were captured and loaded in a proportional counter. The number of decaying

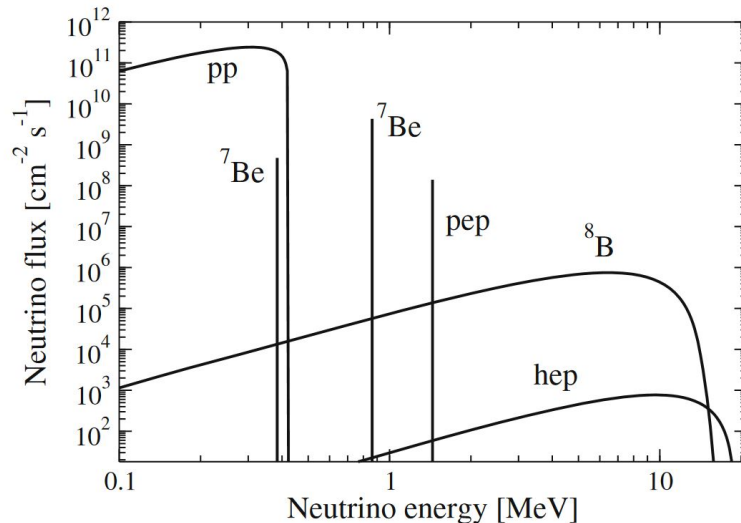


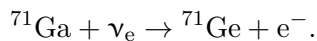
Figure 1.2.: The simulated solar neutrino flux plotted versus the neutrino energy. The neutrinos are produced in a thermonuclear reactor chain by which the sun produces energy as predicted in the standard solar model by John Bahcall [Pov15].

^{37}Ar atoms via electron capture and subsequent emission of an Auger electron was counted [RCDJ85]. The determined flux after 2.5 years of measurement is

$$\Phi = (2.55 \pm 0.17 \pm 0.18) \text{ SNU}^1 .$$

The standard solar model expects a rate of (6.4 ± 1.4) SNU for the Homestake experiment [VBN⁺16]. Other radiochemical experiments with higher sensitivity took place, to test if the reduced neutrino flux was an experimental error.

SAGE and Gallex were two radiochemical experiments, based on the inverse β -decay



The threshold of this reaction is 233 keV. Therefore both experiments measured a part of the pp-neutrino spectrum (see figure 1.2) [AHH⁺92]. The expected measured rate for the radiochemical experiments with gallium is (132 ± 7) SNU [Hax95]. The measured rates by SAGE

$$\Phi = (69 \pm 11 \pm 6) \text{ SNU [VBN}^+16]$$

and also by Gallex

$$\Phi = (79 \pm 10 \pm 6) \text{ SNU [AHH}^+94]$$

are approximately a factor two smaller than the theoretically predicted ones. Both gallium experiments confirm the reduced flux of solar electron neutrinos.

The Sudbury Neutrino Experiment (SNO) solved the solar neutrino problem at the beginning of the 21th century. SNO was the first experiment, which was sensitive to all neutrino flavours. The aim of SNO was to detect the ^8B solar neutrinos through three types of reactions with deuterium: charged current (CC, exchange of W^\pm boson), neutral current (NC, exchange of Z^0 boson) and elastic scattering (ES)



¹Solar Neutrino Unit

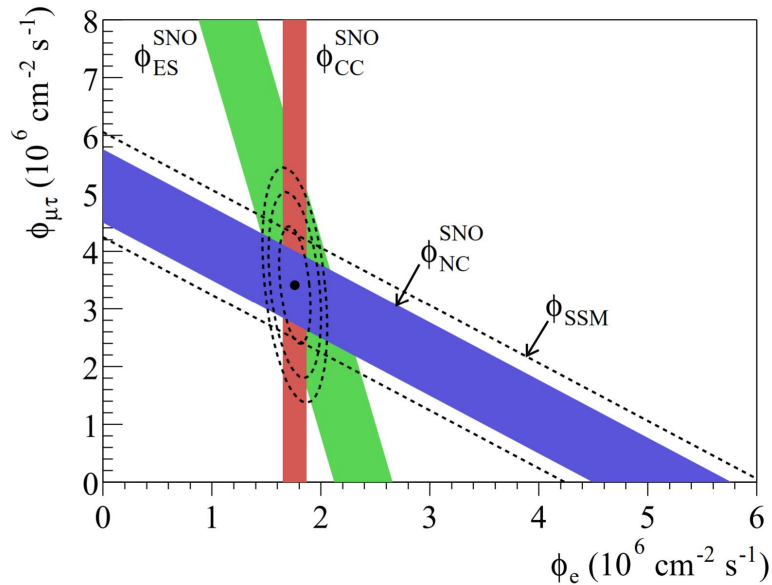


Figure 1.3.: Flux of ^8B solar neutrinos of muon and tau flavour versus electron flavour, measured with SNO. The green band is the flux, induced by elastic scattering (sensitive to all flavours, preferably electron), the red band is the charge current reaction (sensitive to electron flavour) and the blue band is the flux in the neutral current reactions (equally sensitive to all flavours). The dashed line is the flux as predicted by the solar standard model. At the intersection point (black star) the fraction of neutrinos which underwent oscillation can be estimated [AAA⁺02].

Reaction 1.9 and 1.10 are sensitive to all neutrino flavours, whereas 1.8 can only measure electron neutrinos. After approximately 306 days of data taking between 1999 and 2001, the reactions were resolved in electron neutrino induced and muon or tauon induced reactions

$$\begin{aligned}\Phi_e &= (1.76 \pm 0.05 \pm 0.09) \text{ SNU} \\ \Phi_{\mu,\tau} &= (3.41 \pm 0.45 \pm 0.46) \text{ SNU} .\end{aligned}$$

The flux $\Phi_{\mu,\tau}$ is statistically significant above zero and thus giving strong evidence for flavour oscillation of solar electron flavoured neutrinos [AAA⁺02]. The neutral current reaction is equally sensitive to all neutrino flavours and therefore measures the total neutrino flux from the sun, independent of the flavour. Figure 1.3 shows, that this measured flux is in agreement with the standard solar model [Che85].

Determination of the Neutrino Oscillation Parameters

Numerous neutrino oscillation experiments determine the mixing angles of the PMNS-matrix as well as the squared differences. In the following, a summary of important experiments and their results is given. The global status report [FTV12] gives a detailed description of the experiments and the used analysis methods.

The Kamioka Liquid scintillator Anti-Neutrino Detector (KamLAND) determined the oscillation parameters θ_{12} and Δm_{12}^2 by investigating electron antineutrinos produced by fission reactors. The measured neutrino flux is a superposition of fluxes from several nuclear power reactor units with an effective baseline of $L_0 = 180$ km. The data of 2002 to 2007 show two complete oscillation cycles, proving not just the conversion of electron neutrinos into other flavours, but also the back-oscillation [Abe08]. By combining the results of several reactor and solar neutrino experiments, the oscillation parameters are calculated to $\Delta m_{12}^2 = (7.37 \pm 0.21) \times 10^{-5} \text{ eV}^2$ and $\sin^2 \theta_{12} = 0.297 \pm 0.016$ [P⁺16].

One possibility to determine Δm_{23} and Θ_{23} is to measure atmospheric neutrinos, like it is performed with the Super-Kamiokande detector [FFH⁺03]. Hadronic showers resulting from cosmic rays in the atmosphere produce electron and muon neutrinos as decay products. The ratio of muon to electron neutrinos amounts to $\nu_\mu/\nu_e \approx 2$ [GER16]. This ratio is constant within the energy range of 0.1 to 10 GeV. Super-Kamiokande is a water Cherenkov detector, which is able to reconstruct the energy, the flavour (electron or muon) and the direction of the neutrinos for this energy range. Therefore it can estimate the path length. Down-going neutrinos have a short flight length with approximately 10 km, whereas up-going atmospheric neutrinos have to cross the earth first before arriving at the detector. This results in a flight length of approximately 10^4 km. The measured data show a significant deficit of up-going muon neutrinos, which is inconsistent with expectations based on the flux. As the total number of electron neutrinos is consistent with the expectation, an oscillation from muon into tau neutrinos is assumed [FHI⁺98] [Wen10]. The combined results of Super-Kamiokande and accelerator experiments like MINOS [Ada13] deliver $\Delta m_{23}^2 = (2.44 \pm 0.06) \times 10^{-3} \text{ eV}^2$ and $\sin^2 \theta_{23} = 0.51 \pm 0.05$ [P⁺16].

The experiments Daya Bay, Double Chooz [Abe12] and Reno [Ahn12] try to quantify the small mixing angle θ_{13} with reactor neutrinos. Daya Bay measures the survival probability of electron antineutrinos at short distances (1 km) from the reactors. A near-far arrangement of additional detectors allows for a relative measurement of the neutrino flux, which minimises the systematic uncertainty [An,12]. By comparing results of different experiments, the mixing angle is determined to $\sin^2 \theta_{13} = 2.19 \pm 0.12$ [P⁺16].

Mass Hierarchy

The vacuum oscillation probability of neutrinos is proportional to $\sin^2(\alpha \Delta m_{ij}^2)$ and therefore not sensitive on the sign of Δm_{ij}^2 . It is not possible to solve the question, how the mass eigenstates are ordered, by only investigating vacuum oscillation. One approach for the answer uses the Mikheyev–Smirnov–Wolfenstein (MSW) effect.

The MSW effect is a conversion effect of electron flavoured neutrinos in matter, as a result of coherent forward scattering [SS91][Wol78]. In contrast to the vacuum oscillation, the resonance condition of the MSW effect is sensitive to the sign of Δm_{12}^2 , which leads to the recognition that $\Delta m_{21}^2 = m_2^2 - m_1^2 > 0$ [MS86][QV15].

Consequently, three theoretical models remain on how the mass of the neutrino eigenstates could be structured: the normal ($m_3^2 > m_1^2$), the inverted mass hierarchy ($m_3^2 < m_1^2$, see figure 1.4) or the quasi-degeneracy ($m_0^2 \equiv m_1^2 \approx m_2^2 \approx m_3^2$). Great efforts are made to find the sign of Δm_{31}^2 . One method is to determine the small difference between Δm_{31}^2 and Δm_{32}^2 in oscillation experiments like JUNO [AAA⁺16]. The absolute neutrino mass has to be accessed to exclude or confirm the quasi-degenerated mass hierarchy. [QV15].

1.4. Determination of the Neutrino Mass

The absolute neutrino mass can be estimated via several methods. In the following four of these methods are further explained. A complete overview is given in [Zub12].

1.4.1. Time-of-Flight Measurements of Supernovae

The supernovae SN1987A in the Large Magellanic cloud generated a high number of neutrinos of all flavours in a distance of approximately 1.5×10^{21} km. The Kamioka [HKK⁺87] and Irvine-Michigan-Brookhaven [BBB⁺87] detector measured twenty supernovae neutrinos. The neutrinos arrived with a spread of several seconds at the detectors, which is likely related to a propagation effect with non-zero mass. The delay t in the arrival time of any neutrino relative to the first neutrino can be calculated as a function of its energy,

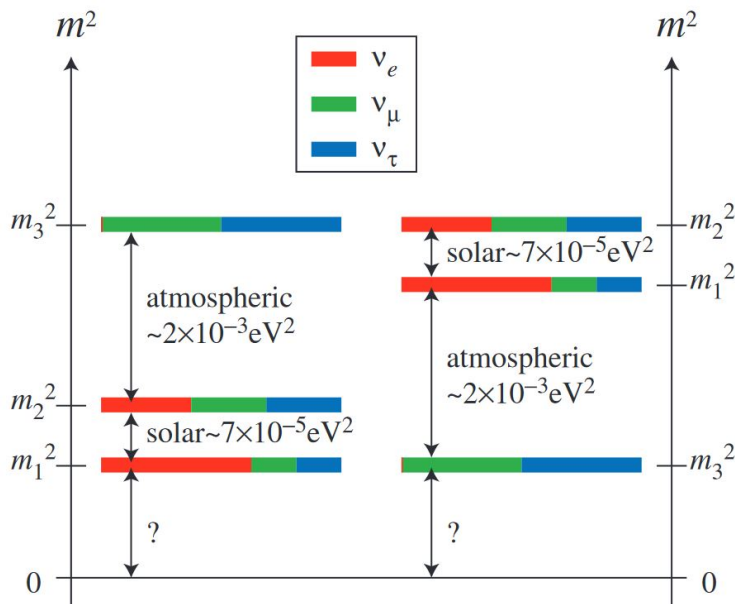


Figure 1.4.: Possible mass hierarchies of neutrinos. The left side shows the normal mass hierarchy ($m_3^2 > m_2^2 > m_1^2$), whereas the right side presents the inverted one ($m_2^2 > m_1^2 > m_3^2$). The quasi-degenerated hierarchy, in which all three eigenstates have nearly the same mass, is not displayed. The absolute neutrino mass scale (offset) could not yet be resolved [KL13].

assuming that the neutrinos were emitted at the same time. This function simplifies in the relativistic limit and delivers an estimation for the neutrino mass of

$$m \approx \left(\frac{2t}{T}\right)^{1/2} E_\nu \text{ [Cow88]}$$

with T as the time of flight. The Kamioka experiment observes a spread in two groups of neutrino masses. The first group contains neutrino masses within 2.8 to 5.8 eV, the second group masses within 16.5 to 27.8 eV. In the mean, two neutrino masses were measured: $m_{\nu_1} \approx 4 \text{ eV}$ and $m_{\nu_2} \approx 22 \text{ eV}$. However, this mass analysis has large statistical and systematic errors and strongly depends on the used supernova model [Cow88][DHMW13].

1.4.2. Cosmological Limits

A possible method to determine the neutrino mass is to measure a cosmological quantity which is influenced by the neutrino mass. The Λ CDM model explains the known evolution of the universe. The model is based on the assumption of a flat, expanding universe as result of the Big Bang. The cosmic microwave background (CMB) is a heat radiation left over from a hot and dense phase in the early universe (approximately 3.8×10^5 years after the Big Bang). The photons, produced in annihilation processes, decoupled from matter at that time due to the expansion of the universe. In this process the energy density was lowered. Up to this point, the universe was in a thermal equilibrium and the photons followed a black body spectra with $T \approx 3000 \text{ K}$. The CMB photons cooled down to $T \approx 3 \text{ K}$ today, as a result of the expansion [Par07]. The cosmic microwave background was discovered in 1965 by Penzias and Wilson [PW65]. Afterwards, numerous experiments, like WMAP [BHH⁺03], COBE [BBG⁺96] and Planck [Ade14] investigated the spatial distribution of the CMB spectrum with high precision. Especially the CMB anisotropies are of interest, as they provide informations on geometry and late-time evolution of the universe. The measured temperature power spectrum is consistent with the Λ CDM model. Its six parameters (for example the Hubble constant) can be estimated with the measured CMB spectrum. Further

conclusions, also in the neutrino sector, are stated based on the parameter estimations. The number of light neutrino generations is determined to $N_{\text{light}} = 3.15 \pm 0.23$ and the sum of neutrino masses is constrained to

$$\sum m_\nu < 0.23 \text{ eV [Ade14]}.$$

Nevertheless, the estimated neutrino masses strongly depend on the used cosmological model [Ade14].

1.4.3. Neutrino-Less Double β -Decay

As mentioned in chapter 1.2, the possibility exists that the small mass of neutrinos is a result of other processes than a simple coupling to the Higgs field. The standard model assumes all fermions to be Dirac particles. Consequently, the fermions are expected to have four degrees of freedom (left- and right-handed particle and left- and right-handed antiparticle). As neutrinos are electrically neutral, the theoretical possibility exists that they are Majorana particles. In that case, the electron antineutrino would be the same particle as the electron neutrino, but with opposite spin. This reduces the number of degrees of freedom to two [Maj08]. Many theorists favour the idea of neutrinos being Majorana particles, since it can explain the small neutrino masses with the so-called Seesaw mechanism.

The Seesaw mechanism postulates for each neutrino mass state ν_i an additional heavy Majorana neutrino mass state N_i with mass $\mathcal{O}(10^{15} \text{ GeV})$ [MSac80]. The initial neutrino mass m_{SM} is assumed to be in the range of charged leptons. However, this mass is suppressed in the Seesaw mechanism due to an interaction with the heavy Majorana neutrino

$$m_\nu \approx \frac{m_{SM}^2}{m_N} \text{ [Pov15]}.$$

The PMNS-matrix needs to be extended by two Majorana phases α and β

$$\underline{U}_{\text{Majorana}} = \underline{U}_{\text{Dirac}} \times \begin{pmatrix} 1 & 0 & 0 \\ 0 & e^{i\alpha} & 0 \\ 0 & 0 & e^{i\beta} \end{pmatrix},$$

which cannot be determined via oscillation experiments [Rod12]. The most realistic possibility to test, whether neutrinos are Majorana particles is the neutrino-less double β -decay ($0\nu\beta\beta$).

A single β -decay is energetically not possible for large nuclei ($A > 70$) with an even number of protons and neutrons. One possibility for the nucleus to get to an energetically more favourable state is the suppressed double β -decay

$$(A, Z) \rightarrow (A, Z + 2) + 2e^- + 2\bar{\nu}_e \text{ [Pov15]}.$$

The $0\nu\beta\beta$ is possible for all nuclei which can also undergo the normal double β -decay, in case that neutrinos are Majorana particles. In the $0\nu\beta\beta$, one neutron in the nuclei decays in a proton, an electron and a virtual right-handed neutrino. This virtual right-handed neutrino undergoes a spin-flip in the nuclei and is absorbed by another nuclei's neutron. In consequence of this absorption, the neutron decays in a proton and an electron (see figure 1.5 left), resulting in the net reaction of

$$(A, Z) \rightarrow (A, Z + 2) + 2e^-.$$

This process violates the lepton number by two units and is not allowed for Dirac neutrinos. $0\nu\beta\beta$ experiments measure the energy of both β -electrons. The two decay electrons gain

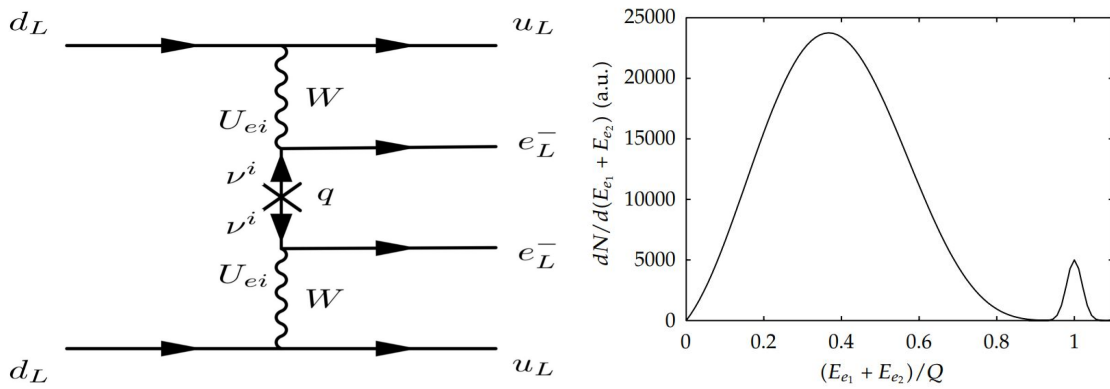


Figure 1.5.: Feynman graph and expected decay spectrum for the neutrinoless double β -decay. The Feynman graph on the left side describes schematically the $0\nu\beta\beta$ on parton level. The suppressing part of the decay is marked with a “x”, which represents the spin-flip of the virtual neutrino [Rod12]. The right graph sketches the double β -decay spectrum of the two electrons versus the summed up electron energy. The $0\nu\beta\beta$ results in a mono-energetic line at the endpoint of the spectrum, which is measured as a peak due to finite detector resolution [GP12].

the total decay energy in case of a $0\nu\beta\beta$. This results in a mono-energetic line at the endpoint of the decay spectrum. Due to a finite energy resolution of the detector, this mono-energetic line is measured as a peak (see figure 1.5 right) [Rod12].

An essential requirement for the $0\nu\beta\beta$ is the spin-flip of the virtual neutrino. The probability for this process is the squared ratio of neutrino mass over its momentum. Assuming a neutrino mass of 0.5 eV and a momentum of 10^8 eV, the probability for a $0\nu\beta\beta$ is suppressed by a factor of 10^{-18} . This suppression factor can be compensated to a certain point by the sheer number of atoms of the decaying isotope [Rod12].

The $0\nu\beta\beta$ can determine the effective electron neutrino mass

$$\langle m_{ee} \rangle = |c_{12}^2 c_{13}^2 m_{\nu_1} + s_{12}^2 c_{13}^2 m_{\nu_2} e^{i2\alpha} + s_{13}^2 m_{\nu_3} e^{i2\beta}| .$$

The effective mass is a coherent sum, therefore the possibility of cancellation exists [Ben15]. Several experiments like the Majorana demonstrator [AAA⁺14], Gerda [Ago13], KamLand-Zen [Gan13] or Cuoricino [And11] search for the neutrinoless double-beta decay. Due to the lack of measured events, only upper limits are published. The current upper limit for the effective electron neutrino mass is

$$\langle m_{ee} \rangle \lesssim 0.4 \text{ eV} [\text{Rod12}].$$

1.4.4. Single β -Decay

Using the kinematics of the single β -decay is a model-independent method to determine the effective electron antineutrino mass [Rod12]. The three-body decay reaction is

$$n \rightarrow p + e^- + \bar{\nu}_e . \quad (1.11)$$

The decay energy E_0 is split on the electron, the neutrino and the nuclear recoil. Measuring the β -electron spectrum with high precision enables the determination of the rest mass of the electron antineutrino by energy and momentum conversation. The relativistic energy-momentum equation $E^2 = m^2 c^4 + p^2 c^2$ shows, that in case of a relativistic neutrino its momentum superimposes the rest mass. Consequently, the rest mass can not be determined. The neutrino gets little energy at the endpoint of the β -spectrum, resulting in a small momentum and therefore a more precise determination of the rest mass (see figure 1.6).

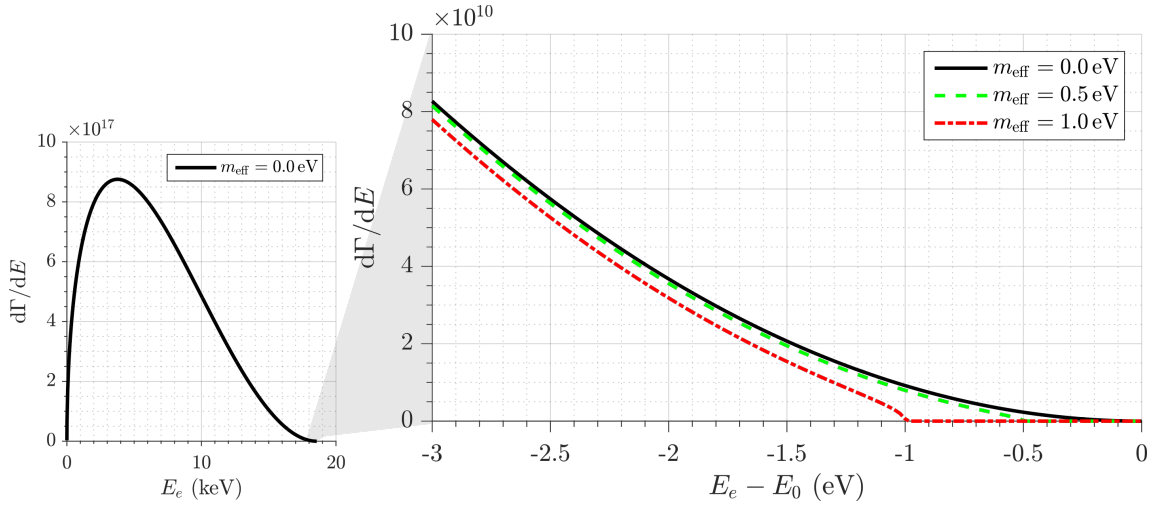


Figure 1.6.: Simulated decay spectrum of the single β -decay for several neutrino masses. The endpoint of the spectrum features the most precise information to determine the non-vanishing effective neutrino mass [Wik17].

Therefore, direct neutrino mass experiments are focused on the endpoint of the β -spectrum. The electron rate for the β -decay can be calculated via Fermi's Golden Rule

$$\frac{dN}{dt} = 2\pi \sum \int |M|^2 df$$

with the transition matrix element M . The integration of M takes place over all possible discrete and continuous final states f . The relativistic energy-momentum relation and super-allowed nuclear transitions modify the equation to

$$\begin{aligned} \frac{dN}{dE dt} = & \frac{G_F^2 \cos^2 \theta_C}{2\pi^3} \cdot |M|^2 \cdot F(Z+1, E) \cdot p \cdot (E + m_e) \\ & \times (E_0 - E) \cdot \sqrt{(E_0 - E)^2 - m_{\bar{\nu}_e}^2} \cdot \Theta(E_0 - E - m_{\bar{\nu}_e}). \end{aligned} \quad (1.12)$$

G_F represents the Fermi coupling constant, θ_C the Cabbibo angle, M the nuclear matrix element and $F(Z+1, E)$ is the Coulomb interaction of the outgoing electron with the nucleus and the shell electrons. E_0 is the maximum energetic momentum an emitted electron can posses and the Heaviside step function Θ guarantees energy conversation. Consequently, the observable of the β -decay is the squared neutrino mass

$$m_{\bar{\nu}_e}^2 = \sum_{k=1}^3 |U_{ek}|^2 m_k^2,$$

which is a superposition of the mass eigenstates. U_{ek} is the corresponding element in the PMNS matrix, which is already determined precisely in neutrino oscillation experiments [DHMW13] [OBW06].

The selection of the β -isotope and thus also E_0 plays an important role for optimal sensitivity of the experiment. A smaller E_0 is favoured, since it is easier to achieve a high energy resolution at smaller energies. β -electrons, which are not part of the relevant tail region of the decay spectrum, can cause background events. This probability also decreases with E_0 [DHMW13].

Tritium has one of the lowest endpoints (18.6 keV) of all β -emitters together with a reasonable long half-life (12.3 years). It decays via the β^- -decay



into helium. The small decay energy enables the possibility to use MAC-E filters for the spectroscopy of β -electrons. The half-life is short enough to feature a high activity of the source resulting in high statistics within a reasonable measurement time [LU00].

${}^3\text{H}$ and ${}^3\text{He}$ are mirror nuclei, therefore the matrix element of equation 1.12 is energy-independent. This simplifies the theoretical calculation. Additionally, tritium has a simple electronic structure with only one shell electron, which also simplifies the theoretical calculation of the Fermi function in equation 1.12 [RK88].

The neutrino mass experiment in Mainz [KBB⁺05] and Troitsk [ABB⁺11] used tritium as source for β -electrons due to these properties. Also the KATRIN experiment uses tritium, but in a molecular gaseous state. Hence, the recoil energy of tritium in KATRIN is small. The maximal recoil energy for molecular tritium is $E_{\text{rec,max}} = 1.72\text{ eV}$ in the endpoint region of the decay spectrum. The variation of the recoil energy is 3.5 meV and thus negligible [MNS⁺07]. However, the molecular state complicates the electronic final states. Two identical electrons, rotational and vibrational states have to be considered, which leads to a blur in the energy of the transition [DTSJ06].

The tritium β -decay experiments in Mainz and Troitsk have measured the best limits on the model-independent electron antineutrino mass up to this date. By combining the measured data, the upper limit on the electron antineutrino mass is

$$m_{\bar{\nu}_e} < 2.05\text{ eV (95 \% CL}^2\text{)} [\text{P}^+16].$$

Both experiments have reached their sensitivity limits due to the systematic uncertainty [Wol10]. A new β -decay experiment is needed, to improve the limit on the neutrino mass by one order of magnitude.

²Confidence Level (see chapter 2.3.1)

2. The KATRIN Experiment

The **K**arlsruhe **T**ritium **N**eutrino experiment is a next-generation β -decay experiment to model-independently determine the mass of the electron antineutrino. The goal of KATRIN is to achieve a sensitivity on the electron antineutrino mass of 0.2 eV (90 % CL) after three “full-beam” years of measurement. Equation 1.12 shows, that the experimental observable in single β -decay neutrino mass experiments is $m_{\bar{\nu}_e}^2$. An aimed improvement of the sensitivity of factor 10 on $m_{\bar{\nu}_e}$, compared to the experiments in Mainz and Troitsk, results therefore in an improvement of factor 100 in the accuracy in the experimental set-up [Wol10] [DHMW13].

The 70 m-long KATRIN set-up is separated into two parts: the source and transport section (STS) and the spectrometer and detector section (SDS, see figure 2.1). The STS contains the rear section (a), the windowless gaseous tritium source (b), the differential (c) and cryogenic pumping section (d). The pre (e)- and main spectrometer (f) as well as the focal plane detector (g) are in the SDS part [Wol10]. The magnetic flux tube adiabatically guides the electrons, which are emitted in the source, through the transport section and the main spectrometer to the focal plane detector.

In the following, the components of the STS (chapter 2.1) and the SDS (chapter 2.2) are described in more detail. Chapter 2.3 introduces important analysis tools and terms to determine the neutrino mass.

2.1. The Source and Transport Section

This chapter summarises the tasks and the requirements of the different components of the STS. The KATRIN design report [KAT05] delivers a more comprehensive description of the requirements.

2.1.1. Rear Section

The task of the rear section is to monitor and calibrate several properties of the windowless gaseous tritium source (WGTS). Between the WGTS and the calibration and monitoring system, a gold-plated crystalline rear wall is installed. Besides separating the WGTS from the calibration and monitoring system, it also defines the electric potential of the tritium plasma. In addition, it can directly measure the β -electron current and the activity of the source via β -induced x-ray spectroscopy. An electron gun [VHB⁺11] is placed behind the rear wall. Based on the photoelectric effect, electrons are produced with adjustable energy and well defined pitch angle relative to the magnetic field. The electron gun enables a calibration of KATRIN components [BBB⁺12] [DHMW13].

2.1.2. Windowless Gaseous Tritium Source

β -decay electrons are produced via the decay of molecular tritium in the WGTS. The conditions inside the WGTS have to be adjusted exactly and with high stability, to ensure

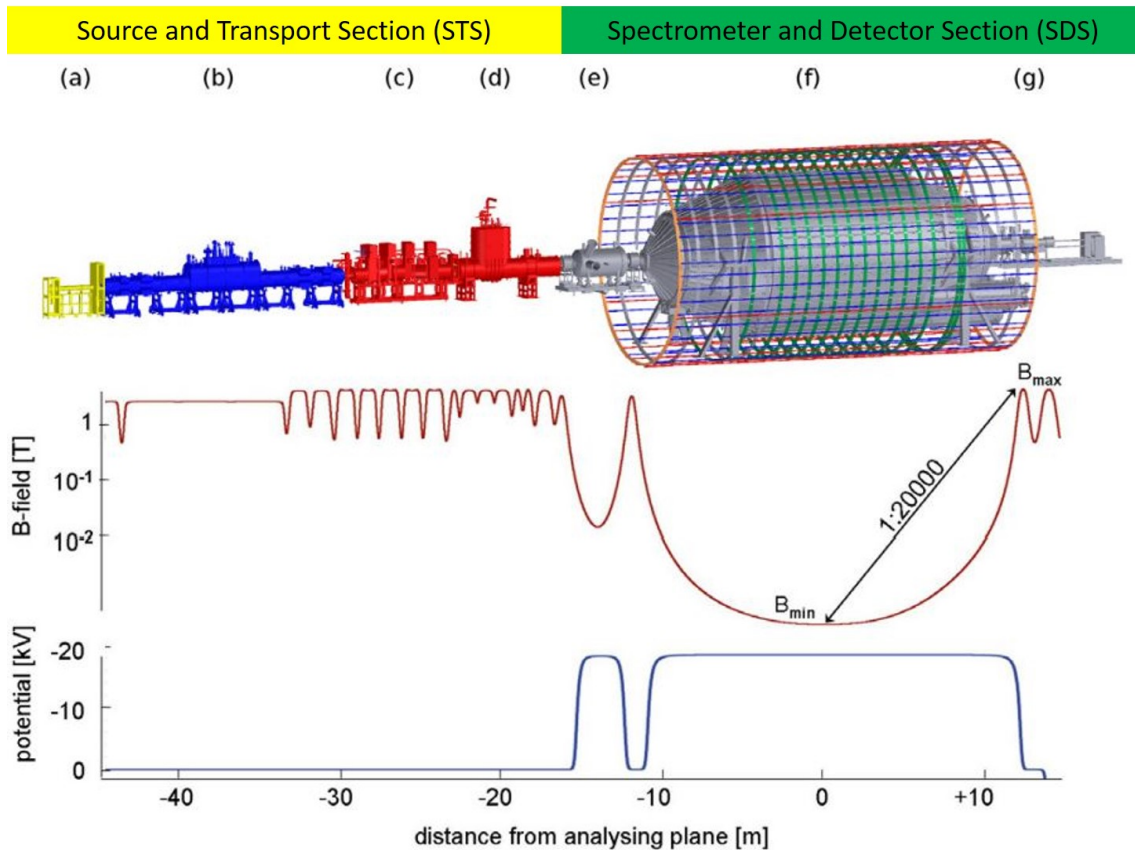


Figure 2.1.: The schematical KATRIN set-up with an overview of applied magnetic field and retarding potential. The upper line displays the schematical KATRIN set-up. The source and transport section consists of the (a) rear wall, (b) windowless gaseous tritium source, (c) differential pumping section and the (d) cryogenic pumping section. In the spectrometer and detector section the (e) pre-spectrometer, (f) main spectrometer and the (g) detector are located. The middle line sketches the magnetic field strength for this set-up with a logarithmic y-axis. The transport section requires a high magnetic field strength to guide the decay electrons, whereas a large drop of the field strength in the main spectrometer is a key feature of KATRIN for the aimed energy resolution. The retarding potential is plotted in the lower line, which is only applied in the spectrometer and detector section to scan the decay spectrum. Adapted from [GDL⁺13].

high luminosity and simultaneously small systematic uncertainty. The WGTS consists of a 10 m-long beamtube, in which ultra-cold molecular tritium gas is kept at a temperature of 27 K and a maximal deviation of 30 mK. The temperature is set to 27 K to minimise the contribution of the thermal Doppler broadening [FSP⁺08] of electron energies. Additionally, this minimises the tritium throughput in the beamline [DHMW13]. The injected gas has an isotopic purity larger than 95% with an injection pressure of 3.4×10^{-3} mbar. The column density of the WGTS is set to its design value of $\rho d = 5 \times 10^{17}$ molecules/cm² by a variation of the injection pressure. The main systematic uncertainty is related to the column density, which must be known to the precision of 0.1%. Consequently, an appropriate stability of all WGTS parameters is required [Wol10] [KAT05].

After the injection of the molecular tritium gas, the molecules are transported to both ends of the WGTS via diffusion. The probability for a single tritium molecule to decay during this mean diffusion time of approximately one second, is of the order of 10^{-9} . The applied magnetic field guides the emerging β -electrons out of the WGTS. The WGTS will deliver 9.5×10^{10} β decays per second within the magnetic flux tube in the nominal neutrino mass

measurements. [KAT05].

The WGTS emits not only β -electrons but also tritium molecules, which can produce background events (e.g. if tritium molecules decay in the spectrometers). As this reduces the sensitivity of the KATRIN experiment, the tritium flow has to be suppressed by a factor of 10^{14} between the outlet of the WGTS and the entrance of the pre-spectrometer. Turbo molecular pumps reduce the tritium flow already at the rear and front (DPS1-F) end of the WGTS by two orders of magnitude [DHMW13]. The collected tritium molecules are fed into a closed inner-loop system [Stu10]. A part of the collected tritium molecules is used to check the gas composition via laser Raman spectroscopy [SSR⁺13], the rest is re-injected into the WGTS.

The Differential (DPS2-F) and Cryogenic Pumping Section (CPS) ensure a further reduction of the tritium flux in the transport section [KAT05] [M⁺15].

2.1.3. Transport Section

The transport section reduces the tritium flow by eleven orders of magnitude and at the same time guides the signal electrons adiabatically from the source to the spectrometers. The first part of the transport section after the WGTS is the DPS2-F. The operation mode of the 6 m-long section with an inner beam tube diameter of 100 mm is based on turbo-molecular pumping. The DPS2-F consists of several segments, which are inclined by 20° . A direct line of sight between the WGTS and the following CPS does therefore not exist. Between each segment, pumping ports are installed. A strong magnetic field (approximately 5 T, see figure 2.1) guides the signal electrons through the segments. The neutral tritium molecules hit the walls and are then pumped out of the beamline. This reduces the tritium flow by five to seven orders of magnitude. The loop system feeds the pumped out tritium molecules back to the WGTS [GBB⁺10] [LBB⁺12] [DHMW13]. The magnetic field guides ions, which are produced in the WGTS by ionisation of β -electrons, towards the spectrometers, similar to the β -electrons. Several ring electrodes are mounted in the DPS2-F to reflect the ions, as they can cause background events. Additionally, four dipole electrodes are installed which remove trapped ions from the beamline [DHMW13].

Downstream of the DPS2-F, the 7 m-long CPS is located. The CPS again reduces the tritium flow by seven orders of magnitude. As well as the DPS2-F, also the CPS is formed in a zigzag arrangement, to prevent a direct line of sight for neutral tritium molecules. The magnetic field guides the electrons adiabatically through this chicanery. Seven superconducting magnets produce the necessary magnetic field strength of up to 5.7 T [KAT05]. A 3 K-cold argon layer covers the inner surface of the CPS. The surface absorbs neutral tritium which hits the wall with a probability of approximately 70 % [Hae81]. Since one data taking period in the neutrino mass measurements has a length of up to 60 days, the argon frost layer temperature has to be stabilised over this period with a dedicated cooling system. Helium gas with a temperature of 100 K purges the CPS to remove tritium and argon after the data taking phase. Before starting the next measurement phase, a new layer of argon is deposited on the inner surface of the CPS.

Instabilities in the WGTS represent a large part of the systematic uncertainties of KATRIN [KAT05]. A detection possibility of instabilities is by measuring the flux of β -electrons. This is achieved with the Forward Beam Monitor, which is a doped silicon detector located in a pump port of the CPS. The β -electron flux in the outer region of the magnetic flux tube is measured by it with a precision of 0.1 %. Additionally, a condensed krypton source can be installed for calibration measurements at the down-stream end of the CPS (see also appendix A) [GBB⁺10] [Jan15].

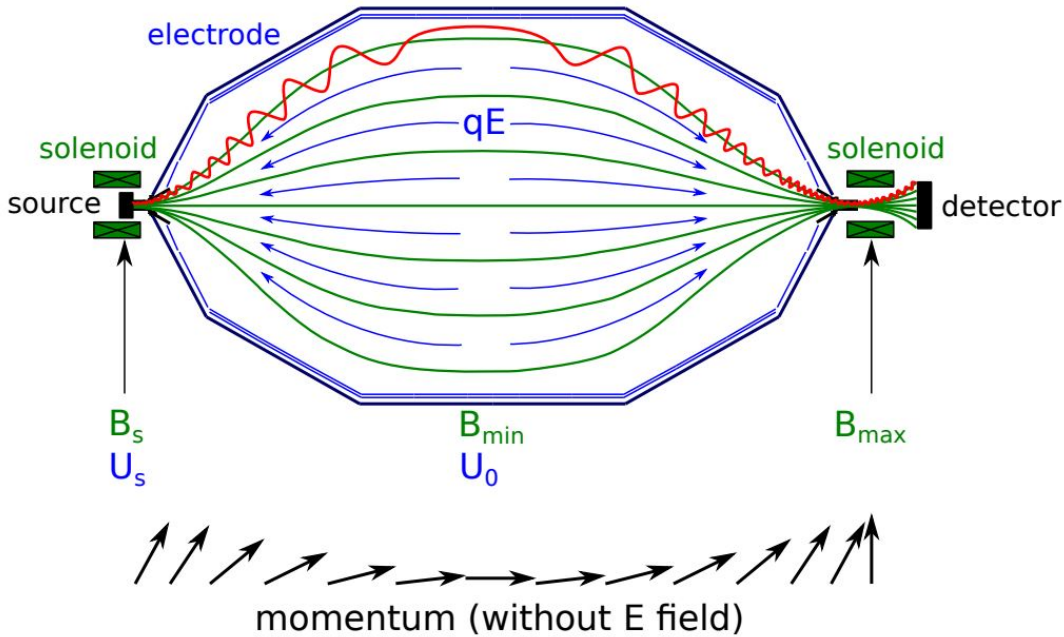


Figure 2.2.: Schematical operating principle of the main spectrometer. The decay electrons (red) enter the spectrometer from the left side and are guided by the magnetic field (green) to the detector. Through a drop of the magnetic field strength in the middle of the spectrometer, the momentum is tilted in longitudinal direction. A voltage, applied on the spectrometer vessel (blue), creates a retarding potential inside the main spectrometer [Wan13].

2.2. The Spectrometer and Detector Section

The unique feature of the KATRIN experiment is the tandem spectrometer section, consisting of a pre- and main spectrometer. These spectrometers are MAC-E filters¹, which work as high-pass filters for the β -decay electrons. The first chapter 2.2.1 explains the principle of MAC-E filters, before the following chapters 2.2.2 and 2.2.3 describe the hardware of the pre- and main spectrometer. The subsequent chapters characterise further components of the SDS, namely the monitor spectrometer (chapter 2.2.4) and the focal plane detector (chapter 2.2.5).

2.2.1. Operating Principle of MAC-E Filters

The operating principle of MAC-E filters is proposed in [BPT80]. Neutrino mass experiments use MAC-E filters due to their high energy resolution and large acceptance solid angle of nearly 2π [PBB⁺92b]. A MAC-E filter is based on a magnetic adiabatic collimation followed by an electrostatic filter [BBD⁺99]. At first, this chapter introduces the electrostatic filter, secondly the magnetic collimation of the electrons and as a last point the magnetic mirror effect.

Electrostatic Filter

β -decay electrons of tritium can reach a maximal kinetic energy of 18.6 keV. A MAC-E filter generates an electrostatic barrier, which defines a threshold for the signal electrons. Therefore, a negative potential U_0 is applied at the spectrometer vessel. Low-energy electrons with a longitudinal kinetic energy $E_{||} < q|U_0|$ are reflected at the centre of the spectrometer, the so-called “analysing plane”. A variation of the size of the electrostatic

¹Magnetic Adiabatic Collimation followed by Electrostatic filter

barrier changes the threshold for signal electrons and enables a scan of the integrated β -spectrum. The electrostatic filter is only sensitive to the longitudinal kinetic energy, yet the electrons are emitted isotropically in the WGTS [Har15]. Therefore, a transformation of the kinetic energy into the longitudinal component is needed, which is performed by magnetic adiabatic collimation.

Magnetic Adiabatic Collimation

The kinetic energy of signal electrons can be written to

$$E_{\text{kin}} = E_{\parallel} + E_{\perp} \quad (2.1)$$

with respect to the magnetic field lines. The transverse component is responsible for the cyclotron motion around the magnetic field lines. This component shall be transferred into the longitudinal one for energy analysis in the MAC-E filter. A variation of the magnetic field strength enables this transformation. A strong magnetic field ($B = 3.6 - 5.7 \text{ T}$) is applied in the WGTS and the beamline (see figure 2.1). The magnetic field reaches its minima B_{min} in the centre of the spectrometer. The magnetic moment

$$\mu = \frac{E_{\perp}}{B} \quad (2.2)$$

is conserved under adiabatic magnetic field changes. By lowering the magnetic field strength, the longitudinal component of the kinetic energy increases and the transversal decreases accordingly (see figure 2.2). A large ratio of the maximal magnetic field strength B_{max} to B_{min} ensures, that nearly the whole transverse component of the energy is transferred into the longitudinal component. To guarantee the adiabaticity of this process, the magnetic field should decrease with small gradients. This defines the minimal length of a MAC-E filter.

However, the magnetic field line in the analysing plane is non-zero. This gives a limit on the maximal possible transformation of the transversal into the longitudinal energy component. Therefore, the lower limit of the resolving power is defined to

$$\Delta E = \frac{B_{\text{min}}}{B_{\text{max}}} \cdot E_{\text{kin}} \quad (2.3)$$

A decrease of the magnetic field strength towards the analysing plane results in an increase of diameter of the magnetic flux tube. This is due to the conservation of the magnetic flux

$$\Phi = \int_A \vec{B} \cdot d\vec{A} = \text{const.} \quad (2.4)$$

Consequently, the maximum diameter is calculated to

$$d_{\text{max}} = d_{\text{S}} \sqrt{\frac{B_{\text{S}}}{B_{\text{min}}}} \quad (2.5)$$

with d_{S} as diameter of the magnetic flux tube in the magnetic field B_{S} of the source. The increase of the diameter in the analysing plane defines the radial extent of the MAC-E filter [PBB⁺92b] [MDF⁺13]. To achieve the aimed neutrino mass sensitivity of 200 meV, an energy resolution of $\Delta E = 0.93 \text{ eV}$ is required. A ratio of $B_{\text{min}}/B_{\text{max}} = 5 \times 10^{-5}$ is necessary for β -electrons at the endpoint of the tritium spectrum. The nominal magnetic flux tube diameter of approximately 53 cm^2 in the WGTS [KAT05] results in a diameter of 9 m in the analysing plane of the spectrometer. Due to the inner electrode system and a safety margin, the main spectrometer is designed with a radial extension of 10 m [KAT05].

Magnetic Mirror Effect

β -electrons with large polar emission angles in the source relative to the magnetic field lines have extended path lengths in the transport section compared to electrons with smaller polar emission angles. On the extended path, these electrons lose more energy via synchrotron radiation and scattering with residual gas molecules. As the information about their energy is distorted, it is beneficial to exclude the electrons with large emission angle. This is done with the magnetic mirror, by placing the strongest magnetic field B_{\max} at the end of the MAC-E filter and not in the β -electron source (see figure 2.1). Therefore, electrons with large emission angles are reflected. The maximal polar acceptance angle θ for β -electrons near the endpoint of the decay spectrum can be approximated to

$$\theta_{\max} = \arcsin \left(\sqrt{\frac{B_S}{B_{\max}}} \right). \quad (2.6)$$

The exact formula for the maximal acceptance angle is stated in chapter 4.1 [DHMW13] [MDF⁺13].

2.2.2. Pre-Spectrometer

The pre-spectrometer is the upstream MAC-E filter in the tandem spectrometer set-up of KATRIN. In the nominal neutrino mass measurement, the retarding voltage of the pre-spectrometer is set to a voltage $|U_0| < E_0$ to reduce the number of decay electrons in the main spectrometer by several orders of magnitude. This also lowers the number of background events by ionisation of residual gas in the main spectrometer.

The 3.4 m-long pre-spectrometer is made of stainless steel and has an inner diameter of 1.68 m. Two pump ports, which are equipped with a set of turbo-molecular pumps (TMPs) and a non-evaporable getter (NEG) pump, maintain the vacuum inside the 8.3 m³-large vacuum chamber. The retarding high voltage potential is directly applied onto the vessel, which allows an inner electrode system for the fine-shaping of the potential and suppression of background events from the walls.

The pre-spectrometer was the first KATRIN hardware component at Karlsruhe, it has been delivered in 2003. The results of several tests with the pre-spectrometer were used for the vacuum concept and electromagnetic design of the larger main spectrometer [FBD⁺11] [Dre05] [Frä10].

2.2.3. Main Spectrometer

The main spectrometer is a large MAC-E high-resolution energy filter with a length of 23 m and a diameter of 10 m. It can reach an energy resolution of up to 0.93 eV at the endpoint of tritium [Val10].

To reach the aimed KATRIN sensitivity on the neutrino mass, a gas pressure smaller than 10⁻¹¹ mbar is needed in the main spectrometer. This is ensured by several turbo-molecular pumps, non-evaporable getter material and a dedicated baking of the spectrometer to temperatures of 200 °C [Wol09].

The main spectrometer is located between two superconducting magnets with a maximal field strength of 4.5 T at the entrance of the main spectrometer and maximal 6 T at its exit to guide the electrons through the vessel. The total magnetic field strength drops to approximately 3 × 10⁻⁴ T in the analysing plane. The large drop in the magnetic field strength by four orders of magnitude is responsible for the high energy resolution.

The main spectrometer is surrounded by two large air-coil systems (see figure 2.1). One is the Earth Magnetic field Compensation System (EMCS) which compensates the earth magnetic field. Due to the large dimensions of the main spectrometer, even small magnetic field strengths can distort the symmetric shape of the magnetic flux tube inside the vessel.

The EMCS consists of 16 vertical and 10 horizontal cosine coils. The second magnetic system around the main spectrometer is the Low Field Coil System (LFCS) which fine-shapes the flux tube in the centre of the spectrometer. The LFCS consists of 14 normal-conductive coils surrounding the spectrometer vessel.

A negative potential (~ 18.4 kV) is applied onto the main spectrometer vessel, to produce the retarding potential for the β -electrons. Similar to the pre-spectrometer, an inner electrode system is installed on the inside of the vessel to fine-shape the electric field and to reduce background events (see chapter 4) [Val09] [Har15] [B⁺10].

2.2.4. Monitor Spectrometer

The KATRIN experiment is highly dependent on the accuracy and stability of the electric field strength in both spectrometers and thus on the applied high voltage [KAT05]. Two methods are used, to monitor the applied voltage. First, the high voltage is scaled down with a voltage divider to measure it with a high precision voltmeter. The second method uses the MAC-E filter of the former Mainz neutrino experiment. It is called monitor spectrometer in the KATRIN set-up. The monitor spectrometer is operated with two superconducting magnets, an inner electrode system, an air coil system to fine-shape the magnetic field in the analysing plane and with the same high voltage source as the main spectrometer. Downstream of the monitor spectrometer, an electron detector is installed. The spectrometer determines the position of a narrow electron peak by varying its retarding potential. Any change in the position or the shape of the peak points to an instability of the high voltage system. For the cross-check, the K-32 conversion line of the γ -decay of $^{83\text{m}}\text{Kr}$ with subsequent electron emission is used. The K-32 conversion line has a narrow width of only 2.8 eV and its energy of 17.8 keV is near the endpoint of tritium [PBB⁺92a] [Val09] [SBD⁺13].

2.2.5. Focal Plane Detector

The focal plane detector (FPD) system was constructed at the University of Washington and installed at Karlsruhe in 2011. The pinch magnet at the exit of the main spectrometer collimates the decay electrons, which pass the spectrometer. The electron beam is afterwards guided to the lower magnetic field of the detector magnet and accelerated with an electrode before reaching the FPD.

The FPD is a circular PIN-diode array housed on a silicon wafer. Ionising particles deposit energy by forming free charge carriers, which are collected by the read-out electronics. The detector and pre-amplifier are cooled with liquid nitrogen through the post acceleration electrode. The sensitive area of the wafer has 90 mm in diameter, a thickness of 500 μm and is separated in 148 pixels of equal area. The pixels allow a spatial resolution of the observed flux tube and are placed in rings on the detector. The inner ring, the so-called bulls-eye, contains four pixels, the outer twelve rings contain twelve pixels each. An electron source and a γ -emitter can be inserted in the beamline between the pinch and detector magnet for calibration purposes [ABB⁺15] [Sch14].

Between the detector magnet and the post acceleration electrode, a passive copper and lead shield are installed for background reduction in the detector section. Furthermore, a veto system for cosmic muons is used. The post-acceleration of the FPD enables the shift of signal electron energies to a region with a small intrinsic detector background rate (see chapter 4.7) and reduces the backscattering probability [Sch14].

2.3. Neutrino Mass Analysis with KATRIN

This chapter introduces the analysis tools and terms to determine the neutrino mass with KATRIN. Crucial terms in the course of the evaluation of statistical results as performed

with KATRIN are the terms “confidence interval” and “confidence level”, which are defined in chapter 2.3.1. Chapter 2.3.2 describes the region-of-interest cut, which allows to remove a part of the intrinsic detector background electrons in the KATRIN analysis. The following chapter 2.3.3 explains the method to determine the neutrino mass based on the measured data. The systematic and statistical error budgets are introduced in chapter 2.3.4.

2.3.1. Confidence Interval and Level

Measurements of physical quantities are always entailed with uncertainties. A method to quantify the statistical uncertainty of a measurement is the confidence interval, which is linked to a confidence level. In the following, the terms confidence level and interval are introduced by the example of the radioactive decay.

A large part of processes happens on a random basis in quantum mechanics, for example the decay of unstable atoms. By measuring the decay time of a great number of unstable atoms, one can determine a value for this sort of atoms. This estimation ($\hat{\tau}$) does not need to be necessarily in accordance with the true value of the half-life (τ), as $\hat{\tau}$ is dependent on the statistical fluctuations of the decay time of the single atoms. Increasing the number of decay atoms in the experiment leads to a larger accordance between $\hat{\tau}$ and τ .

The confidence interval quantifies the uncertainty on $\hat{\tau}$. It is constructed with the measured data. The confidence interval is linked to a probability, which is called confidence level. The confidence level is set to 68 % for this example. This means, that in case of an infinite repetition of the experiment, the true value τ lays in 68 % of the experiments within the constructed confidence intervals of the estimator $\hat{\tau}_i$ [Geo15].

In the following, the used confidence level for the uncertainty of parameters is 68.27 %, if not stated otherwise. The corresponding confidence interval is abbreviated with σ . The previous interpretation of the confidence level is the Frequentist inference of statistics, which is usually used in the course of this thesis. The Frequentist approach claims to be completely objective.

The Bayesian approach is used in chapter 3. The Bayesian approach includes a personal assumption about the to be estimated parameter (e.g. mass of a particle is not negative). The advantage of the Bayesian over the Frequentist approach is, that a probability on the parameter value of one single outcome of an experiment can be reported. However, the outcome of a Bayesian approach is dependent on the assumption made beforehand, which is the disadvantage of this approach [Wal15].

2.3.2. Region-of-Interest Cut

Not all electrons measured at the FPD are of interest for the neutrino mass analysis, since a lot of background electrons are produced in the KATRIN set-up. A region-of-interest (ROI) cut is defined to remove the major part of the intrinsic detector background. The neutrino mass analysis considers only those electrons, which have an energy within the ROI. The centre of the ROI is the expected incident energy E_0 of the signal electrons, which is calculated to

$$E_0 = E_i + q(-U_A + U_{\text{PAE}} + U_{\text{BIAS}}) . \quad (2.7)$$

E_i is the energy of the β -electrons in the analysing plane of the MAC-E filter, which is in the neutrino mass analysis approximately 0 eV. U_A represents the acceleration voltage of the electrons, which is the same as the applied retarding voltage. U_{PAE} is the post acceleration voltage of the detector section, the typical value for the post acceleration voltage is 10 kV. The bias voltage of the FPD U_{BIAS} is always set to 0.12 kV [Frä15].

The FPD had an average energy resolution of about 2.2 keV in the SDS-II measurement

phase. Consequently, the ROI needs to have a total width larger than 2.2 keV. If it is too broad, the weak energy dependence of the intrinsic detector background leads to problems. Additionally, more background electrons are included in the analysis. A decision for an asymmetric energy interval was made in the SDS-II measurement phase, as the incident electrons suffer from energy losses in the dead-layer of the detector. The default ROI for the SDS-II phase is defined from 3 keV below E_0 to 2 keV above [Har15] [Frä15].

A new ROI was defined for the krypton campaign and subsequent measurement phases, due a degradation of the FPD resolution and to improve robustness against energy fluctuations. The ROI was extended to 3 keV above and below E_0 [Eno17].

The following analyses use these default ROI cuts, if not stated otherwise. To investigate special effects (for example the decay of ^{210}Pb), other ROI cuts are defined.

Nevertheless, the ROI cut only removes a part of the intrinsic detector background. However, the intrinsic spectrometer background dominates the overall background rate. Background reduction mechanisms are required (see chapter 4), as this background lays within the default ROI.

2.3.3. KATRIN Likelihood

The electron rate, measured in the KATRIN experiment, is the integrated β -decay spectrum, smeared with systematic and statistical effects. The expected number of counts N_s of the decay spectrum is calculated to

$$N_s(qU, E_0, m_\nu^2) = N_{\text{tot}} \cdot t_U \int_0^{E_0} \frac{dN_\beta(E_0, m_\nu^2)}{dE} \cdot f_{\text{res}}(E, qU) dE .$$

N_{tot} describes the total number of tritium nuclei in the source. t_U represents the measuring time at a certain retarding potential U , whereas f_{res} is the response function of KATRIN. However, there are also background processes (see chapter 4), which contribute to the measured rate. The KATRIN design report assumes the background counts N_b to be independent of the retarding potential in the neutrino mass scanning range [KAT05]. The theoretical prediction for the total measured background is therefore

$$N_{\text{th}}(qU, m_\nu^2, E_0, R_s, R_b) = R_s \cdot N_s(qU, m_\nu^2, E_0) + R_b \cdot N_b . \quad (2.8)$$

with R_s and R_b as relative amplitude of signal and background electrons. Quantum mechanical effects smear the number of expected counts with a Gaussian distribution with width $\sqrt{R_s \cdot N_s + R_b \cdot N_b}$ [KAT05].

The neutrino mass shall be determined, based on the measured counts N_{obs} . Likelihood minimisation, which is a powerful tool in parameter estimation, enables this determination. The likelihood function L describes the probability how likely a particular outcome of a measurement is. The probability of observing the outcome N (in KATRIN the measured number of counts), given the parameters' fixed values as input, is equal to the likelihood L given a set of observations as input with free model parameters. The expected number of counts N_{th} depends on five parameters (see equation 2.8). It depends on the retarding potential, which can be set, and four parameters (squared neutrino mass m_ν^2 , endpoint of tritium E_0 , signal R_s and background amplitude R_b) which are not known a priori. These four parameters have to be estimated by the measured data with the likelihood

$$L(m_\nu^2, E_0, R_s, R_b | N_{\text{obs}}) = \prod_i p(N_{\text{obs},i} | N_{\text{theo},i}(qU_i, m_\nu^2, E_0, R_s, R_b)) . \quad (2.9)$$

The index i denotes several applied retarding potentials. $p(N_{\text{obs},i} | N_{\text{theo},i})$ refers to the probability of making a single observation $N_{\text{obs},i}$ under the theoretical assumption of $N_{\text{theo},i}$. The values of R_s , R_b , E_0 and m_ν^2 are the best-fit estimators at the global maximum of

L . This allows a careful statement about their true values [Kle14]. The shape of the likelihood enables an estimation of the parameter's uncertainties [Jam80]. Due to numerical reasons, it is common not to maximise the likelihood but to minimise the negative logarithmic likelihood [Wal15].

2.3.4. Statistical and Systematic Uncertainty Budget

The shape of the negative logarithmic likelihood around its minima allows the calculation of the statistical uncertainty on the determined neutrino mass. The minimisation process of the likelihood delivers the best-fit estimator for the squared neutrino mass and its uncertainty $\sigma_{m_\nu^2}$. For a small neutrino mass, the uncertainty on the neutrino mass is approximated to

$$\sigma_{m_\nu} = \sqrt{\sigma_{m_\nu^2}} \quad (2.10)$$

The statistical fluctuations $\sqrt{R_s \cdot N_s + R_b \cdot N_b}$ of the measured counts influence the shape of the likelihood and therefore also the uncertainty of the squared neutrino mass. The uncertainty of the squared neutrino mass decreases with smaller fluctuations. The signal electrons are needed for determining the neutrino mass, whereas the background electrons increase the statistical fluctuations and thus need to be minimised.

Additionally, the statistical uncertainty of the squared neutrino mass depends on the uncertainties of the so-called nuisance parameters (E_0 , R_s , R_b). As the parameter of interest (m_ν^2) correlates with the nuisance parameters, their uncertainties propagate onto the uncertainty of the parameter of interest [Wal15]. Smaller uncertainties of the nuisance parameters therefore minimise also the uncertainty of the parameter of interest. To ensure a small uncertainty on m_ν^2 , a measurement time distribution is calculated which delivers the highest sensitivity to all parameters (see figure 2.3).

The statistic uncertainty of the squared neutrino mass is estimated for a background rate of 10 mcps and a measurement time of three “full-beam” years to

$$\sigma_{m_\nu^2, \text{stat}} = 0.018 \text{ eV}^2 \text{ [KAT05]}. \quad (2.11)$$

Systematic effects, which cannot be further minimised (e.g. variations of the high voltage, uncertainty in the description of final tritium states etc.), cause a shift on the measured neutrino mass. Studies of the design report quantify the shift $\sigma_{\text{syst},i}$ of each systematic effect on the squared neutrino mass. The overall systematic uncertainty is calculated to

$$\sigma_{m_\nu^2, \text{syst}} = \sqrt{\sum_i \sigma_{\text{syst},i}^2} = 0.017 \text{ eV}^2 \text{ [KAT05]}. \quad (2.12)$$

The total uncertainty on the squared neutrino mass, measured with KATRIN, is therefore

$$\sigma_{m_\nu^2, \text{tot}} = \sqrt{(\sigma_{m_\nu^2, \text{stat}})^2 + (\sigma_{m_\nu^2, \text{syst}})^2} \quad (2.13)$$

resulting in the aimed sensitivity on the effective neutrino mass of 200 eV with 90 % CL [HLAE07].

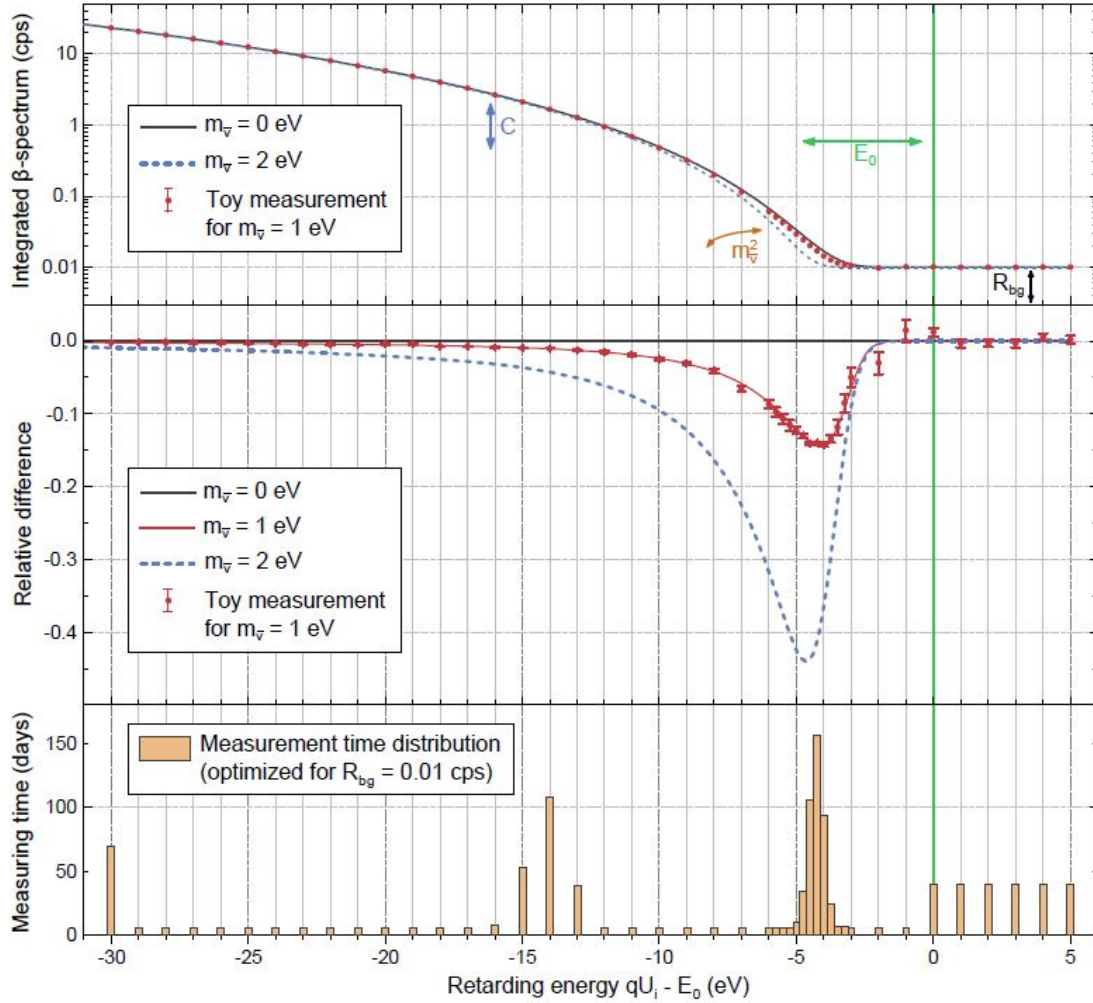


Figure 2.3.: Measurement time distribution for the integrated β -spectrum.

In the upper plot the integrated β -spectrum is simulated for two different neutrino masses as well as for a toy measurement with a neutrino mass of 1 eV. Additionally, the most sensitive measurement places for the four free parameters relative signal (C) and background amplitude (R_{bg}), endpoint of tritium (E_0) and squared neutrino mass (m_ν^2) are marked. The graph in the middle shows the relative difference of the expected spectrum for a vanishing neutrino mass with the spectrum of an assumed neutrino mass of 1 eV (2 eV). This highlights the retarding potential at which the highest sensitivity is given for determining the neutrino mass. The lower plot displays the measurement time distribution for a “full-beam” measurement time of three years and a background rate of 10 mcps. The run-time distribution is optimised for highest possible sensitivity on the neutrino mass and consequently high sensitivity on the three nuisance parameters [Har15].

3. Systematic Uncertainties of Rate Estimation

Due to physical processes in the focal plane detector and read-out artefacts, the number of recorded events is not equal to the number of incident electrons. In first-order approximation the detector effects are treated as a constant detection inefficiency independently of the rate. Consequently, it is assumed that the incident electron rate is gained by calculating the event rate, which is multiplied with a constant factor. The factor is assumed to be independent of the rate itself. The standard approach for calculating the events and thus estimating the rate of incident electrons is simple event counting divided by measurement time.

This chapter investigates if the approximation of a constant detection inefficiency can be assumed over a rate range of four orders of magnitude. The systematic uncertainty of rate estimation due to detector effects is quantified in this context. The underlying data for this study was obtained in the gaseous krypton campaign in 2017.

Chapter 3.1 describes the $^{83\text{m}}\text{Kr}$ -krypton decay mechanism and how krypton is used in the KATRIN set-up. An overview of the three most important detector effects in the measurement phase with krypton is given in section 3.2. Chapter 3.3 focuses on methods to estimate the rate of Poisson distributed electrons. The assumption, if detector effects can be treated as a constant detection inefficiency, is investigated in chapter 3.4 and 3.5 without and with a ROI cut. Additionally, the uncertainty of rate estimation due to detector effects is quantified there. Chapter 3.6 compares the results of the two preceding chapters and draws further conclusions.

3.1. Conversion Electrons of $^{83\text{m}}\text{Kr}$

In order to enable the calibration as well as stability tests in the KATRIN experiment, the excited krypton isotope $^{83\text{m}}\text{Kr}$ is employed. A $^{83\text{m}}\text{Kr}$ source delivers well defined electron energies. Systematic effects and instabilities will result in observable shifts of the measured electron energy or the spectral shape of the electrons [KAT05]. Additionally, the half-life of krypton is relatively small with $t_{1/2} = 1.83\text{ h}$ [McC15], which excludes a long-term contamination of the KATRIN set-up. $^{83\text{m}}\text{Kr}$ has already been used as calibration source in several neutrino experiments [RBS⁺91] [WBB⁺87].

$^{83\text{m}}\text{Kr}$ is generated via decay processes of its mother isotope 83-Rubidium (^{83}Rb) in the KATRIN experiment. ^{83}Rb has a relatively long half-life of 86 days. It decays via electron capture in $^{83\text{m}}\text{Kr}$ in the state with angular momentum $I = 1/2$, negative parity $P = -1$ and half-life of 1.83 h [McC15]. The transition of $^{83\text{m}}\text{Kr}$ to the ground state takes place via either γ -emission or internal conversion. In case of internal conversion, the excited $^{83\text{m}}\text{Kr}$ nucleus interacts with one of the orbital electrons leading to its ejection and a relaxation of the nucleus [Cra12]. However, a direct decay into the ground state of krypton is suppressed, preferred is the decay via an intermediate state with $I^P = 7/2^+$ (see figure 3.1). Thereby,

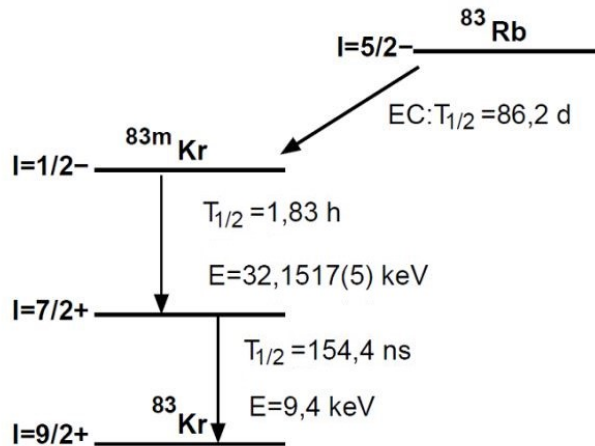


Figure 3.1.: Decay scheme of ^{83}Rb into ^{83}Kr . ^{83}Rb decays via electron capture with a half-life of 82.6 days into the excited $I^P = 1/2^-$ -state of $^{83\text{m}}\text{Kr}$. Via γ -decay or internal conversion, a decay via the intermediate $I^P = 7/2^+$ -state into the ground state of krypton takes place. Adapted from [Ost09].

an excitation energy of $E_{\text{exc}} = 32.2 \text{ keV}$ is released. The intermediate state decays after $t_{1/2} = 154.4 \text{ ns}$ and with an energy release of 9.4 keV into the ground state [McC15].

Measurements, which took place in July 2017, were performed with two types of krypton sources: a gaseous (GKrS) and a condensed krypton source (see chapter A.1). In both cases, the measurement time amounted to one week approximately.

The GKrS is based on the deposition of ^{83}Rb into zeolite beads. Approximately 85% of the produced $^{83\text{m}}\text{Kr}$ emanates into vacuum, whereas ^{83}Rb is bound in the zeolite beads. Consequently, the contamination of the KATRIN set-up with ^{83}Rb is excluded. The emanated $^{83\text{m}}\text{Kr}$ is injected into the WGTS by the gaseous krypton generator [KAT18a]. The GKrS is used to characterise the complete KATRIN set-up. For these measurements, one is interested in the high energy-lines of krypton with narrow width (e.g. $L_3 - 32$). These measurements enable a determination of an upper limit on the electric potential fluctuations in the WGTS [KAT05]. The GKrS delivers electron rates up to several 10^4 cps which are nearly uniformly distributed over the whole detector.

The condensed krypton source appears at the detector as a point-like source and features high count rates. It is used to scan the beamline. Appendix A gives more details about the condensed krypton source.

The goal of this study is the evaluation of the systematic error with regard to the rate estimation over the whole detector. For this reason, only data which was obtained in the GKrS campaign is considered in the following.

3.2. Physics Processes and Read-Out Artefacts in the Focal Plane Detector

There are three major detector effects, which can distort the number of measured events in comparison to the number of incident electrons: charge-sharing, backscattering and pile-up.

An incident electron causes a step-like response in the detector. The pulse-height of this step allows an estimate of the electron energy. Two trapezoidal filters, which are defined via a shaping length L (typically $1.6 \mu\text{s}$) and a gap length G , recognise this step [JK94] [Sch14]. If the time period between two or more electrons which hit the same pixel is smaller than L , the corresponding electrons cannot be distinguished and thus are counted

as a single event. However, it is found that the impact of pile-up is negligible for typical rates of several 10 cps in the neutrino mass measurement of KATRIN [Kor17]. Rates of the krypton measurement phase range up to more than 10^4 cps. In this order of magnitude, pile-up can have a large effect.

Charge-sharing is a side effect of the segmentation of the FPD into several pixels. If an incident electron strikes the FPD near a pixel-boundary, parts of its energy can be deposited in the neighbouring pixel. If the deposited energy in each affected pixel is larger than the electronic threshold, this electron is measured as two events striking the FPD at the same time. The summed-up energy of both events is approximately the one of the incident electron [Sch14]. The probability for charge-sharing varies from 1.5 % for the bulls-eye of the detector to 2.7 % for the outermost pixels [Kor18].

Backscattering describes the effect, if an electron strikes the FPD, deposits parts of its energy and leaves the detector because of (in-)elastic scattering. Due to the electromagnetic design of the detector section, this electron cannot re-enter the main spectrometer. It is reflected and will strike the detector again. The probability for this process depends on the energy and the striking angle of the electron. However, some rough statements can be made. The detector backscattered electron will most likely strike the FPD again after less than $0.2 \mu\text{s}$ and with a position change of less than 0.3 mm compared to the first strike. Therefore, the backscattered electron will usually strike again at the same pixel and with a time difference smaller than the shaping length L [Kor17]. Hence, a large part of backscattered electrons are still measured as one single event at the detector.

Due to the three effects described above, the number of events differs from the number of incident electrons. In case of backscattering and charge-sharing, more events are measured than the amount of incident electrons. A property of the so-called surplus “false events” is that they are measured with a small time difference (in the order of up to several μs) to other events at the detector. In case of pile-up, an event contains two or more incident electrons and therefore lowers the number of events relative to the number of incident electrons. A pile-up event shows no irregularities in its time of arrival, nevertheless it can partly be discriminated by its higher energy.

3.3. Methods for Rate Estimation

The measured rate in the krypton campaign is a superposition of the decay rate of krypton and the background rate. The decay rate of krypton is Poisson distributed. Also the background rate can be assumed Poisson distributed in first-order approximation. The reproductive property of the Poisson distribution states, that a sum of two independent Poisson distributions with expectation value μ_1 and μ_2 results in a Poisson distribution with expectation value $\mu_1 + \mu_2$ [Wal15]. Therefore, it is assumed, that the rate measured with the GKrS is Poisson distributed. Three methods to estimate the rate are presented in the following. Subsequent of the presentation, it will be discussed what can be gained by comparing their results to each other.

3.3.1. Event Counting Divided by Measurement Time

The only model independent method to estimate the rate is the standard approach in the KATRIN framework. Therefore all the events, which are measured at the detector, are counted and divided by the measurement time. This method is denoted with R1 hereinafter. Method R1 counts all measured events as incident electrons, regardless of their true origin as either an incident electron or a detector-induced false event. Consequently, R1 is biased as it assumes a perfect detector without a rate distortion. The left graph of figure 3.2 shows this rate approach.

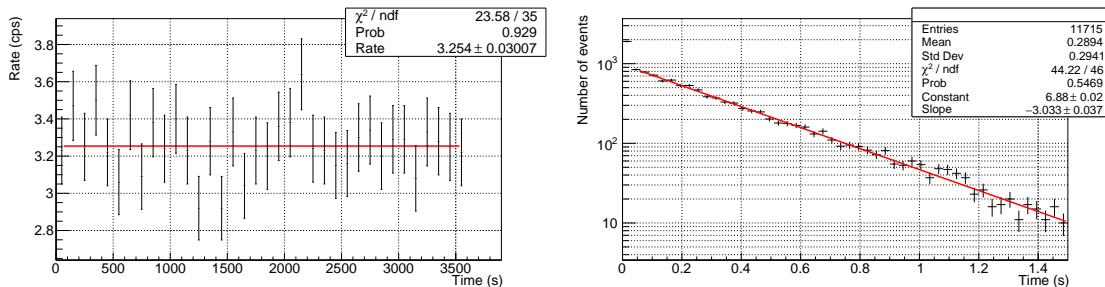


Figure 3.2.: Two methods to estimate the rate shown by example for run 33015. On the left side method R1 is displayed which is simple event counting divided by measurement time. On the right side the inter-arrival time distribution is generated which follows an exponential function. The slope of the exponential function is the negative estimated rate of method R2.

3.3.2. Determination via Multiplicity Plot

This method is only valid for Poisson distributed rates. Consequently, the method is biased as it assumes an underlying Poissonian rate. However, this assumption is justified for data of the GKrS. To determine the rate, the measurement time is split into smaller time ranges. For each time segment, the number of measured events is counted and filled in a histogram, resulting in a so-called “multiplicity plot”. In case of purely Poissonian rates the multiplicity plot is expected to follow a Poisson distribution. By fitting the plot with this distribution, the estimated rate can be calculated. However detector effects will distort the purely expected Poisson distribution and also further correlated effects will falsify this method. Nevertheless, this method will be applied in chapter 3.4 as a test for Poisson distributed events.

3.3.3. Determination via Inter-Arrival Time Distribution

Similar to chapter 3.3.2, the following method can only be used for Poissonian rates and is thus biased in that context. This method determines the rate by the investigation of the time distribution between two consecutive events (a.k.a inter-arrival time distribution). For Poissonian rates, the probability density function of the inter-arrival time distribution follows an exponential function

$$f(t) = Ae^{-\mu t} \text{ [Wal15]}. \quad (3.1)$$

Here, the rate μ is determined by applying an exponential fit to the distribution. This method is denoted with R2 in the following. The right graph of figure 3.2 displays the measured inter-arrival time distribution and the fit of the exponential function.

3.3.4. Comparison of the Methods

A Monte Carlo simulation proves that all three above described methods for rate estimation result in the same rate estimation for Poissonian rates and a perfect detector. However, as the detector is not perfect, the results from the three methods differ. This is caused by a different vulnerability to detector effects.

Method R1 counts all measured events regardless of their true origin as either an incident electron or a false event. In method R2 a discrimination can occur. As mentioned above, false events by charge-sharing and backscattering form a cluster with small inter-arrival times in the order of up to several μs between the measured events. Consequently, the false events influence especially this time range in the inter-arrival time distribution. By excluding the small inter-arrival times in the fit, the influence of these two detector effects

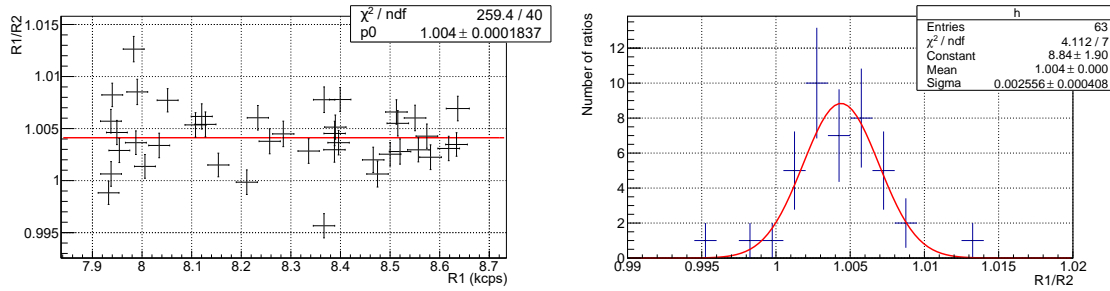


Figure 3.3.: Rate estimation for run 33144. The left graph shows the ratio $R1/R2$ versus the rate, which is fitted with a constant value. The right graph displays the distribution of the ratios, fitted with a Gaussian distribution.

can mainly be eliminated. The comparison of $R2$ with $R1$ allows the quantification of the influence of detector effects on the rate estimation with $R1$. Furthermore, also an investigation, whether the influence of detector effects is constant versus rate, can be performed.

In order to compare the results of $R1$ and $R2$, the ratio $R1/R2$ is calculated for each analysed subrun. Based on the assumption, that the rate estimation is not dominated by detector effects, the expectation value of this ratio amounts to approximately 1.0. In case if the detector effects are independent of the rate, a constant shape of the ratio versus rate is expected. The width of the ratio distribution represents the systematic uncertainty on method $R1$ with regard to the rate estimation. Figure 3.3 shows this approach by example for the subruns of run 33144. The left graph of figure 3.3 shows the ratio versus the rate. The ratio seems constant with a mean value of 1.004. The right graph displays the distribution of the ratio, which can be described by a Gaussian function with standard deviation of 2.55×10^{-3} . The results allow two possible interpretations:

1. As the ratio is constant versus rate, it can be stated that method $R1$ overestimates the rate by a factor of 1.004 due to detector effects. The relative systematic uncertainty of $R1$ is given by 0.255 %.
2. This method is a more Bayesian and conservative approach for the error estimation. The mean value of the ratio is expected to be close to 1.0, thus a penalty term for a deviation of the mean value from the expected value is included. The systematic error estimation of this method includes the deviation of the expectation value and the width of the ratio distribution as the square root of the squared sum:

$$\begin{aligned}
 \sigma_{\text{tot}} &= \sqrt{\sigma_{\text{dev}}^2 + \sigma_{\text{width}}^2} \\
 &= \sqrt{(1 - 1.004)^2 + (2.55 \times 10^{-3})^2} \\
 &= 0.47 \% .
 \end{aligned} \tag{3.2}$$

The correction factor can deviate in dependence of the rate range (see chapter 3.4). The difference of several correction factors can therefore lead to problems, if rate estimations from different rate ranges are compared. To circumvent this problem, method two is favoured over method one. Additionally, the correction factors cannot be defined in some cases due to a strong rate dependence which also favours interpretation possibility two. Hereinafter, the results for both interpretation possibilities are given, by focussing on the second one. In addition, it has to be stated that the ratio of $R1$ and $R2$ does not have to follow a Gaussian distribution as both quantities have statistical fluctuations. The ratio of two Gaussian quantities can result in a Cauchy distribution [Wal15]. In that case, the mean

value is approximated by the median and the 68 %-quantile of the measured distribution is calculated numerically.

In the following the systematic error on R1 is estimated without and with the default ROI cut.

3.4. Systematic Uncertainties without Region-of-Interest Cut

The analysis of this chapter only considers events with energies higher than 10 keV. The post acceleration electrode of the detector is set to 10 kV during the krypton measurement phase. Energies lower than 10 keV are therefore assumed to occur due to detector noise or backscattering. Hardware effects, for example the active pump-out of remnant krypton molecules from the spectrometer volume (see appendix A), can lead to non-Poissonian rates. Such processes are irrelevant for this study. Therefore only those subruns are taken into account in which the inter-arrival time distribution follows the exponential function with a confidence level of 95 %.

961 subruns have been analysed to study the systematic uncertainty on R1 for different orders of magnitude of the rate. The ratios of the subruns versus the rate determined with R1 are plotted in figure 3.4. As first approximation for the ratio uncertainties, the standard error propagation for correlated ratios [Wal15] is applied, even it is not always justified due to the non-Gaussian behaviour stated above. Figure 3.4 shows that the error bars increase with decreasing rate. This behaviour is caused by decreasing statistics, fewer events are counted in a certain time interval than for higher rates. The uncertainty on the rate consequently increases and propagates onto the ratio. The mean value of the ratio versus rate is determined with a χ^2 -fit [Pea34][Pea00] of a constant. However the χ^2 -value is too large for the number of degrees of freedom to describe this behaviour. The graph demonstrates, that the ratios seem to depend on the rate. For that reason the ratios are split by each order of magnitude of the rate and analysed in more detail. Figure 3.5 displays the distributions of the ratios for each order of magnitude of the rate. The systematic uncertainty for each rate range, based on the results of figure 3.5, is stated in table 3.1.

The upper left plot in figure 3.5 shows the histogram of the ratios for rates lower than 100 cps. The distribution can be described with a mean value of 0.968 ± 0.005 and a width of 4.5×10^{-2} . The mean value is significantly smaller than the expectation value. This behaviour is discussed below. However, the ratios are constant versus the rate.

In the range between 10^2 cps and 10^3 cps, the distribution of the ratios does not follow a Gaussian distribution (see figure 3.5 upper right). Nevertheless, the median is near the expectation value and the ratios are constant versus the rate. In the next order of magnitude of the rate, the ratios are also constant versus the rate. The resulting Gaussian distribution has a mean value of 1.008 (lower left graph).

The ratios show a rate dependence for rates higher than 10 keps. The ratios increase with

Table 3.1.: Estimated systematic uncertainties without ROI cut. The first column describes the range of the rate. The second and third column summarises the mean and the width of the ratio distribution for the respective rate range. The fourth column lists, if the ratios are constant versus the rate. The systematic uncertainty is estimated based on the Bayesian approach (see equation 3.2) in the fifth column.

Range (cps)	Mean	Width	Constant versus Rate	Systematic Uncertainty (%)
$10 - 10^2$	0.968	0.045	y	5.48
$10^2 - 10^3$	0.998	0.014	y	1.37
$10^3 - 10^4$	1.008	0.006	y	0.98
above 10^4	1.004	0.005	n	0.67

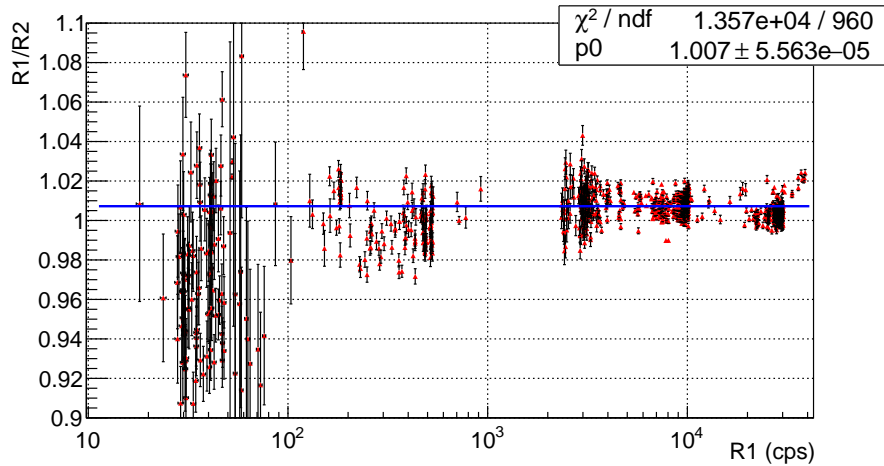


Figure 3.4.: Ratios $R1/R2$ versus the estimated rate. The mean value of the ratios is determined through a fit with a constant. However, the χ^2 -value is too large to assume a constant ratio over four orders of magnitude in the rate.

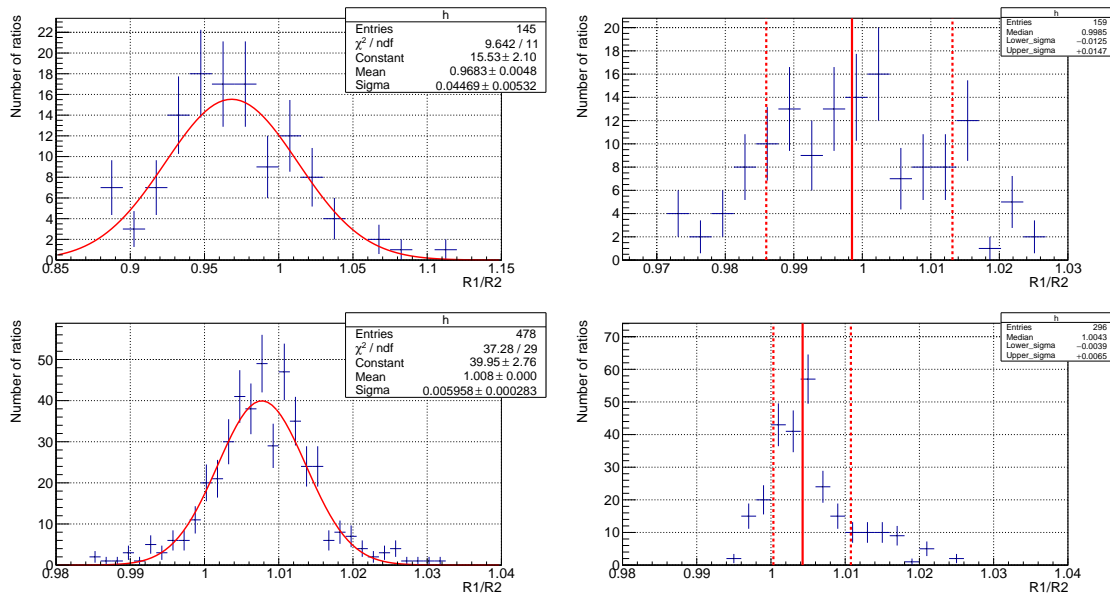


Figure 3.5.: Distribution of ratios $R1/R2$ for each order of magnitude of the rate. The upper left histogram displays the ratio distribution for the rate range below 100 cps, on the upper right side for the range of 10^2 to 10^3 cps. The lower right plot shows the rate range from 1.0 to 10 keps and the lower right one the ratios for rates higher than 10 keps.

rate pointing towards rate dependent detector effects (e.g. dead-time of the detector). This results in an asymmetric distribution of the ratios (lower right graph).

Consequently the ratio $R1/R2$ shows two unexpected behaviours: a significant smaller mean value relative to the expectation value for rates lower than 100 cps and a rate dependence for rates higher than 10 keps.

3.4.1. Ratio for Rates below 100 cps

Small rates in the krypton measurement phase mainly occur at a high retarding potential. The rate and the distribution of the background electrons are assumed to be independent of the applied retarding potential in contrast to the krypton decay electrons. The number of these electrons depends on the retarding potential. Hence, the relative fraction of background electrons, which is partially non-Poisson distributed (e.g. due to radon decays, see chapter 4), increases with the retarding potential. For non-Poissonian rates, method R2 is not applicable to estimate the rate. This results in a flawed rate estimation and might lead to a ratio smaller than 1.0 .

Background measurements show that the spectrometer background rate increases with the radius in the detector plane (see chapter 6.1). The decay electrons of the GKrS are dominant at the centre. To minimise the rate of background electrons and therefore to increase the fraction of Poisson distributed decay events, the rate measured in the three outermost detector rings is excluded in the analysis. In case if the non-Poissonian events cause the too small mean ratio, it should get closer to the expectation value by the ring cut.

The events are projected into a multiplicity plot ($\Delta t = 2.0$ s) and fitted with a Poisson distribution, to test if the measured events are Poisson distributed. This method is applied on a random basis for runs showing rates below 100 cps. The multiplicity plots for both distributions (with and without ring cut) follow a Poisson distribution with 95 % CL. Nevertheless, the ratio distribution is plotted in figure 3.6 with applied ring cut, which might allow the identification of effects which cannot be discovered with the multiplicity plot.

The exclusion of the three outermost detector rings leads to a change of the distribution of ratios (see figure 3.6 compared to figure 3.5). The shape of the resulting distribution is asymmetric with a tail towards smaller ratios and a 68 %-quantile of -0.042 and 0.049.

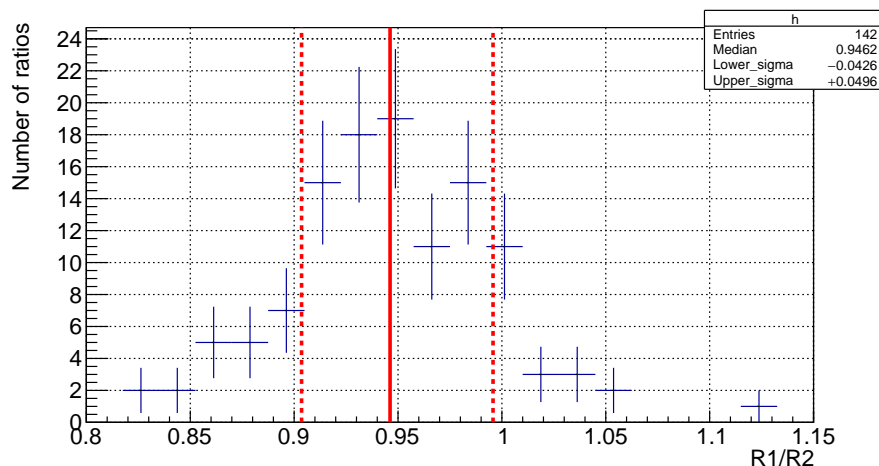


Figure 3.6.: Distribution of ratios $R1/R2$ for rates below 100 cps after exclusion of the outer detector rings. The distribution has 0.946 as median, the 68 %-quantile is -0.042 and +0.049.

The distribution's median decreases slightly with the ring cut (0.95) in contrast to the distributions without cuts (0.96). Consequently, the background rate is probably not the reason for the lowered mean ratio. Further investigations (for example with the standard ROI cut, see chapter 3.5) are needed to gain a better understanding for the reason of this behaviour.

3.4.2. Ratio for Rates higher than 10 kcps

One conceivable reason for the ratio dependence on the rate for rates greater than 10 kcps is given by the different treatment of the methods R1 and R2 with regard to events corresponding to short inter-arrival times. Method R1 handles every measured event as one electron hitting the detector. This is not completely correct due to the occurrence of detector effects.

Runs with high rates are taken at low retarding potential. This allows the conversion electrons at 9 keV and 32 keV of both consecutive $^{83\text{m}}\text{Kr}$ decays to overcome the retarding potential and to arrive at the detector. Additionally, the intermediate state of krypton has only small half-life of 154 ns, which allows the two consecutive electrons to arrive nearly at the same time at the detector. These correlated electrons of cascade decays are counted correctly by R1 if the inter-arrival times of these two electrons is larger than the shaping length of $L \approx 1600$ ns. However, R2 drops the correlated electrons. This results in an increasing ratio R1/R2 with the rate. One possibility to prevent this behaviour is a ROI cut, thereby one of the two $^{83\text{m}}\text{Kr}$ decay peaks is removed (see chapter 3.5). Another option is a so-called multi-pixel cut.

A multi-pixel cut with an exclusion time t_0 removes all measured events with smaller inter-arrival times than t_0 . In this case, R1 will drop the correlated electrons which is assumed to lead to an agreement with R2. Consequently, this should result in a stable ratio for rates higher than 10 kcps. To exclude the cascade decays, a multi-pixel cut with exclusion time larger than the half-life of the intermediate krypton state is needed. In the following analysis t_0 is set to 1 μs .

The dependence of the ratios versus the rate with applied multi-pixel cut is shown in figure 3.7. For rates larger than 21 kcps, the ratio is constant with a mean value of approximately 0.976. The constant behaviour is an evidence, that the increasing ratio is due to the different treatment of R1 and R2 concerning events with little inter-arrival times. For rates smaller

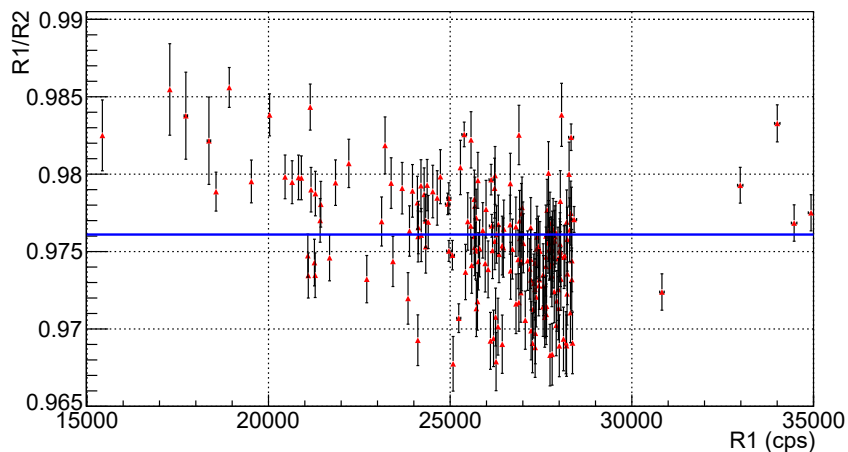


Figure 3.7.: The ratio plotted versus the rate for rates above 10 kcps with applied multi-pixel cut. The ratio can be approximated constant above 25 kcps, though a rate dependent ratio is shown below 25 kcps.

than 21 keps a rate dependent behaviour exists. The ratio decreases with increasing rate, which is due to the removal of the so-called “accidental coincidences”. The multi-pixel cut removes all events with small inter-arrival times, also uncorrelated electrons of the krypton decay. Applying the multi-pixel cut results in an incorrect estimation by R1 by dropping the accidental coincidences and causing the rate dependence below 21 keps. Nevertheless, it is shown, that the ratio dependence of the rate above 10 keps in the GKrS campaign is caused by the correlated electrons of cascade events and not by rate dependent detector effects.

3.4.3. Summarising Table

Table 3.2 summarises the relative systematic uncertainties on the rate estimation, caused by applying method R1. Furthermore, the reaction of the uncertainty is shown, if certain analysis tools are applied. The relative systematic uncertainty within a rate range equals to the width of the distribution. The Bayesian estimation of the systematic uncertainty enables a comparison of different rate ranges and is calculated based on equation 3.2.

Table 3.2.: Estimated systematic uncertainties without ROI cut for several applied analysis tools. In the first column the applied cuts for the uncertainty estimation are listed. The second and third column show the mean values and widths of the ratio distributions. If the ratios are constant versus rate (fourth column) the detector effects can be treated as constant inefficiencies. The results of the Bayesian error estimation are printed in the last column.

Cuts	Range (cps)	Mean	Width	Constant	Bayes Uncert. (%)
No cuts	$10 - 10^2$	0.968	0.045	y	5.48
	$10^2 - 10^3$	0.998	0.014	y	1.37
	$10^3 - 10^4$	1.008	0.006	y	0.98
	above 10^4	1.004	0.005	n	0.67
Outer three rings eliminated	$10 - 10^2$	0.946	0.046	y	7.09
	$10^2 - 10^3$	0.995	0.013	y	1.35
	$10^3 - 10^4$	1.007	0.006	y	0.89
	above 10^4	1.004	0.004	n	0.54
Multi-pixel cut ($1 \mu\text{s}$)	$10 - 10^2$	0.944	0.040	y	6.87
	$10^2 - 10^3$	0.985	0.012	y	1.91
	$10^3 - 10^4$	0.987	0.006	n	1.41
	above 10^4	0.976	0.004	y	2.48
Multi-pixel cut ($10 \mu\text{s}$)	$10 - 10^2$	0.942	0.041	y	7.07
	$10^2 - 10^3$	0.980	0.012	y	2.30
	$10^3 - 10^4$	0.930	0.026	n	7.41
	above 10^4	0.855	0.004	n	14.48

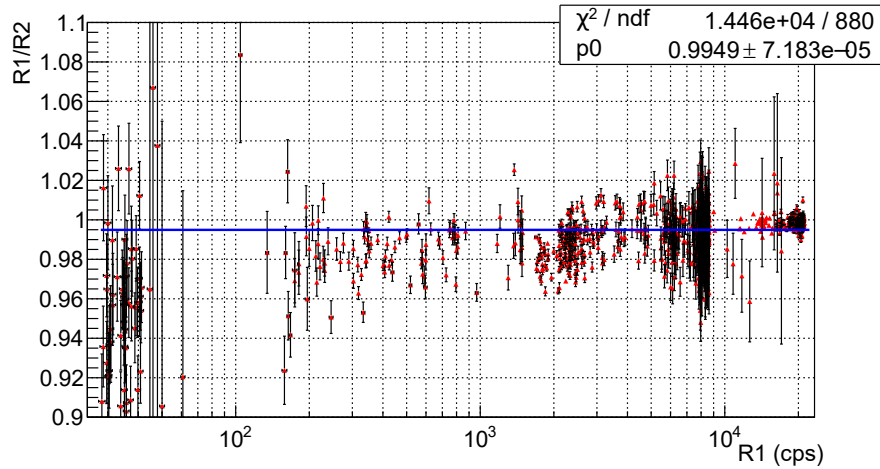


Figure 3.8.: Ratios $R1/R2$ versus the estimated rate with applied ROI cut. The ratios are fitted with a constant. A small trend of increasing ratios with the rate is shown, however it can be neglected versus the wide rate range.

3.5. Systematic Uncertainties in the Region of Interest

This analysis considers only events in the energy region of interest. The ROI is used as defined for the SDS-II measurements (described in chapter 2.3.2). The update of the ROI for the krypton data was decided after performing this study. However, a major impact by updating the ranges of the ROI is not expected.

Similar to the preceding chapter, only those subruns are analysed, in which the inter-arrival time distribution follows an exponential function with a confidence level of 95 %.

Figure 3.8 shows the ratio $R1/R2$ versus four orders of magnitude in the rate in the ROI, which is fitted with a constant. The obtained χ^2 -value of 10^4 with 880 degrees of freedom demonstrates, that the constant behaviour of the ratio does not apply to the whole rate range. The uncertainty on the ratios increase to lower rates because of lower statistics (see figure 3.8) similar to chapter 3.4. The graph indicates a slight increase of the ratios with the rate. This behaviour is neglected for this analysis, as the slope is small over four orders of magnitude of the rate. The distribution and behaviour of the ratios is evaluated for each order of magnitude for further investigations. Figure 3.9 presents the distributions of the ratios split for each order of magnitude of the rate. The resulting systematic uncertainties are shown in the upper section in table 3.3.

The analysis with applied ROI cut shows two important features in comparison to chapter 3.4. First, the distribution of the ratios for rates lower than 100 cps is in mean smaller than the expectation value. $R1$ underestimates the rate by a factor of 0.96 in comparison to $R2$. Possible reasons for this underestimation of the rate are discussed in chapter 3.6. Second, the ratio is constant within each order of magnitude of the rate. It is therefore concluded, that correlated electrons of cascade decays of krypton cause the rate dependence in chapter 3.4. One of the two correlated decay electrons is removed from the analysis by applying a ROI cut, which results in a constant ratio. Due to the constant mean ratios, the influence of detector effects on rate estimation can be treated as constant detection inefficiencies within one order of magnitude of the rate.

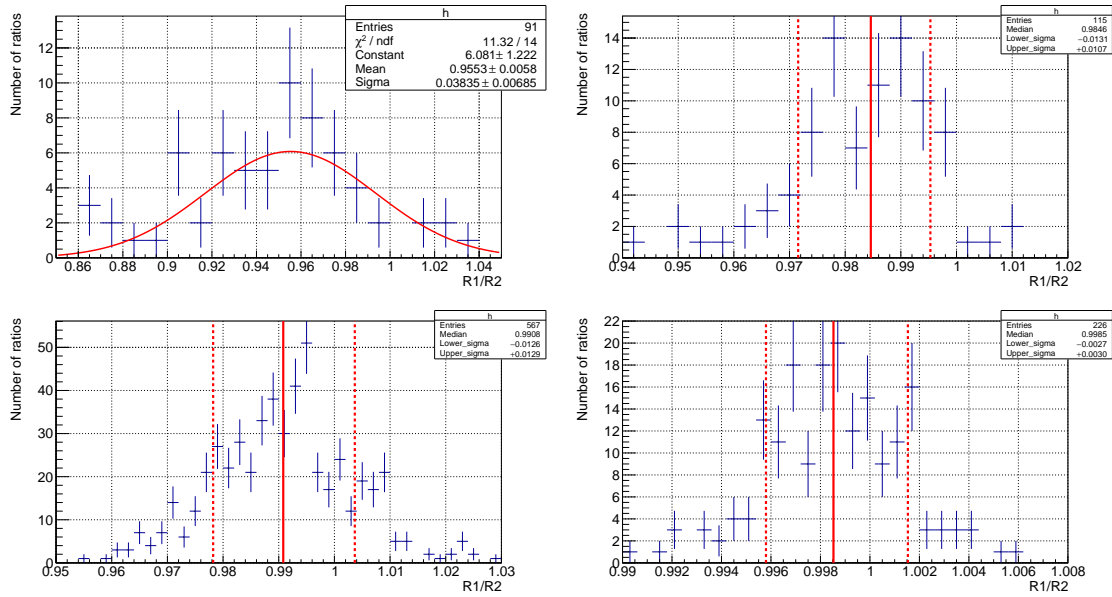


Figure 3.9.: Distribution of ratios $R1/R2$ for each order of magnitude of the rate with applied ROI cut. The upper left histogram shows the distribution of ratios for rates below 100 cps, the upper right for rates between 10^2 cps and 10^3 cps. The lower left graph displays the rate range from 1 to 10 kcps, the lower right for rates higher than 10 kcps.

Table 3.3.: Estimated systematic uncertainties with ROI cut for several applied analysis tools. In the first column the applied cuts for the uncertainty estimation are listed. The second and third column show the mean values and widths of the ratio distributions. If the ratios are constant versus rate (fourth column) the detector effects can be treated as constant inefficiency. The results of the Bayesian error estimation are printed in the last column.

Cuts	Range (cps)	Mean	Width	Constant	Bayes Uncert. (%)
No Cuts	$10 - 10^2$	0.955	0.038	y	5.89
	$10^2 - 10^3$	0.984	0.010	y	1.94
	$10^3 - 10^4$	0.991	0.013	y	1.57
	above 10^4	0.999	0.003	y	0.32
Outer three rings eliminated	$10 - 10^2$	0.934	0.038	y	7.64
	$10^2 - 10^3$	0.983	0.014	y	2.21
	$10^3 - 10^4$	0.992	0.010	y	1.27
	above 10^4	0.999	0.003	y	0.29
Multi-pixel cut ($1 \mu\text{s}$)	$10 - 10^2$	0.945	0.042	y	6.89
	$10^2 - 10^3$	0.983	0.014	y	2.25
	$10^3 - 10^4$	0.986	0.010	y	1.72
	above 10^4	0.980	0.004	y	2.02
Multi-pixel cut ($10 \mu\text{s}$)	$10 - 10^2$	0.945	0.042	y	6.89
	$10^2 - 10^3$	0.978	0.013	y	2.58
	$10^3 - 10^4$	0.941	0.022	n	6.30
	above 10^4	0.873	0.008	n	12.72

3.5.1. Summarising Table

Table 3.3 presents the relative systematic uncertainty on R1 in the region of interest for several applied analysis tools. The conservative Bayesian estimation of the systematic error as well as an overview of applied cuts are summarised. The ratios are constant versus the rate, except if a multi-pixel with $t_0 = 10 \mu\text{s}$ is applied. Consequently, the approximation of treating the influence of detector effects as constant detection inefficiencies seems justified within each order of magnitude for an applied ROI cut.

3.6. Underestimation of the Rate by R1 below 100 cps

One important similarity between the analysis with and without ROI cut is the lowered ratio for smaller rates relative to the expected value. The test for Poissonian rates and the exclusion of the outer detector rings precludes non-Poissonian background as a possible source for the underestimation of the rate by R1.

A further reasonable source is given by the energy of the conversion electrons. Runs with low rates correspond to a high retarding potential and hence to conversion electrons with higher energy. These electrons are accelerated by the high retarding potential after passing the analysing plane. This results in a higher energy at the detector than runs with low retarding potentials and high rates. Figure 3.10 shows the results of simulations for the energy dependence of backscattering and charge-sharing as the major detector effects, which influence this analysis. The upper graph displays the primary backscattering coefficient η versus the initial energy of the conversion electrons. The typical energy range for krypton conversion electrons is between 7 and 40 keV. η shows a slowly decreasing behaviour in this energy range, consequently also the probability for backscattering decreases. However, η is dominated by the striking angle of the electrons at the detector and not by the energy dependence. The lower graph shows the probability for charge-sharing as a function of the ring number of the detector. The probability is calculated for 30, 40, 50 and 60 keV striking energy of the electrons. It is shown, that the probability for charge-sharing increases with striking energy.

Consequently the probability for backscattering slightly decreases with electron energy whereas for charge-sharing an increasing behaviour is shown. The dependence on the electron energy is however not strong in both effects. Therefore, a reason for the lowered ratio R1/R2 for low rates could not be identified.

3.7. Conclusions

The systematic uncertainty of rate estimation by event counting divided by measurement time due to detector effects is quantified. The investigation is performed based on the assumption of Poissonian rates. The most important results are:

- The Bayesian estimation of systematic uncertainty is between 5.48 and 0.67 % in the analysis without ROI cut. A dependence of the rate estimation is seen to rates higher than 10 kcps, which is not caused by detector effects but by correlated cascade decays of krypton.
- The systematic error on the rate estimation is between 5.89 and 0.32 % in the standard analysis with ROI cut. The ratios show a constant behaviour for each order of magnitude in the rate. This allows to assume detector effects to be independent of the rate, which enables to treat them as a constant detection inefficiency.
- An underestimation of the rate by R1 is seen for rates below 100 cps in the analysis with and without ROI cut. The reason for this could not be identified.

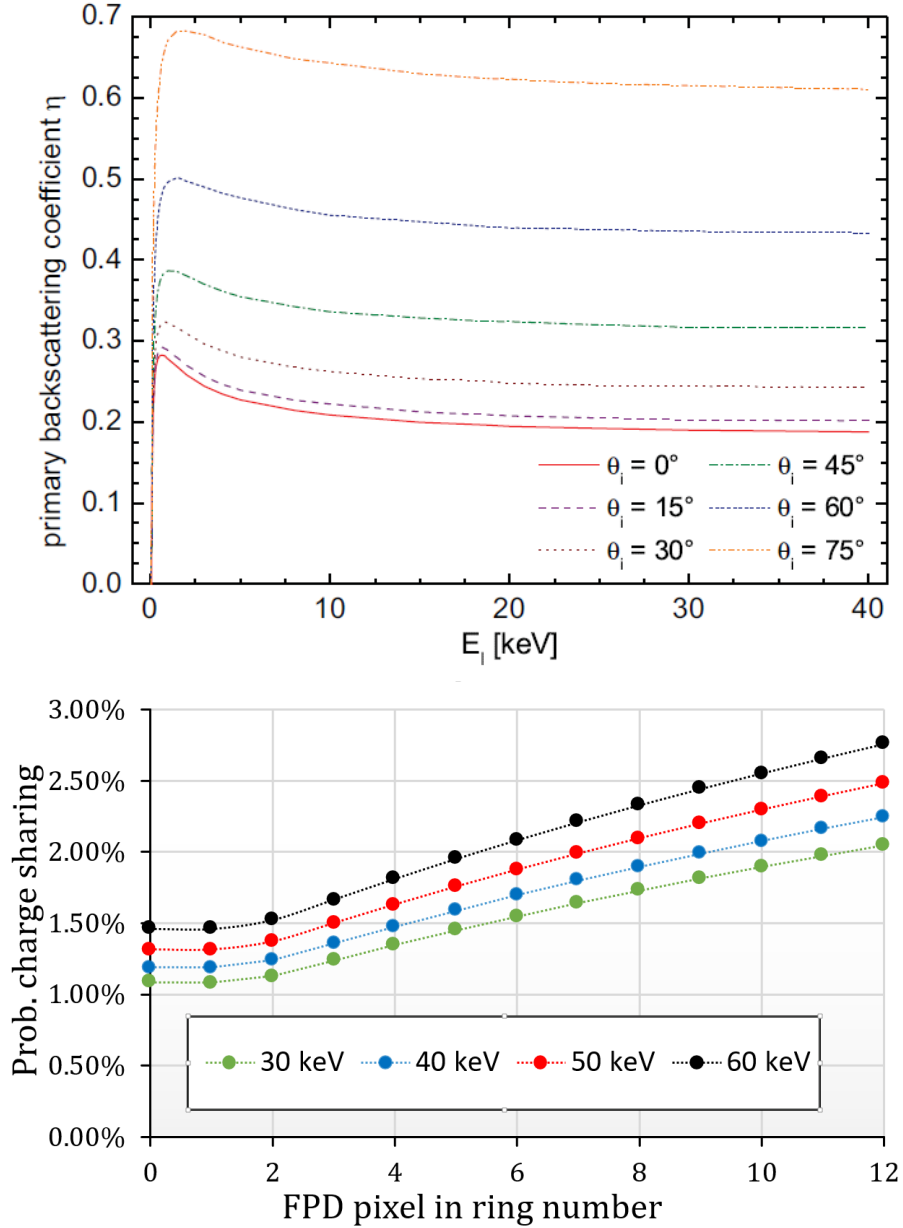


Figure 3.10.: The probability for backscattering and charge-sharing for different electron energies. The upper graph presents the primary backscattering coefficient η versus the electron energy for several striking angles. η decreases with increasing energy, however it is dominated by the striking angle [Ren11]. The lower graph displays the probability for charge-sharing versus the detector rings for several striking energies. The probability for charge-sharing is increasing with the electron energy [Kor18].

4. The KATRIN Background Model

Electrons produced in background processes influence the statistical uncertainty of the KATRIN experiment (see chapter 2.3.4). According to the KATRIN design report, the achievement of a background rate of 0.01 cps is mandatory in order to reach the aimed sensitivity of 200 meV (90 % CL) on the neutrino mass [KAT05]. The measured background rate in the SDS is factor 50 higher than the design value with a magnetic field setting, which provides the optimal energy resolution of 0.93 eV in the main spectrometer. Consequently, the background rate needs to be minimised to ensure maximal sensitivity on the neutrino mass. In addition, the different background sources have to be characterised to predict their time development over the total measurement time of five years. This chapter describes the different known background sources of the SDS as well as their influence on the electron ROI rate. Furthermore, possible reduction mechanisms are explained. The major part of the background rate is generated in the main spectrometer. Figure 4.1 gives a schematic overview of the known background sources. The trapping mechanism of electrons is of fundamental importance for the understanding of background processes.

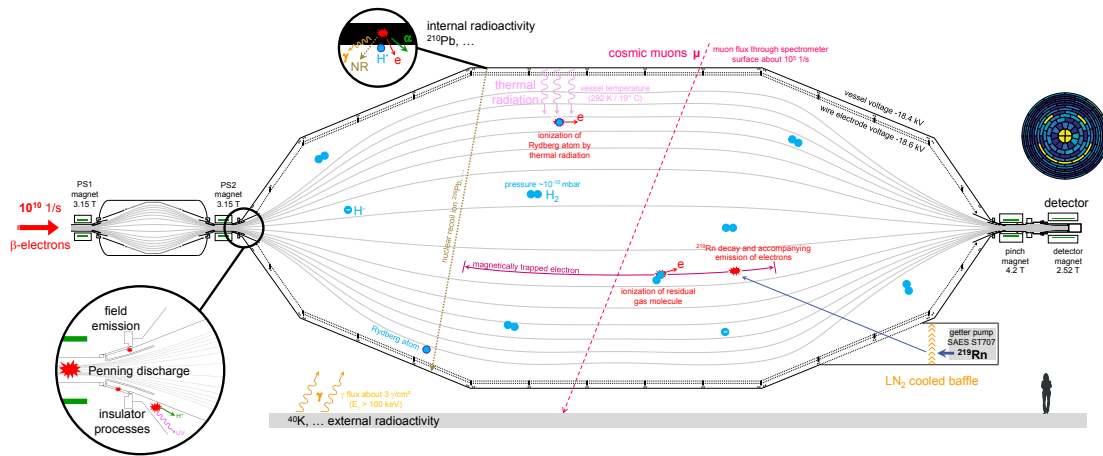


Figure 4.1.: Overview of the known sources of background in the main spectrometer. External background sources are cosmic muons and γ 's as part of the natural radioactivity. They hit the spectrometer vessel and can produce secondary electrons on the inner surfaces. The non-evaporable getter pumps emanate radioactive ^{219}Rn , which can decay in the sensitive flux tube and thereby produce trapped electrons. A Penning discharge is possible for the Penning trap formed between pre- and main spectrometer. ^{210}Pb is implanted in the spectrometer vessel, which produces in the course of its decay Rydberg atoms [FK17].

4.1. Magnetically Stored Electrons

Electrons can be reflected by the magnetic mirror when travelling from weak to strong magnetic fields, as described in chapter 2.2. Background electrons, which are produced in the weak magnetic field near the analysing plane, can be trapped in the so-called magnetic bottle. A fraction of the electrons is reflected on both ends of the spectrometer, as the magnetic field strength increases towards both ends.

The probability of an electron to be stored depends on its kinematics. A background electron is trapped in the magnetic bottle if its polar emission angle at its point of creation relative to the magnetic field lines is larger than

$$\theta_{\max} = \arcsin \left(\sqrt{\frac{q|U(\vec{x})|}{E_{\text{kin}}(\vec{x})} \cdot \frac{B(\vec{x})}{B_{\max}}} \right). \quad (4.1)$$

Here, $E_{\text{kin}}(\vec{x})$ describes the kinetic energy of the background electron at the point of creation, $U(\vec{x})$ the electric potential, $B(\vec{x})$ the magnetic field strength and B_{\max} the maximal field strength along the flight path.

An electron, which cannot exit the magnetic bottle due to its polar emission angle, moves in axial direction back and forth in the spectrometer. It follows the magnetic field lines on fast, small-diameter cyclotron paths. Additionally, the slow azimuthal magnetron drift of the electron takes place, which is caused by radial magnetic field gradients [CGR06] [Mer12]. A stored electron goes through a cooling-down process in which it either loses enough energy by synchrotron radiation to break the storage condition or it scatters with residual gas and thereby changes its polar angle. The energy loss due to synchrotron radiation is dominant for background electrons with $E_{\perp} > 10$ keV. Low-energy electrons are more likely to break the storage conditions by (in-)elastic scatter processes with residual gas.

In case of inelastic scattering, secondary electrons are produced via ionisation processes. One stored electron with an energy of $\mathcal{O}(1 \text{ keV})$ can generate up to hundreds of secondary electrons. Secondary electrons, which are created near the analysing plane and possess small energies, are adiabatically guided to the detector. Due to the fact, that such electrons are accelerated by the retarding potential towards the detector, they cannot be distinguished from β -signal electrons. Excellent vacuum conditions in the main spectrometer yield relatively long storage times of background electrons, that can range up to several hours [MDF⁺13].

High-energy electrons ($E > 10$ keV) can undergo two further processes, which enable them to break the storage condition. The first option is that the cyclotron radius is larger than the spectrometer vessel and the electrons hit the inner surfaces. The second option is that due to non-adiabatic effects the orbital magnetic moment of the electrons are no longer conserved allowing them to leave the magnetic bottle [Har15] [MDF⁺13].

Several possibilities exist to remove trapped electrons from the main spectrometer, for example by applying an electric dipole or a magnetic pulse [Wan13].

Another possible method to remove stored electrons is based on stochastic heating by electron cyclotron resonance. Therefore an external high frequency field is applied. Its frequency is adjusted to match the cyclotron frequency of the stored electrons. If the cyclotron frequency is met, the trapped electrons gain a small amount of energy by the external field. Stored electrons pass the analysing plane up to 10^4 times within 10 ms. By applying the external field in the central part of the spectrometer, these electrons gain a certain amount of energy each time they pass the analysing plane. Consequently, the cyclotron radii of those electrons increase. Once the radius exceeds the dimension of the spectrometer, the corresponding electron is absorbed on the inner surface of the spectrometer [MBB⁺12].

4.2. Cosmic Muons

Hadronic showers in the atmosphere produce cosmic muons [GER16]. The main spectrometer vessel is exposed to a flux of about 10^5 muons per second, which can cause the emission of secondary electrons from the inner surfaces [FK17] [Lei14]. Electromagnetic reduction mechanisms avoid a direct propagation of these secondary electrons into the sensitive spectrometer volume.

The magnetic field is mostly parallel aligned to the inner surfaces of the spectrometer. Due to the orientation of the field, secondary electrons are forced on a cyclotron path by the Lorentz force and guided into the walls. Deviations from the parallel alignment can trap secondary electrons at the outermost magnetic field lines. However, these electrons are not guided to the detector. An ideally designed magnetic shielding provides a reduction factor of five orders of magnitude on the secondary electron rate [Wan13].

Nevertheless, due to non-adiabatic transport effects of secondary electrons, a drift into the sensitive volume of the main spectrometer can take place. This process can happen with a probability of up to 10^{-5} for electrons starting from the hull. Wire electrodes have been installed in both spectrometers in order to minimise the rate for such a process. The inner electrodes cover the entire inner surface of the spectrometer vessels and are operated at more negative voltage than the vessel. This results in a retarding potential for negative charged particles emitted by the inner surfaces [Val10]. In the normal operation mode, the inner electrodes are at 200 V more negative potential than the spectrometer vessel. A larger offset would lead to a more reduced rate of secondary electrons from the inner surfaces [Har15]. However this would also lead to stronger inhomogeneities of the electric field in the analysing plane. Furthermore, field electron emission can take place above a certain inner electrode voltage. In this process, electrons leave the electrodes by the tunnel effect and produce additional background [Har15] [Sch14].

A muon detection system is installed close to the main spectrometer to quantify the influence of the muon flux onto the background rate in the standard ROI. A correlation analysis was performed with the measured muon flux and the background electron rate with the data of a long-term background measurement. The correlation factor is consistent with zero and the fraction of muon-induced background events is quantified to $(4.8 \pm 4.9)\%$ [CDE18]. The electromagnetic shielding is hence sufficient to eliminate the influence of cosmic muons on the background rate in the ROI.

4.3. Penning Traps

Charged particles can be captured by a special interplay of electric and magnetic field in Penning traps. A strong magnetic field traps charged particles in radial direction and a static electric field in axial direction [Bla06]. Penning traps are created in KATRIN along the magnetic flux tube, where the electric potential has a minimum (for example close to the inner electrode system). In the electromagnetic design of the main spectrometer it has been taken care to avoid Penning traps [Mer12].

Between the pre- and main spectrometer a so-called Penning-Malmberg trap is formed. Thereby the magnetic field lines go from one negative potential to another with a positive potential well in the middle. Background electrons, which do not possess enough kinetic energy to overcome the potential, will accumulate in the trap. The mean free path of an electron in the Penning trap reaches up to several kilometres since the spectrometer provides good vacuum conditions. One trapped primary electron can produce up to 10^8 secondary electrons, charged particles and photons by ionisation processes in a 18 keV deep Penning trap [FGV⁺14]. The trap stores the secondary electrons, whereas positive ions and photons can leave it. They can then ionise residual gas or hit the inner surfaces. Such processes yield a higher background rate. A charged plasma with negative space charge

can arise, due to the long storage time of electrons in the Penning trap, which distorts the electrostatic field design [FGV⁺14]. In extreme cases, the unstable plasma can lead to a vacuum breakdown (Penning discharge) resulting in a clearly elevated background rate (>1 keps) [Har15]. Penning discharges are excluded as source of background events in the KATRIN set-up by dedicated measurements [FK17].

4.4. Radon Decay

First measurements with the pre-spectrometer indicated a contribution of background events from radioactive decays of certain radon isotopes inside the spectrometer volume [FBD⁺11]. Noble gases, such as radon, are not influenced by electromagnetic fields in vacuum and can therefore not be shielded by them. The radon isotopes ^{219}Rn , ^{220}Rn and ^{222}Rn are part of the primordial decay chains and thus part of the naturally occurring radioactivity. Furthermore, the non-evaporable getter (NEG) material, which is installed in both spectrometers to achieve good vacuum conditions, is a known source of radon emanation. The short-lived isotopes ^{219}Rn and ^{220}Rn with half-life in the order of seconds decay homogeneously via α -decay in the spectrometer. The long-lived isotope ^{222}Rn is usually pumped out of the spectrometer before its decay and is therefore not considered in the following. However, ^{222}Rn influences indirectly the background, as will be pointed out in chapter 4.5 [Har15].

Low level γ -measurements lead to the conclusion, that the contribution of ^{220}Rn to the background rate is two orders of magnitude smaller than the fraction of ^{219}Rn induced by the NEG material [Frä10]. Therefore the focus of the following discussion is on ^{219}Rn decay.

^{219}Rn decays via α -decay in ^{215}Po . The emitted α -particle does not contribute to the generation of background electrons, since its cyclotron radius exceeds the dimensions of the main spectrometer. The α -particle can produce charged particles in the collision with the inner surface, however they are effectively shielded by the electromagnetic shielding. Nevertheless, processes accompanying the ^{219}Rn decay like inner-shell shake-off, atomic relaxation or atomic-shell reorganisation yield to an emission of electrons. This is a consequence of the transition of the excited ^{215}Po nucleus to its ground state. In this way, up to twenty electrons with an energy range of few eV to multi-keV can be emitted in the sensitive flux volume by a single radon decay. Depending on the energy and emission angles, the magnetic bottle can trap the primary electrons. The trapped electrons can produce up to hundreds of secondary electrons in the cooling-down process. These secondary electrons can reach the detector and elevate the background rate in the electron ROI [WDF⁺13] [Har15].

Additionally to elevating the background rate, the stored high-energy electrons of radon decays significantly worsen the KATRIN sensitivity. The statistical uncertainty on the squared neutrino mass scales approximately with $\sim N_{\text{bkg}}^{1/6}$ in case of Poissonian background rates [KAT05] [Ott94]. Secondary electrons produced by a single stored primary electron are correlated and thus not Poisson distributed. The statistical sensitivity was calculated for a full-beam measurement time of three years with Monte Carlo simulations. The maximal KATRIN sensitivity was determined to $m_\nu > 160$ meV (90 % CL) for a purely Poissonian background rate of 10 mcps. A large contribution of secondary electrons produced by radon decays (total rate 60 mcps) worsens the sensitivity to $m_\nu > 370$ meV [MDF⁺13]. This calculation underlines the necessity of radon reduction mechanisms in the spectrometer.

The NEG material is the major source of radon in the spectrometers. A LN₂ cooled baffle system is installed in the three pump ports to prevent a direct line of sight from the NEG pump to the sensitive flux volume. This shall actively reduce radon in the main spectrometer. The baffle system is cooled to approximately 80 K to absorb radon on its

surfaces. Thereby, the baffle system suppresses the radon induced background of 500 mcps with an efficiency of 95 % [Har15]. No baffle system is installed in the pump ports of the pre-spectrometer due to the lower area of NEG material. The radon atoms emitted there can enter the sensitive spectrometer volume uninterruptedly, measurements to quantify this influence are ongoing.

4.5. Natural Radioactivity

The natural radioactivity deposited in the material of the spectrometer building results in a γ -ray flux to which the spectrometers are exposed. A ^{60}Co source with an activity of 53 mBq [FK17] was placed near the main spectrometer vessel, to test if the γ -flux influences the background rate. The rate in the main spectrometer stayed constant despite of the source, consequently background events induced by γ -ray flux are effectively shielded [FK17].

A long-term measurement at the end of 2014 indicated radioactive ^{210}Pb at the inner surfaces of the main spectrometer. In the design process of the spectrometer vessel and the inner electrode system, it was taken care to use only materials with high radio purity. Furthermore the inner surfaces of the spectrometer were electropolished after the production, eliminating nearly all traces of ^{210}Pb . Based on these countermeasures, it can be concluded that the deposition of ^{210}Pb must have occurred either during or after the installation of the main spectrometer at KIT.

^{210}Pb is a part of the primordial decay series of ^{238}U . Hence, it is a decay product of the long-lived radon isotope ^{222}Rn . ^{222}Rn is a noble gas and can easily diffuse to the surface of materials and emanate into the ambient air. During the construction and maintenance phase from 2007 to 2012 the spectrometer vessel was vented to atmosphere and therefore its surfaces exposed to ^{222}Rn . There are several α -decays in the decay chain of ^{222}Rn to ^{210}Pb . The daughter nucleus gains a recoil energy in each α -decay and can therefore be implanted several nanometres deep into the spectrometer vessel or the inner electrode system. The decay of ^{222}Rn to ^{210}Pb takes place within a few minutes, whereas ^{210}Pb itself has a half-life of 22.2 years [Bas14]. The main spectrometer was vented to air only three times since 2012. Therefore, it can be assumed in first-order approximation, that the only implanted daughter nucleus of ^{222}Rn is currently ^{210}Pb .

The influence of the β -decay electrons of ^{210}Pb onto the background rate near the endpoint of tritium is investigated in [Har15]. A direct contribution from low-energy β -electrons seems negligible due to the electrostatic and magnetic shielding. An indirect small contribution of the β -decay due to storage of high-energy shell conversion electrons towards the outer spectrometer region is probable [Har15].

4.6. Rydberg Atoms

All background effects mentioned above are effectively shielded and only contribute below or on a percent-level to the overall KATRIN background. However, the major source of the main spectrometer background with a rate of $\mathcal{O}(10^2)$ mcps remains unidentified. The current background model labels Rydberg atoms accompanying the decay of ^{210}Pb as major source of the background rate near the endpoint of tritium [FK17].

The thesis of F. Harms [Har15] states, that the amount of measured background events mainly depends on the observed sensitive volume rather than on the applied magnetic field strength in the spectrometer. This implies, that the background electrons are approximately homogeneously distributed over the volume of the spectrometer. The electrons need to have low energy at their point of creation to contribute to the background near the tritium endpoint. A neutral particle is needed as source of the background. The neutrality of such a particle is prerequisite since otherwise it would be affected by the internal shielding. The

particle needs to be in a metastable state, to emit a low-energy electron in the sensitive flux volume [Tro18]. The most likely process is the production of Rydberg atoms which are ionised in the volume of the spectrometer by thermal radiation [FK17].

Rydberg atoms are in states of high principal quantum number n with lifetimes in the order of milli-seconds. The Rydberg atoms in KATRIN are generated as a consequence of α -decays near the surface of the spectrometer vessel. As previously mentioned, ^{210}Pb is implanted into the inner surfaces of the spectrometer as a consequence of contamination with ^{222}Rn . ^{210}Pb decays into ^{210}Bi via β -decay, which then decays into ^{210}Po . During the α -decay of ^{210}Po , the daughter nucleus gains a recoil energy $\mathcal{O}(100\text{ keV})$. This recoil allows the daughter nucleus to leave the surface and to sputter atoms on the inner surfaces of the spectrometers. As result of the scattering process, a part of the atoms is excited in Rydberg states with high quantum numbers [Tro18].

Due to the high principal quantum number state, Rydberg atoms have a large dipole moment and react to electromagnetic fields. Considering an electric field corresponding to the applied voltage U_{app} , Rydberg atoms with principal quantum numbers larger than

$$n_{\text{max}} = \left(\frac{27.4\text{ V}}{16 \times U_{\text{app}}(\text{V})} \right)^{1/4} \quad [\text{Gal05}] \quad (4.2)$$

are ionised. A large fraction of Rydberg atoms are produced on the inner vessel surface. An electrostatic field is created between the vessel and the inner electrodes by which a part of the Rydberg states are ionised according to equation 4.2. The residuals of the ionised atoms are then absorbed by the electromagnetic shielding. Hence, a decrease of the rate is expected with increasing inner electrode offset, which is experimentally confirmed [Har15]. The lifetime of the remaining Rydberg states is sufficient to enter the sensitive flux volume of the main spectrometer. There, the black-body radiation of the spectrometer can ionise the atoms. The retarding potential accelerates the resulting low-energy electron, which then causes an indistinguishable background from the signal electrons near the endpoint of tritium [GNO10] [Har15].

An attempt to reduce the background rate by ionisation of Rydberg atoms was given by baking-out the pre- and main spectrometer. The spectrometers were heated to 200°C (main spectrometer) respectively 300°C (pre-spectrometer) for several consecutive days [Thü17] [Thü18]. Sputtering processes of recoil nuclei with atoms on the inner surfaces of the spectrometers produce the Rydberg atoms in KATRIN. These atoms are mainly H_2O molecules, which accumulate on the inner surfaces in monolayers. During the bake-out process, the accumulated atoms on the inner surfaces were evaporated and pumped out, which lowers the probability for the Rydberg atom production [Har15]. The bake-out process lowered the background rate in the ROI by approximately 40%.

Despite the experimental evidences, which favour the Rydberg model as background source, there are also effects, which can partially not yet be explained by it. One example is the energy distribution of background electrons in the main spectrometer, which is investigated via dipole measurements. The maximally allowed electron energies for ionised Rydberg atoms by black-body radiation range up to 100 meV . However, dipole measurements indicate that background electrons can have starting energies up to 1 eV [Pol18].

4.7. Intrinsic Detector Background

The design goal of the detector system is to reach an intrinsic detector background rate, which is lower than 1 mcps near the endpoint of tritium [KAT05]. Active (multi-pixel cut, veto cut) and passive (selection of materials) background-reduction techniques are applied to enable the achievement of this goal [Leb10]. Measurements with a closed valve

between the detector section and the main spectrometer enable a determination of the intrinsic detector background rate. The post-acceleration is turned off in this measurement, since otherwise low-energy surface electrons of the valve would be accelerated towards the detector. The measured energy spectrum contains four features:

- The electronic noise dominates the measurement below 6 keV, resulting in a peak-like structure.
- Fluorescence light from surrounding materials dominates the range from 10 to 110 keV. In this range, the background rate drops exponentially.
- At approximately 125 keV, a rise in the spectrum can be recognised and described with a Landau distribution. This observation can be explained by cosmic rays, for example muons, passing through the FPD and depositing parts of their energy.
- A broad peak exists above 180 keV, which is due to overflow.

Through the combination of active and passive shielding techniques, the design goal of the background rate for the detector section is fulfilled with a post acceleration of 10 kV [Sch14].

4.8. Conclusions

The background rate produced in the spectrometer and detector section in the electron ROI is many times higher than required in the design report. Many efforts have been made to identify the sources of this elevated background. It was found that secondary electrons due to cosmic muons are well shielded and influence the background rate only at the percent level. Furthermore, Penning traps could be excluded as source of background. The radioactive radon isotopes ^{219}Rn and ^{220}Rn worsen the sensitivity of the KATRIN experiment by producing high-energy electrons, which are trapped in the spectrometers. A LN_2 cooled baffle system effectively shields radon in the main spectrometer in contrast to the pre-spectrometer. A γ -ray flux of the intrinsic radioactivity of the building material causes the emission of secondary electrons from the inner spectrometer surfaces. The electromagnetic shielding absorbs these electrons. Further measurements showed the existence of ^{210}Pb atoms in the vessel material of the main spectrometer. The major source of the background rate is assumed to be Rydberg atoms, which are produced accompanying the decay of ^{210}Pb . The black-body radiation of the spectrometers can ionise the Rydberg atoms in the sensitive flux volume of the spectrometer and produce a low-energy electron in the sensitive flux volume. Several measurements underpin this theory, however there are still observations which cannot be explained by the Rydberg model. The intrinsic detector background rate fulfils the requirements of the design report.

5. Voltage Dependence of the Main Spectrometer Background near the Endpoint of Tritium

The KATRIN design report assumes that the background rate is independent of the applied retarding potential near the endpoint of tritium [KAT05]. The thesis of F. Harms [Har15] investigates the rate dependence on the retarding potential over a wide range (from approximately 40 eV to 1.8×10^4 eV). An increasing background rate with the retarding potential is measured and the reason for this dependence remains unknown. The goal of this chapter is to answer if the spectrometer background rate can be assumed constant for the scanning range of the neutrino mass measurements (35 eV or 65 eV, depending on scenario).

Chapter 5.1 summarises sensitivity studies of the voltage dependence of the background rate, which were performed in the course of the KATRIN design report. Afterwards a mechanism, which might cause a dependence of the background rate, is stated in chapter 5.2. The following chapter 5.3 presents the experimental results of a measurement performed in October 2017 to this topic. Chapter 5.4 shows the results of two further measurements, both performed in January 2018, and the inconsistencies which occurred in there. The subsequent chapter 5.5 presents three possible ways to treat the measured voltage dependence and their influence on the KATRIN sensitivity.

5.1. Voltage Dependence in the Design Report

Different scenarios have been simulated to calculate the optimal measurement time distribution for the determination of the neutrino mass. In most of the cases, the retarding potential is varied from 30 eV or 60 eV below the endpoint of tritium to 5 eV above. A decision for a final measurement time distribution is not yet made. The KATRIN design report assumes the background rate to be independent of the retarding potential for the scanning range in neutrino mass measurements. It assumes, that in case of a voltage dependence, it can be described as a first degree polynomial in first-order approximation. This assumption is also taken over for the following sensitivity studies in this chapter. The rate R is thus described in dependence of the retarding potential qU by

$$R(qU) = \delta \cdot qU + R_{\text{off}} , \quad (5.1)$$

with δ as the slope of the potential dependence and R_{off} as the extrapolated rate without retarding potential.

Sensitivity studies have been performed to test the influence of the voltage dependence on the neutrino mass. In these studies, the squared neutrino mass is set to 0 eV^2 and the decay spectrum of tritium is simulated based on this value. The simulated decay rates are then added to the data set as well as a background model, which contains a dependence of

the background rate on the retarding potential with a certain slope. The background is assumed to be constant in the model, which is fitted to the simulated data set. By fitting an incomplete model to the data set, the fitted squared neutrino mass is shifted versus the “true” value. The shift is the systematic shift on the squared neutrino mass caused by neglecting a possible background dependence.

As result of the sensitivity studies performed for the design report, a critical slope of the background dependence is determined to $\delta = 2.5$ mcps/keV. With an assumed background rate at the endpoint of tritium of 10 mcps, this slope leads to a shift on the squared neutrino mass larger than the maximally allowed systematic error for one systematic effect ($\approx 6 \times 10^{-3} \text{ eV}^2$). The upper limit on the background dependence in the Troitsk neutrino experiment was measured above the endpoint to 0.5 mcps/keV. Based on this value, a possible background dependence is linked to a systematic shift on the squared neutrino mass smaller than $1.2 \times 10^{-3} \text{ eV}^2$ in the KATRIN systematic error budget. Thereby the constant underlying background is assumed to be 10 mcps [KAT05].

5.2. Model for Voltage Dependence

This chapter explains a mechanism, which can cause a dependence of the background rate on the applied retarding potential. The main spectrometer background is dominated by electrons, which are produced in the ionisation process of Rydberg atoms (see chapter 4.6). Their emergence only depends on the decay of ^{210}Pb near the inner surfaces of the spectrometer, which is independent of the applied vessel potential. An ionisation of certain Rydberg states directly after their creation is only dependent on the offset between the inner electrode system and the vessel potential. This offset is constant during a measurement. Consequently, the spectrum of Rydberg atoms is independent of the applied retarding potential. The black-body radiation of the main spectrometer ionises the Rydberg atoms and produces thereby the free low-energy background electrons. This radiation only hinges on the vessel temperature [TM15]. In summary, the production of background electrons by Rydberg atoms is independent of the applied retarding potential.

The production mechanism of background electrons cannot explain a possible voltage dependence, thus it might only be caused after the production and before the detection of

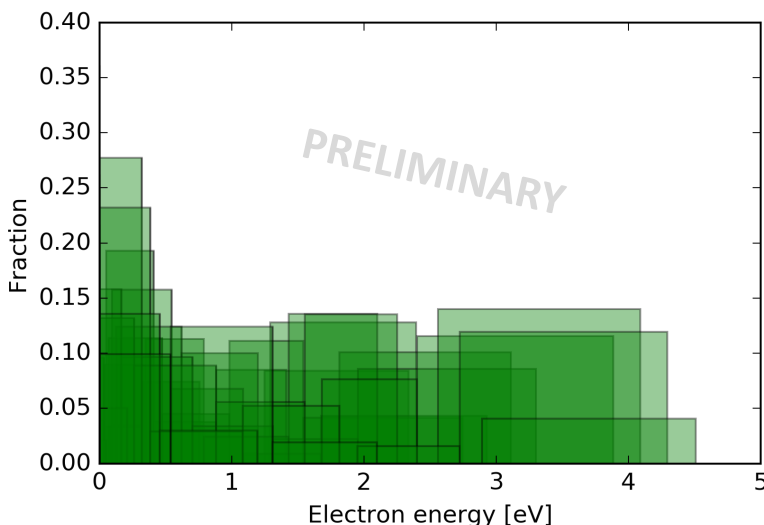


Figure 5.1.: The background electron energy spectrum in the main spectrometer, determined in dipole measurements. The energy spectrum ranges up to several eV, which is not expected in the current Rydberg background model [Pol18].

the electrons. The electron background energy distribution in the main spectrometer is of crucial importance for the investigation of a possible source.

The energy distribution is determined in so-called dipole measurements. The principle is to trap background electrons below a certain energy in the sensitive flux volume of the main spectrometer. Before the trapped electrons can scatter with residual gas and thereby break the storage conditions (see chapter 4.1), an electric dipole is applied. The stored electrons are removed from the flux tube, consequently the measured background rate at the detector is reduced. A variation of the trapping depth enables a scan of the energy distribution in an integrated way. The trap can be produced by two methods. One method is a magnetic trap, which traps electrons depending on their transverse energy relative to the magnetic field (see chapter 4.1). The depth of the trap is varied by the magnetic field setting and the retarding voltage. The other method is to trap electrons in a shallow Penning trap (see chapter 4.3). Electrons, with energies smaller than the depth of the Penning trap, are trapped in radial direction by the magnetic field and in axial direction by the electric field. Depending on the pitch angle, the Penning trap can also store electrons with larger energies than the trap depth. The depth of the trap is varied by a variation of the electric field strength. Figure 5.1 displays the preliminary results for the calculated differential energy distribution. The graph shows, that a part of the background energy distribution has starting energies greater than 1 eV. The background model of Rydberg atoms, which are ionised by black-body radiation, explains only energies $\mathcal{O}(10^2 \text{ meV})$ [Pol18]. Electrons with energies larger than 1 eV can be magnetically trapped in the main spectrometer, in contrast to electrons with less energy.

Background electrons are trapped in the main spectrometer if their polar emission angle θ relative to the magnetic field lines exceeds a certain angle θ_{max} at their point of creation (see chapter 4.1). θ_{max} can be described as a function of the retarding potential qU , the kinetic energy E_{kin} , the magnetic field strength at the point of creation $B(\vec{x})$ and the maximal magnetic field strength B_{max} :

$$\theta_{\text{max}} = \arcsin \left(\sqrt{\frac{q|U(\vec{x})|}{E_{\text{kin}}(\vec{x})} \cdot \frac{B(\vec{x})}{B_{\text{max}}}} \right) \quad [\text{Har15}]. \quad (5.2)$$

θ_{max} is calculated as a function of the retarding potential and the electron energy. $B(\vec{x})$ is set to 2.7 G^1 , which is a typical value for the analysing plane. The maximal applied magnetic field B_{max} is 4.2 T in the pinch magnet.

The upper graph of figure 5.2 shows the results of this calculation. The retarding potential is plotted on the y-axis from 18 keV to 19 keV. On the x-axis the electron energies from 0.1 eV to 3 keV are shown logarithmically. Background electrons which possess these energies are measured in the electron ROI at the detector. The plot shows, that θ_{max} is mainly dominated by the electron energy. Electrons smaller than 1.2 eV are not stored at all, independent of their polar emission angle, as this is the maximal energy resolution of the main spectrometer for the 2.7 G-setting. θ_{max} equals the maximal polar angle of 90° for this energy range. θ_{max} is decreasing for electron energies above 1.2 eV. The energy distribution of figure 5.1 shows, that a non-negligible part of the background electrons has energies above 1.2 eV. A small dependence on the retarding potential exists for these energies.

This relation is demonstrated by a profile plot of θ_{max} as function of the retarding potential for an electron energy at 1.5 eV (see lower graph of figure 5.2). θ_{max} increases linearly with the retarding potential from 61.5° at 18.0 keV to 64.5° at 19.0 keV. θ_{max} is small at low retarding potential, resulting in an increased amount of trapped electrons.

Normally one would expect, that the trapped background electrons go through a process of cooling-down (see chapter 4.1) and should leave the trap with a small temporal difference

¹1 G=10⁻⁴ T[Jil15]

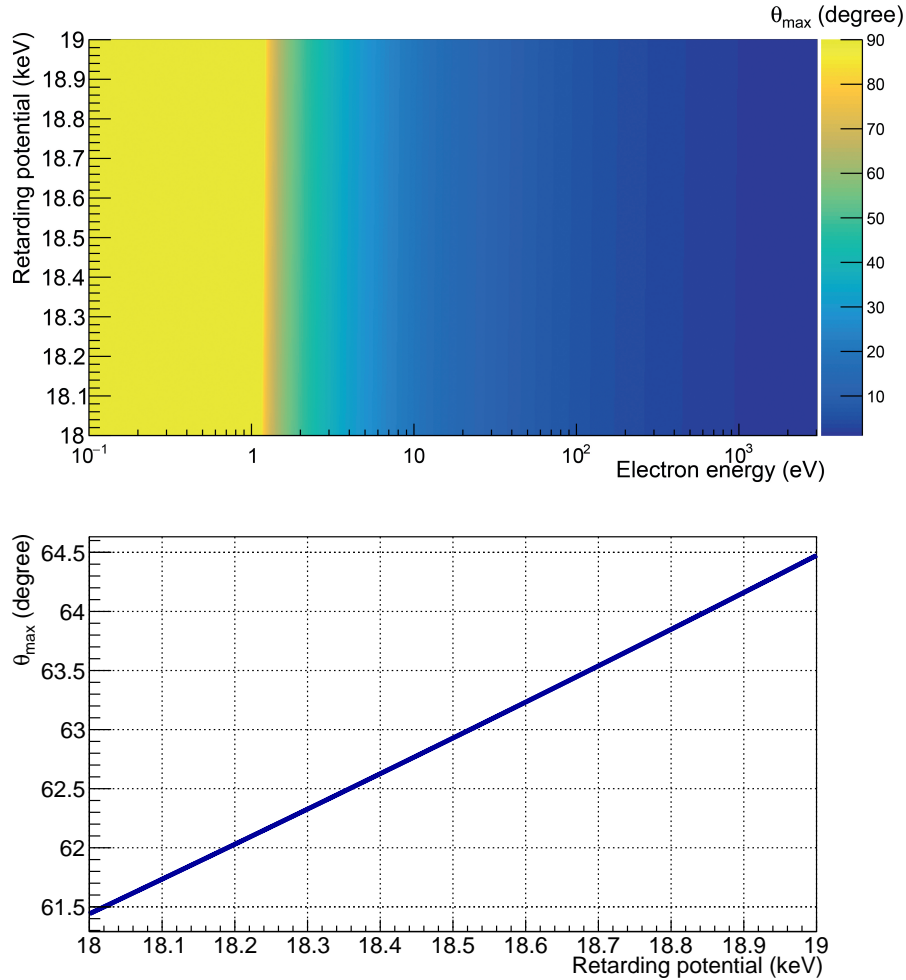


Figure 5.2.: θ_{\max} as function of kinetic energy and retarding potential (upper graph), dependence of θ_{\max} on the retarding potential for electron energies at 1.5 eV (lower graph). For the calculation of θ_{\max} the ratio of $B(\vec{x})/B_{\max}$ is set to a typical value of 6.4×10^{-5} in the analysing plane. It is displayed in the upper plot that the maximal polar angle is dominated by the kinetic energy of the electron (notice the logarithmic x-axis). However, also a small dependence on the retarding potential exists. This small dependence is shown in the lower graph, where θ_{\max} is plotted as a function of the retarding potential for a kinetic electron energy of 1.5 eV.

$\mathcal{O}(\min)$. For a measurement time at one potential on the scale of hours, the voltage dependence should be washed out. However, a mechanism which removes the stored electrons from the sensitive flux volume, would result in a reduction of the background rate. There are two possible mechanisms which could prevent the measurement of stored electrons at the detector:

1. A weak electrostatic dipole could drift stored electrons to the spectrometer vessel where they would disappear. Such an electrostatic dipole might be caused by a varying distance of the inner electrode system to the vessel. Simulations to this topic are ongoing. A stronger effect of a possible dipole on stored electrons would be expected at larger radii.
2. During the storage time, trapped electrons scatter with residual gas and change the polar emission angle, which allows them to break the storage condition. While the electrons are stored, they perform a slow drift around the magnetic main axis of the main spectrometer. During this magnetron motion, stored electrons can spend part

of their storage time outside the flux tube. In case the trapped electrons scatter with residual gas outside the flux tube, they might break the storage condition. However, as this process takes place outside the sensitive volume, the electrons are not guided to, but past the detector and are therefore not detected. Also in this mechanism, the rate reduction would mainly take place at the outer detector rings.

Nevertheless, more detailed investigations are required to explain a possible voltage dependence [MPHG17].

In case that the electrons of the ionised Rydberg atoms are emitted isotropically and that all stored electrons cannot reach the detector, a possible reduction of the rate can be calculated. A reduction of the rate of 2.7% is expected for an electron energy of 1.5 eV. Nevertheless, this is just a very rough estimate, more detailed simulations with the measured electron energy distribution are required and should be performed in future works.

5.3. Measurement of October 2017

The retarding potential was varied for a measurement time of 60 hours to determine the relation between the retarding potential and the background rate. The background rate was periodically measured at 18.0, 18.2, 18.4, 18.6, 18.8 and 19 keV for one hour each [Frä17f]. This measurement determined the background dependence over a relatively wide range of the retarding potential (10^3 eV) in comparison to the normal scanning range of neutrino mass measurements of maximal 65 eV. The retarding potential was chosen over such a wide range to get a “lever arm” for a more precise determination of the slope. If, on the one hand, the background rate would be measured only over a narrow retarding potential range, a possible background slope would be superimposed by statistical fluctuations. If on the other hand the retarding potential range is chosen too wide, the first-order approximation to describe the background with a first degree polynomial would lose its validity. Therefore a decision for a 1 keV retarding potential range was made.

There were collisions of the magnetic flux tube with the spectrometer walls in the measurement. The corresponding pixels of the detector (124-130, 136-142 and 147) are therefore dominated by secondary electron emission and consequently excluded for the analysis.

Figure 5.3 displays the results of the measurement. An increasing rate with retarding potential is shown, which is describable by a first degree polynomial with a reduced χ^2 of 0.7.

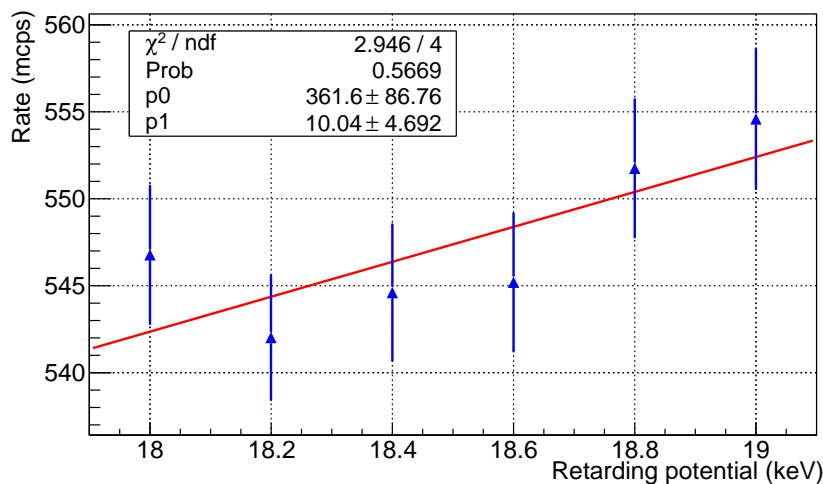


Figure 5.3.: Background rate versus retarding potential. A trend of increasing background rate with the retarding potential is shown and fitted with a first order polynomial. The fit results in a slope of $\delta = (10.04 \pm 4.69)$ mcps/keV.

The fit results in a statistically significant background slope of $\delta = (10.04 \pm 4.69)$ mcps/keV. A ring-wise analysis of the data indicates, that the rate increases uniformly with the retarding potential and not only in certain parts of the detector. If the rate would only increase towards the outer ring, this would point towards a relation with secondary electrons. However, since the rate increases uniformly over the whole detector, the varied retarding potential seems to affect all background electrons distributed in the volume of the spectrometer.

A decrease of the rate towards lower retarding potentials favours the source explained in chapter 5.2. A difference of the measured background rate between 18 keV and 19 keV of approximately 2.2% is in accordance with the estimate for trapped background electrons, which are eliminated from the sensitive flux volume.

5.4. Measurements of January 2018

Two additional measurements were performed in January 2018 to determine the background slope with higher precision [FB18]. In those measurements the magnetic field setting was chosen to be 6 G in the analysing plane, as this promises the highest KATRIN sensitivity [Beh17]. By changing the magnetic field setting in comparison to the October measurements, the storage condition for background electrons changes (see equation 5.2). Thus, it is expected that the value of the slope also changes. The difference of the storage condition $\Delta\theta_{\max} = \theta_{\max}(\text{January}) - \theta_{\max}(\text{October})$ is plotted in figure 5.4.

$\Delta\theta_{\max}$ is always greater than zero which means that θ_{\max} is larger in the January measurement than in the one from October. This results in less trapped electrons in the main spectrometer and consequently should result in a smaller slope. The difference of the magnetic field settings has large influence on electron energies between 2 eV and 3 eV with a difference in θ_{\max} of more than 45° .

5.4.1. Experimental Results

The first of the two January measurements was performed at the beginning of January 2018, for which the retarding potential was iteratively set to 18.0, 18.4, 18.8 and 19.2 keV. In comparison to the October measurement, the range of the retarding potential is wider to get a more precise determination of the slope. Additionally, there are less measurement points

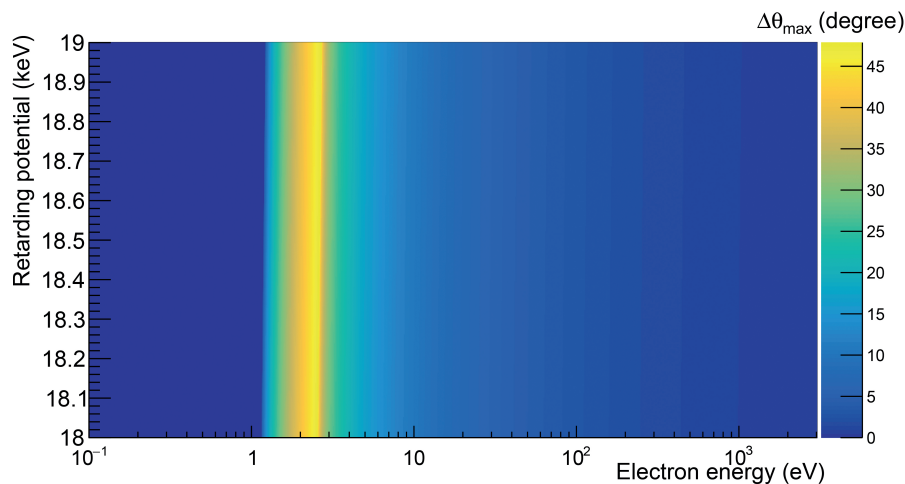


Figure 5.4.: Difference of the maximally allowed polar emission angle for background electrons between the October and January measurements. The difference is calculated to $\Delta\theta_{\max} = \theta_{\max}(\text{January}) - \theta_{\max}(\text{October})$. The January measurements used a 6 G and the October measurements a 2.7 G magnetic field setting.

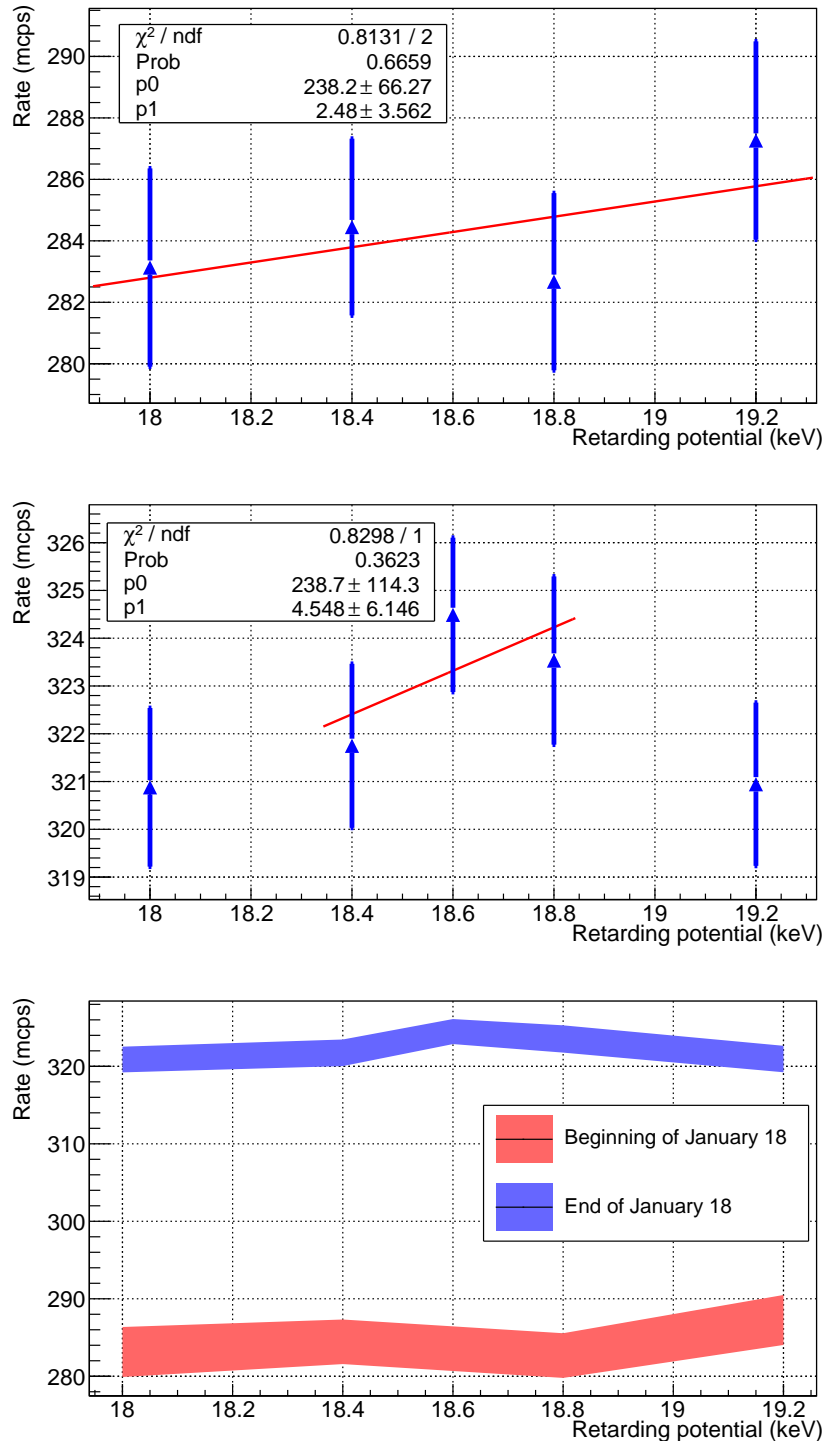


Figure 5.5.: Measurements of background dependence on the retarding potential, measured at beginning (upper graph) and end (middle graph) of January '18. The lower line shows both measurements in one graph for better comparison. Both measurements indicate a dependence of the measured rate (y-axis) versus the retarding potential (x-axis). The results of the measurement at the beginning of January can be described by a first degree polynomial. The measurement at the end of January is performed with the same magnetic setting. The overall shape of the rate versus the retarding potential as well as the total rate changes, which is not expected. The rate and the corresponding statistical uncertainty of both measurements are shown in the lower graph. For illustration, the four (red) and five (blue) data points and their uncertainties are interpolated. The discrepancy in the total rate between the two measurements cannot be explained by statistical fluctuations.

in January to increase the statistics at each point. In total, 40 h data were taken in the first January measurement. It was measured for two hours at each retarding potential before continuing to the next one. An increase of the rate with retarding potential was measured, which is describable by a first degree polynomial with slope $\delta = (2.48 \pm 3.56)$ mcps/keV (see upper graph of figure 5.5). The uncertainty on the measured slope decreases in comparison to the October measurement, this is due to the wider measurement range of the retarding potential. As expected, the slope itself decreases in comparison to the October measurement. Within its statistical uncertainty, it is compatible with zero. However, the measured rate at 18.8 keV is lower than the one at 18.4 keV. To further investigate this region, a measurement point at 18.6 keV was added and the measurement was repeated at the end of January with higher statistics.

At the end of January, the voltage dependence was measured over one week with the same magnetic field setting as in the measurement at the beginning of January. The middle plot of figure 5.5 presents the rate versus the retarding potential, which shows two inconsistencies compared to the previous measurement.

First, the overall shape of the dependence changes and cannot be described by a first degree polynomial anymore (68 % CL). A change of the voltage dependence is only expected by a change of the magnetic field, which did not occur. Nevertheless, the slope of the background rate versus the retarding potential needs to be quantified for the long-term measurement at the end of January. Therefore, only the rate at the three inner points at the retarding potentials of 18.4, 18.6 and 18.8 keV are fitted with a first degree polynomial. The resulting slope is (4.55 ± 6.15) mcps/keV.

The second inconsistency is, that the total underlying rate is elevated by at least 30 mcps (see lower graph of figure 5.5). This increase cannot be explained by statistical fluctuations. A sudden increase of the rate is also not expected, as the Rydberg model expects a time-independent background rate on the time-scales of several months. Additionally, in between the two measurements no artificial background source was installed in the spectrometer and detector section, which might cause a higher background rate.

Possible sources for the two inconsistencies are discussed in the following chapter.

5.4.2. Possible Explanations for Inconsistencies in the January Measurements

One reasonable explanation for the inconsistencies might be a fluctuation of the hardware parameters (also called slow-control parameters).

The different hardware parameters (e.g. magnetic field strength) are recorded over time. This enables a detailed investigation on parameter changes during a measurement. 17 slow-control parameters (see table 5.1), which are assumed to have an influence on the background rate, are examined in more detail to explain the inconsistencies in the January measurements. All examined slow-control parameters show a stability on the percent level or below during each measurement, indicating that the hardware parameters were constant. The required stability for each parameter, which is achieved during the measurements, is given in [KAT05].

Additionally, correlation analyses with the measured rate and the 17 slow-control parameters are performed to quantify the influence on the rate. Therefore, each measurement is split into smaller time ranges. For each time range, the mean value of the respective slow-control parameter and the mean value of the rate is calculated. A scatter-plot displays the results of all time ranges for one measurement for the respective slow-control parameter and the measured rate. The orientation for uncorrelated data points is mainly parallel to one of the axes of the scatter-plot. A deviating trend in the scatter-plot indicates a correlation. The correlation coefficient ρ quantifies a possible correlation. It ranges from -1 to +1. The correlation coefficient is $\rho = 0$ for uncorrelated variables. $\rho = 1$ is called positive correlated

Table 5.1.: Analysis of slow-control parameters during the January measurements. The first two columns describe the used slow-control parameters. The result of the correlation analysis of the respective parameter with the measured rate is printed in the fourth and fifth column. The relative mean deviation of the slow-control parameters between the two measurements is calculated in the last column. The corresponding KATRIN numbers of the slow-control parameters are given in chapter B.

Parameter	Position Sensor	ρ Beginning of January	ρ End of January	Rel. Deviation Slow-Control (%)
Magnetic field analysing plane	Mid-Ring 9	-0.27	-0.19	0.009
	Mid-Ring 23	0.40	0.26	0.025
	Mid-Ring 30	0.27	0.12	0.002
MS pressure	Extractor ion gauge	-0.06	0.09	8.425
FPD temperature	Carousel	0.12	-0.09	2.808
Baffle 1 temperature	Top	-0.09	-0.08	1.361
	Bottom	-0.28	-0.05	0.004
	Centre	0.37	-0.30	0.142
	Inlet	0.12	-0.30	0.120
Baffle 2 temperature	Top	-0.01	-0.07	0.240
	Bottom	-0.02	-0.05	0.062
	Centre	-0.11	-0.12	0.107
	Inlet	0.00	0.00	0.428
Baffle 3 temperature	Top	0.02	0.01	0.297
	Bottom	0.05	-0.13	0.005
	Centre	0.04	-0.14	0.012
	Inlet	0.02	-0.10	0.011

whereas $\rho = -1$ describes a negative correlation [Wal15].

The resulting correlation coefficients of the correlation analyses with the measured rate and the 17 slow-control parameters are shown in the third and fourth column in table 5.1. A strong correlation is not present, as the absolute correlation factor $|\rho|$ is always smaller than 0.4 in both measurements. To explain the inconsistencies between the two January measurements by hardware effects, two conditions have to be fulfilled. First, a non-negligible correlation between the hardware parameter and the background rate is required. Second, a deviation of the measured values of this parameter between the two measurements must be given (see table 5.1 last column). The relative deviations between the two measurements are all below the percent level, except for the main spectrometer pressure, the FPD carousel temperature and the baffle 1 temperature at the top. However, all of these three parameters have a nearly vanishing correlation with the measured rate. To summarise, there are no signs of hardware fluctuations in the KATRIN set-up which could be responsible for the elevated background rate or a changed behaviour of the rate versus retarding potential.

Possible side-effects of ramping through several retarding potentials could elevate the total background rate. To investigate this, it is necessary to take a look at the complete SDS-IIIc measurement phase. Before the first January voltage dependence measurement, a long-term background measurement was performed (see chapter 6). In this period the background was measured over 14 consecutive days at a constant retarding potential of 18.6 keV. The mean rate in the electron ROI is (287.7 ± 0.4) mcps, which is in accordance with the voltage dependence measurement at the beginning of January. After the second voltage dependence

measurement at the end of January, an additional measurement was performed to confirm the elevated rate. In there the same settings as for the long-term measurement were used and the elevated rate is confirmed [FHB18]. Hence, side-effects of ramping through different retarding potentials are excluded as source for the elevated rate. Further investigations to this topic are ongoing.

5.5. Methods to Treat the Voltage Dependence and the Influence on the Sensitivity

The influence of a possible voltage dependence of the background rate on the KATRIN sensitivity needs to be quantified. Therefore, three different ways to handle the impact of the vessel potential on the background rate are presented in the following. The first method is to neglect the background dependence in the background model, the second one is to include the dependence with a fixed value. Finally, a third method is presented which treats the background slope δ as a free fit parameter. The methods are introduced by the example of the measured values of the October '17 measurement. Afterwards the respective result for the measured values of the January '18 measurement is stated.

The sensitivity studies in the following are performed with the tool `KaFit` of the KATRIN software `KASPER`. The thesis of M. Kleesiek states more details about `KASPER` and `KaFit` [Kle14].

5.5.1. Neglecting Voltage Dependence

The design report states, that a slope of 2.5 mcps/keV results in a systematic shift on the squared neutrino mass of $\Delta m_\nu^2 \approx 6 \times 10^{-3} \text{ eV}^2$. This result is based on a background rate of 10 mcps at the endpoint of tritium. On the one hand the measured value of the slope in October is four times larger than the critical one from the design report. On the other hand the measured (545 ± 4) mcps background rate at the endpoint of tritium is many times higher than in the design report. Therefore one could assume, that the elevated background rate absorbs the measured slope to a certain level.

A data set with three full-beam years is simulated with a tritium spectrum of vanishing neutrino mass and a certain voltage dependent background. The model, which is fitted

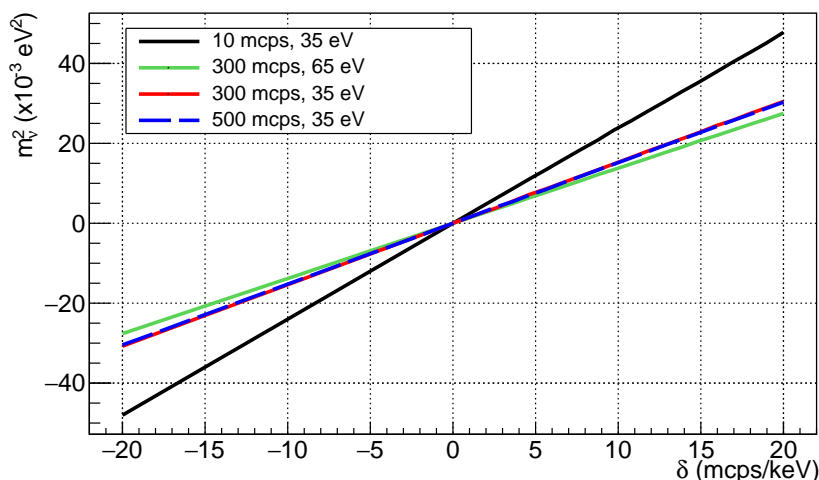


Figure 5.6.: The estimated squared neutrino mass, if the data contains a voltage dependent background, which is not considered in the background model. The shift on the squared neutrino mass is calculated for several background rates (10, 300 and 500 mcps). Additionally, the influence of the run-time schedule is shown for a background rate of 300 mcps.

Table 5.2.: Fit results of the squared neutrino mass versus the background slope δ for different background rates. The calculated squared neutrino mass can be described by $m_{\nu^2}(\delta) = a \cdot \delta$, if the data contains a voltage dependence which is not considered in the model.

Background Rate (mcps)	Scanning Range (eV)	a ($\times 10^{-3} \text{eV}^2 \cdot \text{keV}/\text{mcps}$)
10	35	(2.391 ± 0.001)
300	35	(1.5523 ± 0.0007)
300	65	(1.3954 ± 0.0004)
500	35	(1.5496 ± 0.0005)

to the data, assumes a constant background independent of the retarding potential. The fitted squared neutrino mass can be interpreted as the systematic shift on it. Figure 5.6 summarises the results of several sensitivity studies, in case the model does not consider a voltage dependent background. The calculated squared neutrino mass is plotted as a function of the background slope for three different background rates. This graph reveals three important characteristics.

First of all, the calculated squared neutrino mass increases linearly with the background slope. The estimated squared neutrino mass in dependence of the underlying background slope can be described for all simulated scenarios with $m_{\nu^2}(\delta) = a \cdot \delta$. Table 5.2 states the fitted values of a for the scenarios.

Second, the size of the shift decreases with increasing background rate. This behaviour is expected. The statistical uncertainty increases at each retarding potential with increasing background rate. Consequently, the ratio of the slope over the statistical uncertainty decreases towards higher rates, resulting in less influence on the sensitivity. The increased background rate therefore partially absorbs the measured slope.

Third, the choice of the run-time schedule has a significant influence on the shift of the squared neutrino mass. The comparison of the two sensitivity studies for a background rate of 300 mcps shows this effect. The estimated shift on the squared neutrino mass is smaller for a run-time schedule which uses 65 eV as scanning range than one, which uses 35 eV. The source for this is also the statistical uncertainty. The run-time schedule with a scanning range of 65 eV measures at more retarding potentials than the one of 35 eV. Hence, the statistical uncertainty of the determined rate is larger at each retarding potential in the first run-time schedule. The ratio slope over uncertainty decreases in comparison to the 35 eV schedule, which results in a smaller influence of the slope on the squared neutrino mass. The sensitivity studies in the following based on the data of the January measurements use the 65 eV run-time schedule due to two reasons. First, the influence of the slope on the sensitivity is smaller compared to the 35 eV schedule, therefore this is a best case approximation. Second, the 65 eV scanning range promises the best statistical uncertainty on the neutrino mass in the latest sensitivity studies [Beh17].

The influence of the experimental results on the squared neutrino mass are calculated in the following. The total rate at the endpoint of tritium amounts to 545 mcps in the October measurement. The slope is determined to 10.04 mcps/keV. The resulting shift on the squared neutrino mass of $15.4 \times 10^{-3} \text{eV}^2$ is nearly as large as the complete systematic error budget of $17.0 \times 10^{-3} \text{eV}^2$. Neglecting the impact of the retarding potential on the background rate seems therefore to be no option.

A slope of $(4.55 \pm 6.15) \text{mcps}/\text{keV}$ is determined in the data of the long-term January measurement of the background rate dependence on the applied retarding potential. The rate at the endpoint of tritium is approximately 324 mcps. Neglecting the background slope in the model would lead to a systematic shift on the squared neutrino mass of $6.3 \times 10^{-3} \text{eV}^2$ for these measured values. This is at the allowed limit for a single systematic effect in

the systematic error budget [KAT05]. Nevertheless, the slope is not measured precisely. Therefore, the true value of the slope might be higher and would exceed the limit for one systematic effect.

5.5.2. Including Voltage Dependence as Fixed Value

The second method to treat the background dependence includes the slope with a fixed value δ_0 in the model. However, the exact value of the slope is not known. Only the measured value and the corresponding confidence interval σ_δ are set. The experimental results of the October measurement state $\delta_0 = 10.04$ mcps/keV and $\sigma_\delta = \pm 4.69$ mcps/keV. An ensemble test is performed to demonstrate the influence of the uncertainty on the slope. Thereby 10^3 data sets are simulated, each with a different slope. The values for the slope are randomly generated, following a Gaussian distribution with mean 10.04 mcps/keV and width 4.69 mcps/keV. The model is fitted to each data set and the shift on the squared neutrino mass is calculated. The shifts of all analyses are plotted in figure 5.7 as histogram. The resulting distribution follows a Gaussian distribution with mean $(0.23 \pm 0.27) \times 10^{-3} \text{ eV}^2$ and width $(7.38 \pm 0.27) \times 10^{-3} \text{ eV}^2$. Hence, including the voltage dependence as a fixed value in the model leads to no systematic shift, if the true value equals the fixed one of the model. However, the unawareness of the true value results in possible shifts on the squared neutrino mass of $7.4 \times 10^{-3} \text{ eV}^2$ (68 % CL). This method therefore exceeds the limit of $6 \times 10^{-3} \text{ eV}^2$ for one systematic effect.

In case that the background dependence follows exactly a first degree polynomial, it is calculated how long the background slope has to be measured to meet the requirements of the design report. Therefore, the possible shifts on the squared neutrino mass need to be limited to smaller than $1.2 \times 10^{-3} \text{ eV}^2$ (68 % CL). For Poisson distributed rates the statistical uncertainty scales proportional to $1/\sqrt{t_{\text{meas}}}$. The extrapolation of the results from the fit in figure 5.3 yield a necessary measurement time of the background slope of approximately 90 days.

In the latter January measurement, the slope is determined to 4.55 mcps/keV with an uncertainty of 6.15 mcps/keV. The ensemble test with these values result in possible shifts

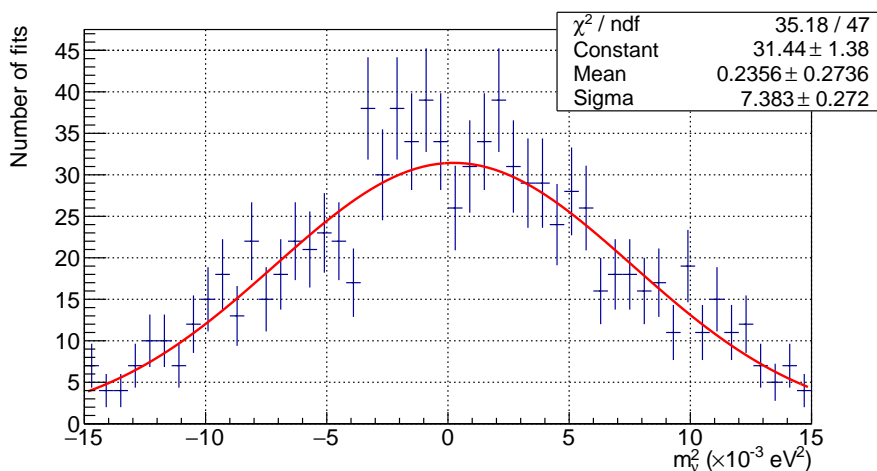


Figure 5.7.: Shift on the squared neutrino mass for 10^3 data sets with different background slopes and a fixed slope in the model. The slopes of the data sets are generated randomly following a Gaussian function with mean 10.04 mcps/keV and width 4.69 mcps/keV. The resulting distribution of the systematic shift on the squared neutrino mass also follows a Gaussian function with mean $(0.23 \pm 0.27) \times 10^{-3} \text{ eV}^2$ and width $(7.38 \pm 0.27) \times 10^{-3} \text{ eV}^2$.

on the squared neutrino mass of $8.4 \times 10^{-3} \text{ eV}^2$ (68 % CL). Also for these values, the allowed limit for one systematic effect is exceeded.

Consequently, including the slope with a fixed value leads to several challenges. First, the slope needs to be determined with higher precision, which results in a significantly increased measurement time. Second, the slope depends on the used magnetic field setting, hence it has to be known precisely for each magnetic field. Third, there are not yet understood effects, which influence the background dependence on the retarding potential even within the same magnetic field setting (see chapter 5.4).

5.5.3. Treating Voltage Dependence as Free Fit Parameter

The standard KATRIN likelihood contains four free fit parameters, namely the squared neutrino mass (m_ν^2), the endpoint of tritium (E_0) and the amplitude of signal (R_s) and background electrons (R_b) (see chapter 2.3.3). For this section the likelihood is extended by a fifth parameter, the background slope (δ). The squared neutrino mass is determined in a four parameters fit for a background rate of 545 mcps (similar to the October '17 measurement) to:

$$m_\nu^2 = (0.0 \pm 57.5 \text{ (stat)} \pm 17.0 \text{ (syst)}) \times 10^{-3} \text{ eV}^2.$$

The estimated statistical and systematic errors result in a sensitivity on the neutrino mass of 314 meV (90 % CL, see chapter 2.3.4). In the five parameters fit, the background slope is set to 10 mcps/keV. The fit estimates the squared neutrino mass to

$$m_\nu^2 = (0.0 \pm 109.6 \text{ (stat)} \pm 17.0 \text{ (syst)}) \times 10^{-3} \text{ eV}^2.$$

The neutrino mass and the background slope are correctly fitted, however the statistical uncertainty nearly doubles. This worsens the sensitivity on the neutrino mass to 427 meV. A closer look on the fit procedure of the five parameters fit is necessary, to explain the large increase of the statistical error.

The background slope can only be fitted with a large statistical uncertainty in the five parameters fit: $\delta = (10.1 \pm 69.7) \text{ mcps/keV}$. The slope is correlated with the parameter of interest, the squared neutrino mass. Therefore, the uncertainty of the slope propagates on the uncertainty of the squared neutrino mass. The covariance of the two parameters $C(x, y)$ is the weight of the propagation. The correlation coefficient is due to its normalisation a good indicator for the strength of the covariance. The correlation coefficient of two variables x and y is defined as

$$\rho = \frac{C(x, y)}{\sigma(x)\sigma(y)},$$

which ranges from -1 to +1. $|\rho| = 1$ indicates a strong correlation, whereas uncorrelated variables have $\rho = 0$ [Wal15].

The upper graph of figure 5.8 displays the correlation matrix of the five parameters for the normal measurement time distribution. The upper right side of the matrix shows the correlation between the squared neutrino mass and the slope. $\rho(m_\nu^2, \delta) = -0.89$ describes a strong negative correlation. The background slope and the endpoint of tritium have the strongest correlation with the squared neutrino mass. Consequently, the large uncertainty of the slope propagates on the squared neutrino mass with a big weight. The statistical uncertainty on the squared neutrino mass increases from $57.5 \times 10^{-3} \text{ eV}^2$ to $109.6 \times 10^{-3} \text{ eV}^2$.

A more precise fit of the background slope is required, to minimise the statistical uncertainty of the squared neutrino mass in the five parameters fit. The measurement principle of

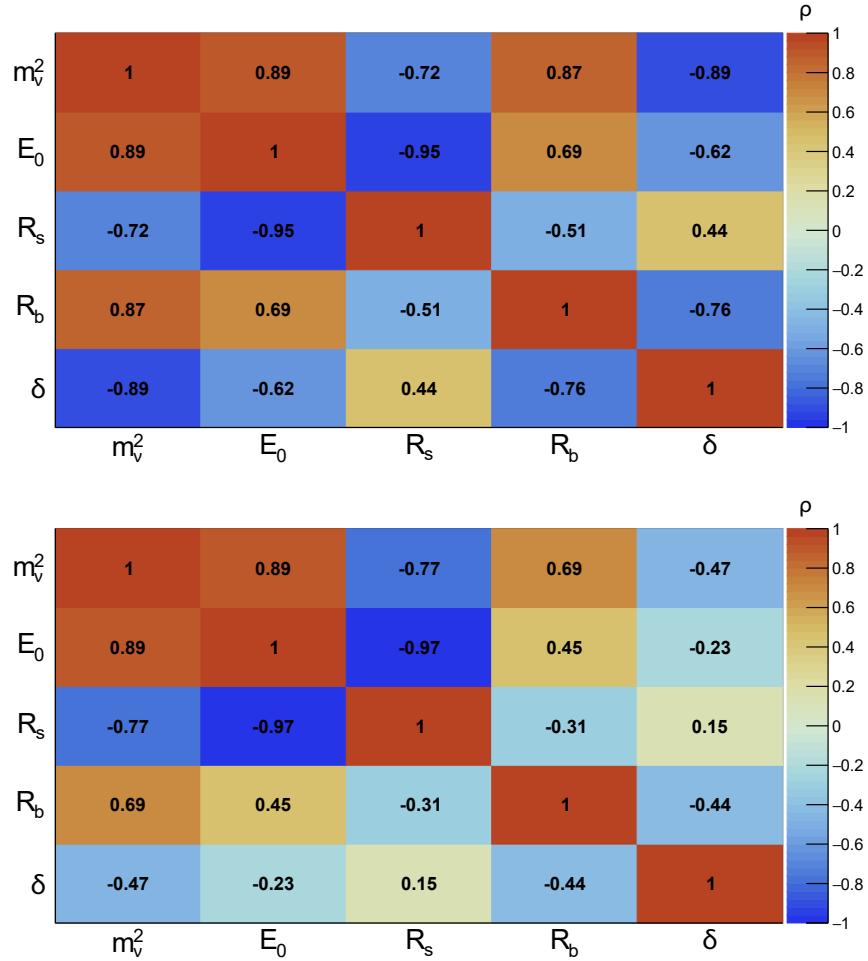


Figure 5.8.: Correlation matrix of the five parameters fit for the normal (upper graph) and adapted run-time schedule (lower graph). The background slope and the endpoint of tritium have the strongest correlation with the squared neutrino mass, if the normal run-time schedule is used. The correlation of the slope with the squared neutrino mass decreases significantly by using the adapted run-time schedule.

chapter 5.3 and 5.4 shows, that a wider scanning range of the retarding potential increases the precision on the slope. Consequently, the measurement time distribution needs to be adapted to achieve a smaller uncertainty on the squared neutrino mass.

The measurement time distribution, which is optimised for a background rate of 500 mcps and a four parameters fit, is plotted in the upper graph of figure 5.9. This run-time schedule varies the retarding voltage from 30 eV below to 5 eV above the endpoint of tritium. This small scanning range enables only an imprecise determination of the slope and results thus in a large statistical uncertainty.

Widening the scanning range enables a more precise determination of the slope. Two further measurement points are set for demonstration purposes in the adapted measurement time distribution (see lower graph of figure 5.9). One is set at 20 eV above the endpoint, the other at 50 eV above, each with a measurement time of approximately 10 days of the in total 3 years data taking phase. The background dependence is fitted to $\delta = (10.0 \pm 14.0)$ mcps/keV for the adapted run-time schedule.

Widening the scanning range also influences the covariance of the squared neutrino mass and the background slope. By adding measurement points above the tritium spectrum into account, the slope can be determined without taking the tritium spectrum into account. This leads to a reduced correlation factor of $\rho(m_\nu^2, \delta) = -0.47$ (see lower graph of figure 5.8).

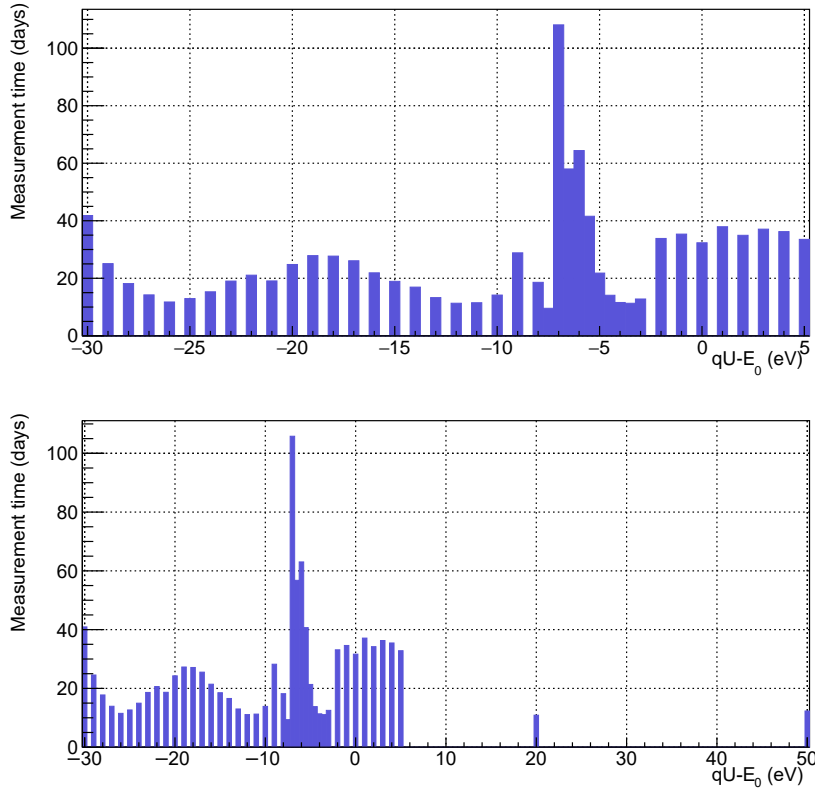


Figure 5.9.: Normal measurement time distribution for a four parameters fit (upper graph) and an adapted one for the five parameters fit (lower graph). On the y-axis the total measurement time at each retarding potential is plotted. The x-axis shows the distance to the endpoint of tritium. The upper run-time schedule is optimised for a background rate of 500 mcps and a four parameters fit. The lower schedule is adapted for a five parameters fit by adding two measurement points at 20 and 50 eV above the endpoint with approximately 10 days measurement time each.

Consequently, the adaption of the run-time schedule reduces the statistical uncertainty on the squared neutrino mass in the five parameters fit to $64.5 \times 10^{-3} \text{ eV}^2$. This improves the sensitivity from 425 meV to 331 meV (90 % CL).

The magnetic field setting of the January measurements results in a sensitivity on the neutrino mass of 252 meV (90 % CL) for a constant background rate. The statistical uncertainty on the squared neutrino mass in this four parameters fit amounts to $34.7 \times 10^{-3} \text{ eV}^2$. The statistical uncertainty doubles by extending the KATRIN likelihood for the background slope as fifth free fit parameter. Similar to above, the increase of the statistical uncertainty is minimised by an adapted run-time schedule. The uncertainty decreases to $38.9 \times 10^{-3} \text{ eV}^2$ by adding two additional measurement points above the endpoint of tritium.

It has to be mentioned, that the adaption of the run-time schedule for both measurements is just for demonstration purposes. The additional measurement points were set by hand, to show the improvement on the statistical uncertainty. Consequently, the sensitivity of the five parameters fit can be further improved by calculating an optimised run-time schedule with KaFit.

5.5.4. Comparison of Sensitivity

Table 5.3 presents the results of the different sensitivity studies performed in this chapter. The upper half of the table shows, that the systematic uncertainty budget has only little influence on the sensitivity for the measured values in October '17. The comparison of a

Table 5.3.: Comparison of sensitivity for the three different methods to treat the slope. The first two columns display the method to treat the background slope and the underlying data of the study. The case of constant background is stated for comparison. The third and fourth columns show the resulting systematic and statistical uncertainty. The last column calculates the sensitivity of the respective method with a 90% CL.

Measurement	Method	$\sigma_{\text{syst}} (\times 10^{-3} \text{ eV}^2)$	$\sigma_{\text{stat}} (\times 10^{-3} \text{ eV}^2)$	Sensitivity (meV)
October '17	Const. bkg.	17.0	57.5	314
	Neglect slope	22.9	57.5	319
	Fixed slope	18.5	57.5	315
	Fitting slope	17.0	64.5	331
January '18	Const. bkg.	17.0	34.7	252
	Neglect slope	18.1	34.7	254
	Fixed slope	19.0	34.7	255
	Fitting slope	17.0	38.9	264

constant background rate with the method to neglect the slope shows this. In the first one, the systematic uncertainty budget is $17 \times 10^{-3} \text{ eV}^2$. The systematic uncertainty of the method to neglect the slope is calculated to $22.9 \times 10^{-3} \text{ eV}^2$ (see chapter 2.3.4). The increase of the systematic error budget of 34.7% worsens the sensitivity on the neutrino mass by 1.5%. The statistical uncertainty dominates the sensitivity due to the high total background rate of approximately 500 mcps. Hence, the fit of the slope has the worst sensitivity of the presented methods, as it increases further the statistical uncertainty. Consequently, if the neutrino mass measurements would be performed with a magnetic field, which features such high background rates, neglecting the slope or setting a fixed value in the model would be the best options.

However, the neutrino mass measurements shall be performed with a magnetic field setting similar to the one of the January '18 measurements. Therefore, the results shown in the lower half of table 5.3 are of crucial importance. The used magnetic field setting results in a background rate of approximately 300 mcps. Consequently, the statistical uncertainty decreases in comparison to the October measurement to $34.7 \times 10^{-3} \text{ eV}^2$. However, the statistical uncertainty is significantly large than the systematic one. The overall sensitivity is still mainly dominated by the statistical uncertainty. Consequently, fitting the slope leads to the worst sensitivity for the January measurements. Nevertheless, it has to be taken into account that the method to fit the slope can still be improved. If the optimised run-time schedule enables a statistical uncertainty of lower than $35.5 \times 10^{-3} \text{ eV}^2$, the fit of the background slope would result in a sensitivity better than 254 meV.

5.6. Conclusions

A significant dependence of the background rate on the retarding potential is measured in October '17. A possible explanation for this dependence is a different storage condition of background electrons at different retarding potentials, together with a mechanism which removes trapped electrons. The explanation predicts, that the dependence decreases with increasing magnetic field strength in the analysing plane. The January measurements confirm this prediction, the background slope is determined to be in accordance with zero within the statistical uncertainty.

Two inconsistencies occur by comparing the two January measurements to determine the background dependence on the retarding potential. First, the constant underlying background rate is elevated by approximately 30 mcps, which cannot be explained by statistical fluctuations. Second, the behaviour of the background rate versus the retarding

potential changes. It is assumed that these two effects have the same source. However, this source remains unresolved and further investigations are required in future works.

Three different methods to treat the background slope are presented: neglecting the slope, including it in the model with a fixed value and treating it as a free fit parameter. The first two methods significantly increase the systematic uncertainty budget. However, this only slightly influences the KATRIN sensitivity on the neutrino mass. The statistical uncertainty dominates the sensitivity due to the elevated background rate in comparison to the design report. Treating the background slope as a free fit parameter increases the statistical uncertainty and has therefore a larger influence on the sensitivity. The increase of the statistical uncertainty can be minimised by an adaption of the run-time schedule. An optimised run-time schedule for the five parameters fit needs to be calculated for further discussions. The five parameters fit is only an appropriate solution for a constant slope, if an adapted run-time schedule enables a statistical uncertainty of lower than $35.5 \times 10^{-3} \text{ eV}^2$.

Nevertheless, the measured elevation of the rate in January, related with a change of the background rate dependence on the retarding potential, leads to problems. It is difficult to compare sensitivity studies based on different measurements, if the background rate or background behaviour can change spontaneously. This eliminates a reliable estimate of the systematic uncertainty budget of the methods to neglect the slope and to include it with a fixed value. Therefore, applying the slope as a free fit parameter seems to be the only reliable method. However, it is of crucial importance to find the source for the elevated background to enable the possibility of applying the two others methods and to further control the background related systematics. It is recommended to use the five parameters fit due to its reliability until the source for the elevated background is found. If a sudden increase of the background rate, related with a change of the voltage dependence, can be excluded in the future, it is recommended to treat the background slope as a systematic effect.

6. Investigation of SDS-IIIc Long-Term Background Measurement

A long-term background measurement of the spectrometer and detector section was performed during the Christmas break 2017 for 14 consecutive days. The aim of the SDS-IIIc long-term measurement is the investigation of the background rate in an electric and magnetic field setting, which is planned to be applied in the neutrino mass measurements. A detailed characterisation of properties of the background, like pixel distribution or stability of the rate, is paramount for the KATRIN experiment. Additionally, the measurement enables a test of the stability of several hardware parameters for the complete working SDS over a time range of two weeks.

The following chapter 6.1 investigates the background rate in more detail in comparison to former measurements. In addition, the statistical behaviour of the rate as well as its time development is investigated. Chapter 6.2 tries to determine possible correlations of hardware parameters with the measured electron rate. The energy spectrum of the long-term measurement is characterised in chapter 6.3. The last chapter 6.4 examines the measured pixel distribution in the ion as well as in the electron ROI in more detail.

6.1. Background Rate in the Electron ROI

The magnetic field strength in the analysing plane of the main spectrometer was set to approximately 6 G for the SDS-IIIc long-term background measurement. This is higher than typical values of former long-term spectrometer background measurements (2.7-3.8 G). The total background rate decreases by an increase of the magnetic field strength. Thereby the energy resolution of the main spectrometer worsens from the nominal 0.93 eV to 2.8 eV. The magnetic field configuration of the SDS-IIIc long-term measurement provides the highest KATRIN sensitivity for the current background rate [Beh17]. The pre-spectrometer was operated at a retarding potential of 18.3 keV, the main spectrometer at 18.6 keV. The spectrometer vessel was set to -18.4 kV, the inner electrode system was at 200 V more negative potential [Frä17e].

6.1.1. Comparison with Former Background Measurements

The long-term background measurement of SDS-IIIc is compared with two previous SDS background measurements. All measurements were performed after baking the main spectrometer.

The oldest measurement was performed in course of the SDS-IIb measurement phase in 2015. Six pixels were not available for analysis due to a faulty preamp card in the detector read-out electronics. An interpolation over the two neighbouring pixels allows an estimate of the rate in the faulty pixels. At that time only measurements of the main spectrometer background were possible, which were performed with a 3.8 G magnetic field setting in the

analysing plane [Tro15].

The second presented measurement was taken in mid 2017 in the course of the SDS-IIIb measurement. At that point of time, the main spectrometer was baked, the pre-spectrometer getter pump was not yet activated to full capacity. The pre-spectrometer was set to ground potential for the measurement time of approximately 100 h [RTBF17].

Several calculations are necessary to compare the three measurements with the different magnetic field settings.

First of all the detector background needs to be subtracted from the measured data, as the focus of this analysis lies on the spectrometer background. The intrinsic detector is independent of the magnetic field setting and was determined in the SDS-II [HF15] as well as in the SDS-III [Frä17b] measurement phases.

As stated in chapter 4.6, it is expected that the spectrometer background rate scales with the sensitive volume, which is defined by the magnetic field setting. However, the measured background does not scale exactly with the flux tube volume, therefore the rate is calculated for each detector ring. Afterwards, the ring-wise rate is scaled with the observed flux volume of the respective detector ring. The software *Kassiopeia* [BBC⁺11] determines the flux tube and enables an estimate of the sensitive flux volume. The scaled ring-wise rate is projected to the analysing plane. This results in a better comparison of the background rate of different measurements, as higher magnetic field settings observe only smaller parts of the background rate distribution in the analysing plane.

Figure 6.1 displays the results, after performing the described steps. The graph presents significant differences between the measured background rates. The background of the SDS-IIb phase (black data points) shows the lowest volume-normalised rate. This is reasonable as the data contains only the background of the main spectrometer. An increase of the normalised rate to larger radii is visible.

The data of SDS-IIIb with unbaked and grounded pre-spectrometer is plotted in blue. The upstream magnet of the pre-spectrometer (PS1) was switched off for this measurement, therefore the magnetic field minima was smaller than normally in the pre-spectrometer. This small minima results in a strong magnetic mirror, by which the high-energy electrons are reflected. Hence, only low-energy background electrons can leave the pre-spectrometer. However, they cannot enter the main spectrometer due to the applied retarding potential of 18.6 keV. The pre-spectrometer should therefore only have little influence on the total rate

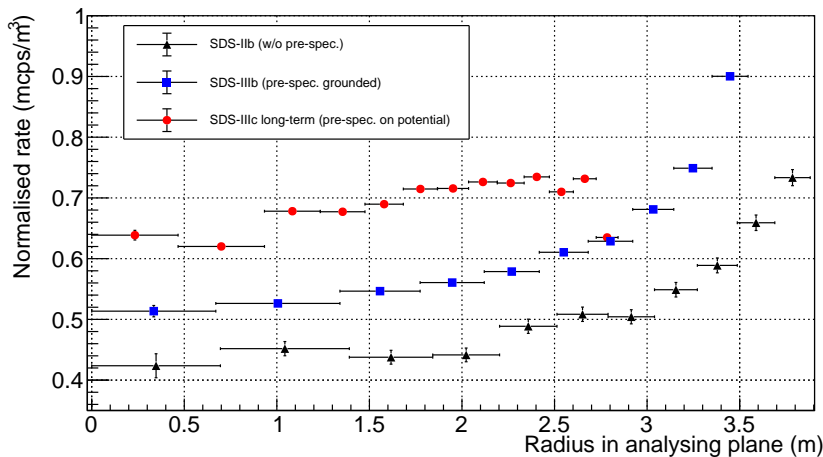


Figure 6.1.: Ring-wise rate normalised with the sensitive flux tube volume plotted versus the radius in the analysing plane. With increasing radius the normalised rate is also increasing. A significant difference between the SDS-IIIc background measurement and former measurements is shown.

as long as it is grounded and as long as the PS1 is switched off. Nevertheless, a significant difference between the background rate of SDS-IIb and SDS-IIIb exists, which increases towards larger radii.

The storage conditions for background electrons near the analysing plane are in both measurements nearly the same. The maximum applied magnetic field along the beamline was 6.0 T, the minima 3.8 G in the SDS-IIb measurements. During the SDS-IIIb measurement phase, the strongest magnetic field amounted to 4.2 T and the minima in the analysing plane was 2.7 G. The storage condition only depends on the ratio (see equation 5.2) which is the same in both measurements. Therefore, the magnetic field setting can be excluded as the source for this difference.

During the SDS-IIIa measurement phase the spectrometer was contaminated with ^{212}Pb to test the Rydberg background model. Therefore a ^{228}Th source was connected to the main spectrometer. ^{228}Th decays into ^{222}Rn , which contaminates the inner spectrometer surfaces and decays in ^{212}Pb . ^{212}Pb is the isotope with the longest half-life in the decay chain of ^{228}Th with $t_{1/2} = 10.64\text{ h}$ [Bro05]. However, there might still be residual ^{228}Th activity, which elevates the background rate [FBH⁺16]. Consequently, the SDS-IIb measurement needs to be reproduced with the same magnetic field setting and valve between pre- and main spectrometer closed. This measurement enables the test, whether long-term increases to the background rate were induced by the ^{228}Th source.

A further possible source for the elevated background rate is the absence of a baffle system in the pre-spectrometer. This allows ^{219}Rn from the NEG material to enter the sensitive flux volume. Since ^{219}Rn is electrically neutral, it is not influenced by the magnetic mirror nor the retarding potential. Hence, it can enter the sensitive volume of the main spectrometer. A decay of ^{219}Rn in the main spectrometer yields additional background (see chapter 4.4). Measurements are ongoing to quantify the influence of radon decays from the pre-spectrometer [Frä18c].

The background rate of the SDS-IIIc long-term background measurement is plotted in red in figure 6.1. The inner electrode offset was set to 100 V in the SDS-IIb and SDS-IIIb measurements. The offset amounted to 200 V in the SDS-IIIc long-term background measurement, resulting in a larger electrostatic shielding. Therefore, it is expected that the background rate is reduced in contrast to the other two measurements. However, the former background measurements show less volume-normalised rate for the flux tube of the SDS-IIIc measurement. The relative difference in the rate between the SDS-IIIb and SDS-IIIc measurement is approximately 23%. There are two major differences in the experimental set-up of the spectrometer and detector section, which might cause the elevated rate: the pre-spectrometer was on potential in SDS-IIIc and a different magnetic field setting was used.

In case the pre-spectrometer is set on potential, a Penning trap is formed. This might result in a Penning discharge and a clearly elevated rate as described in chapter 4.3. Furthermore, the storage conditions for background electrons in the pre-spectrometer change. More electrons with energies lower than the applied retarding potential of the pre-spectrometer can leave it. This might yield additional background. A subsequent of the long-term measurement enables a quantification of this effect. The pre-spectrometer was grounded in this measurement and the PS1 magnet was switched off [Frä17e]. The rate in the electron ROI is measured to $(287.7 \pm 0.4)\text{ mcps}$ with applied retarding potential in the pre-spectrometer. If the pre-spectrometer is grounded, the background rate corresponds to $(283 \pm 1)\text{ mcps}$. A statistically significant difference exists. Nevertheless, the reduction is on the percent level and does not explain the large difference between the blue and red data points.

The magnetic field settings strongly differ from each other between the SDS-IIIb and SDS-IIIc measurements. Both settings had as maximal magnetic field strength along the beamline 4.2 T in the pinch magnet. The magnetic field strength in the analysing plane

of the SDS-IIIb measurement was 2.7 G, which corresponds to an energy resolution of 1.2 eV. Thus, all electrons with larger transverse energies than 1.2 eV are stored. In the SDS-IIIc long-term measurement, a balance was found between the total rate and the energy resolution to ensure best sensitivity on the neutrino mass. The magnetic field strength was set to 6 G in the analysing plane, corresponding to an energy resolution of 2.8 eV. Consequently, background electrons are more likely to be trapped in the main spectrometer with the magnetic field setting of the SDS-IIIb long-term background measurement. The rate reduction of SDS-IIIb in comparison to SDS-IIIc may therefore be explainable by a mechanism, which removes trapped electrons from the sensitive flux tube (see also chapter 5.2).

To summarise, there are several open points, which might explain why the three measured background rates differ from each other. The influence of storage conditions on background electrons in the main spectrometer needs to be further investigated. Additionally, the possible influence of radon isotopes entering the main spectrometer through the pre-spectrometer has to be examined in future works. One approach which allows the test for radon decays in the main spectrometer is the analysis of the time development of the background rate.

6.1.2. Time Development and Statistical Model of the Rate

This chapter examines the time development of the rate with regard to irregularities like periods with elevated or reduced rate. Especially, it is tested if the distribution of the rate is Poissonian or distorted by for example stored electrons accompanying radon decays.

Figure 6.2 shows the rate in the electron ROI versus time for the SDS-IIIc background long-term measurement. The total average rate, determined by event counting divided by measurement time, is (287.7 ± 0.4) mcps. The blue data points display the rate, calculated for time segments with 4 h width. Large fluctuations are shown, in particular two outliers (after approximately five measurement days and at the seventh day) are likely not explainable by statistical fluctuations. If the rate is binned over a greater time range of 24 h (red data points), large fluctuations in comparison to the statistical uncertainty still exist. Several hypothesis tests (with 95 % CL) and calculations are preformed in the following to examine the time development of the rate.

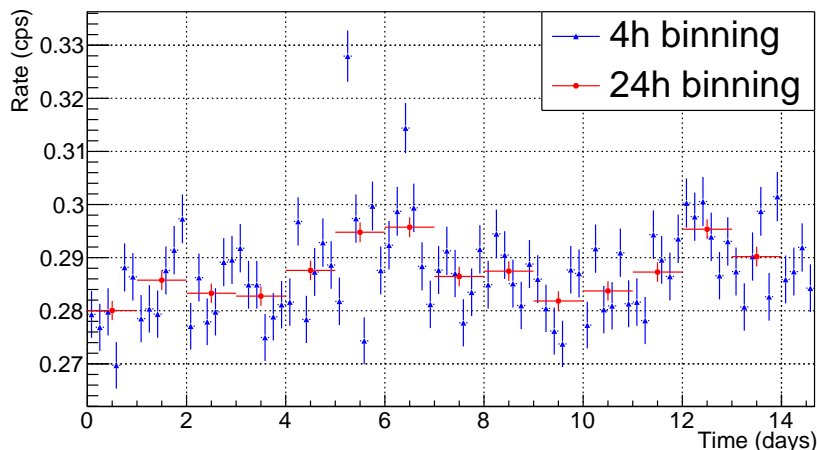


Figure 6.2.: Measured rate in the electron ROI versus time for the SDS-IIIc long-term background measurement. In blue the rate is calculated for 4 h time segments, in red for 24 h time segments. Both calculations show deviations, which cannot entirely be explained by statistical fluctuations.

At the beginning, the Allan deviation is calculated. The Allan deviation is a tool for describing the frequency stability of a system. Therefore, the total measurement time is split in small time ranges with length τ_0 . The electron rate is calculated for each of the time ranges. Accordingly, the Allan deviation is calculated for τ_0 . The deviation is the expectation value of the squared difference of consecutive mean rates. Afterwards another τ_0 is chosen and the Allan deviation for this τ_0 is calculated [Rob84].

The Allan deviation shows large values for small time binnings ($\tau_0 \approx 100$ s). A high deviation indicates large differences in the rate between two consecutive time ranges and therefore an instability in the background rate. The deviation decreases for increasing time scales between $\tau_0 \approx 100$ s and $\tau_0 \approx 6000$ s by more than one order of magnitude. The deviation is approximately constant at larger time scales than 6000 s. This points towards a stable rate. For further investigations, the Wald-Wolfowitz test is applied. Thereby, it is tested if the instability of the rate is caused by an underlying systematic trend or if it is still randomly distributed.

The Wald-Wolfowitz test (also runs-test) examines the similarity between two data sets. Therefore the observations from both data sets are combined and arranged in ascending order of magnitude. If the null hypothesis (the two data sets are from the same population) is true, the observations should be well mixed between coming from data set one and two [WW40]. Based on this statistic, a test for randomness is formulated. Therefore, one data set is replaced by a constant value, which is the mean value of the other data set. In the examined case, a run is a set of temporal, sequential values that are all above or below the mean value. The number of runs is linked via its expectation value and variance to a test statistic, which is asymptotically Gaussian distributed. The runs-test replaces the numerical values by ranks, therefore it is of no interest how far the actual value deviates from the constant value. In the test statistic, only the sequence is of interest. The runs-test is suggested to test the hypothesis of randomness against the existence of a trend or a regular cyclical movement [Noe50] [WW43].

The runs-test is applied to two time scales. The chosen time scales are 100 s, characterised as unstable by the Allan deviation, and 4 h, indicated as stable. The runs-test results for small time scales in a p-value of $p = 2.1 \times 10^{-4}$, the temporal sequence of the rate cannot be assumed to be random. The test statistic of the runs-test for large time scales is equal to $p = 0.14$, the null hypothesis is retained with confidence level 95 %. Consequently, the time development of the rate is assumed to be random on large time scales in contrast to small time scales. Hence, there seems to be an underlying effect which appears below the time scales of 4 h. One possible cause for this underlying effect is the storage of electrons with accompanying production of secondary electrons. The secondary electrons elevate the rate during the storage time, which is smaller than 4 h and may cause deviations from randomness.

To summarise, there is a structure in the time development of the rate on small time scales, which cannot be explained by randomness. The subsequent question is therefore, whether the discrepancy between the data points and the mean rate can be explained by statistical fluctuations. This question will be answered by the χ^2 -test.

The χ^2 -test examines, whether the data points x_i can be described within their statistical uncertainties by a certain model m_i with M free parameters. The test statistic is calculated to

$$S^2 = \sum_{i=0}^N \left(\frac{x_i - m_i}{\sigma_i} \right)^2,$$

with N as total number of data points. The test statistic S^2 follows a χ^2 -distribution with $M - N$ degrees of freedom, if the uncertainties σ_i are Gaussian distributed [Wal15]. S^2 can therefore be linked to a certain p-value.

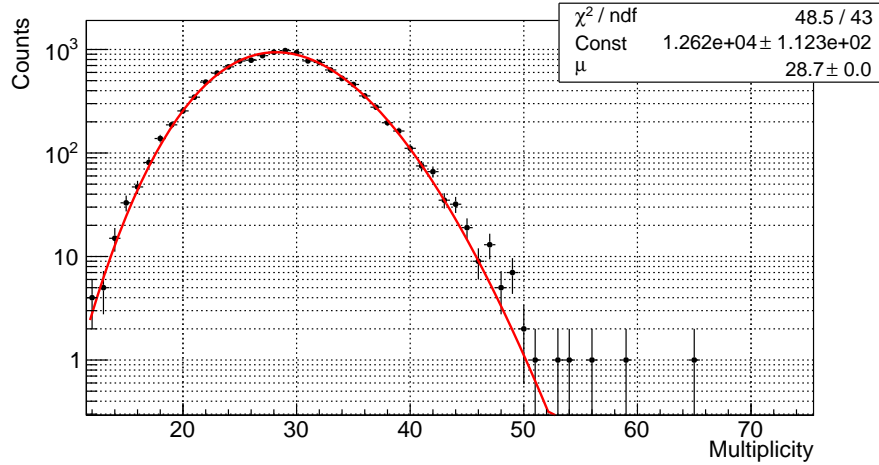


Figure 6.3.: Multiplicity plot of the SDS-IIIc long-term background rate fitted with a Poisson distribution. For this multiplicity plot, the measurement is binned in 100 s segments. The resulting distribution follows a Poisson distribution (95 % CL) with an estimated mean rate of (286.9 ± 0.4) mcps.

The uncertainty of the data points are expected to be Poissonian in the present case. However, a Poisson distribution can be assumed Gaussian for a mean value larger than $\mu = 25$, due to the central limit theorem [Wal15]. Thus, the application of the χ^2 -test is justified, if it is ensured, that each data point contains approximately 25 events.

The hypothesis test is performed for small (100 s) as well as for large time scales (4 h). The χ^2 -test examines, if the data points can be explained by a constant rate and consequently by Poissonian statistical fluctuations. The χ^2 -test rejects for small as well as for large time scales the null hypothesis ($p < 10^{-9}$). The data points are therefore not explainable by statistical fluctuations. The measured counts are displayed in a multiplicity plot, to further analyse the rate distribution.

The measurement time is binned in time segments of 100 s. For each time segment the number of measured events is counted and filled in a histogram, the so-called multiplicity plot (see chapter 3.3.2). In case the rate is Poissonian, the multiplicity plot should be describable by a Poisson distribution. Figure 6.3 displays the resulting multiplicity plot. It is well described by a Poisson distribution with a mean value of 28.7 events per time segment. Towards larger multiplicities a surplus exists, which might cause the small p-values of the χ^2 -test. Nevertheless an overall Poissonian behaviour of the measured rate can be approximated. The upward fluctuations of the rate after approximately five measurement days and at the seventh day can cause the surplus of events to larger multiplicities. Therefore the first upward fluctuation is investigated in more detail in the following.

The upward fluctuation of the rate after five days contains approximately 700 additional events over a time range of 3.5 h relative to the total average rate of (287.7 ± 0.4) mcps. The excess of the rate is in the whole detector and is not just focused on a certain area. This excludes detector systematics as possible source. Two effects remain, which might cause an elevation of the rate: high-energy stored particle(s) or hardware fluctuations.

The rate is elevated over a time range of approximately 3.5 h. A storage time on such time scales is possible due to the good vacuum conditions inside the main spectrometer. The energy of the primary electron can be estimated to

$$E_{\text{prim}} = N_{\text{sec}} \times 37 \text{ eV [MDF}^+13],$$

with N_{sec} as number of secondary electrons. Approximately 700 additional events result in a primary electron energy of 25.9 keV. An electron with this energy is normally not

stored in the main spectrometer over several hours (see chapter 4.1). Furthermore, the shape of the peak versus time follows a Gaussian function. The expectation is a Bragg peak structure [TM15] in case of a single trapped high-energy electron. In addition, if one high-energy electron would cause the elevated rate, the distribution of the rate would be non-Poissonian due to correlations of the secondary electrons. However, a multiplicity plot of this time range proves, that the Poisson distribution describes the measured rate. Nevertheless, the possibility remains, that several simultaneously trapped electrons in the main spectrometer cause the elevated rate. A superposition of the produced secondary electrons might result in the described properties. This needs to be investigated in future works.

Fluctuations of the hardware parameters can also explain an elevated rate. Several correlation analyses are therefore performed in the subsequent chapter.

6.2. Correlation of Rate with Slow-Control Parameters

The slow-control data of several hardware parameters are analysed to investigate a possible correlation to the elevated rate. Therefore, the sensors which monitor the magnetic field strength, the retarding potential, the vessel and detector temperature, the main spectrometer pressure and the temperature of the baffle system are examined (see table 6.1). These are the hardware parameters which are assumed to have an influence on the background rate. A correlation analysis (see chapter 5.4.2) quantifies the influence of the respective slow-control parameter on the measured rate.

The stability of the magnetic field in the analysing plane is characterised with three sensors in this analysis. The storage conditions for electrons in the main spectrometer change in case of fluctuations of the magnetic field strength in the analysing plane. More electrons are stored in an upward fluctuation, resulting in a reduced rate and the other way around. However, the fluctuations of the magnetic field strength during the long-term measurement are below the 10^{-3} level. Additionally, a nearly vanishing correlation factor is calculated. Low-energy background electrons are produced in the sensitive flux volume, which are accelerated by the retarding potential to the detector. Since the ROI is set to a fixed value, any fluctuations of the retarding potential would shift the electron peak versus the ROI. Consequently, the rate would be minimised. The relative standard deviation of the measured slow-control value is 10^{-5} , thus an influence of the retarding voltage can be excluded.

The major part of the background electrons is assumed to be caused by ionisation of Rydberg atoms by black-body radiation. The black-body radiation depends on the vessel temperature of the main spectrometer. A lower temperature results in a lower mean energy. Hence, less Rydberg states are ionised, which should reduce the background rate. Nevertheless, an influence of the vessel temperature on the rate can be neglected due to a vanishing correlation factor.

Changes of the temperature of the focal plane detector might vary the energy resolution and other related properties, which would result in a distorted rate measurement. However, the influence of the FPD carousel temperature on the rate can be neglected.

The probability for ionisation processes by trapped electrons increases with increasing main spectrometer pressure. Hence, the time structure for the production of secondary electrons changes (see chapter 7.1). This would support a peak-like excess of the rate. The deviation of the spectrometer pressure is measured to approximately 6%. However, an influence on the rate is not seen.

The baffle system is installed between the NEG material and the main spectrometer volume. It prevents ^{219}Rn from entering the sensitive flux tube. Normally the baffles are cooled to 83 K to freeze ^{219}Rn to its surfaces. The radon reduction factor decreases by an increase of the temperature, resulting in more radon decays in the main spectrometer. This would

Table 6.1.: Analysis of slow-control parameters during the SDS-IIIc long-term background measurement. In the first two columns the used slow-control parameters are named. The third column presents the correlation factor of a correlation analysis between the respective slow-control parameter and the rate in the electron ROI. The fourth column displays the mean value of each parameter, whereas in the fifth one the relative deviations are printed. The corresponding KATRIN numbers of the slow-control parameters are given in chapter B.

Parameter	Position Sensor	ρ	Mean	Rel. Deviation (%)
Magnetic field analysing plane (G)	Mid-Ring 9	-0.20	0.63	0.08
	Mid-Ring 23	0.15	0.63	0.07
	Mid-Ring 30	0.27	0.63	0.08
Retarding voltage (kV)	K-35	-0.20	18.60	2.1×10^{-4}
MS temperature (K)	Vessel	-0.17	282.55	0.07
FPD temperature (K)	Carousel	0.22	263.25	0.34
Vacuum pressure (mbar)	Extractor ion gauge	0.06	1.2×10^{-11}	6.41
Baffle 1 temperature (K)	Top	-0.27	83.06	0.23
	Bottom	-0.10	85.12	0.26
	Centre	-0.13	83.14	0.28
	Inlet	0.14	131.03	0.28
Baffle 2 temperature (K)	Top	-0.33	86.29	0.25
	Bottom	-0.19	88.55	0.41
	Centre	-0.15	86.88	0.54
	Inlet	0.12	115.33	0.26
Baffle 3 temperature (K)	Top	-0.29	82.95	0.16
	Bottom	-0.29	82.13	0.17
	Centre	-0.29	82.76	0.18
	Inlet	0.09	146.55	0.43

significantly elevate the rate. A stable behaviour below the percent level is measured in all baffle systems and also the rate seems to be independent of the temperature.

Consequently, any influence of instabilities in hardware parameters on the measured background rate can be excluded in the SDS-IIIc long-term measurement.

6.3. Energy Spectrum

The most important properties of the spectrometer background energy spectrum are explained by example of the SDS-IIa long-term background measurement [FLHE14]. In this measurement, the magnetic field in the analysing plane was set to 3.8 G, the retarding potential to 18.6 keV and the post acceleration electrode to 4 kV instead of the nominal 10 kV. Figure 6.4 presents in blue the measured energy spectrum. The black data points display the measured spectrum after a correction for the intrinsic detector background [FMJ⁺14]. The resulting estimate for the spectrometer background shows five characteristic peaks (A1-A5). Electron energies smaller than 4 keV are induced by detector effects and are therefore excluded from this analysis.

The first peak A1 corresponds to H⁻-anions, which are generated inside the spectrometer and are accelerated by the retarding potential. The incident energy of the anions on the detector is expected to be 22.72 keV [Har15]. Due to energy losses in the dead-layer of the

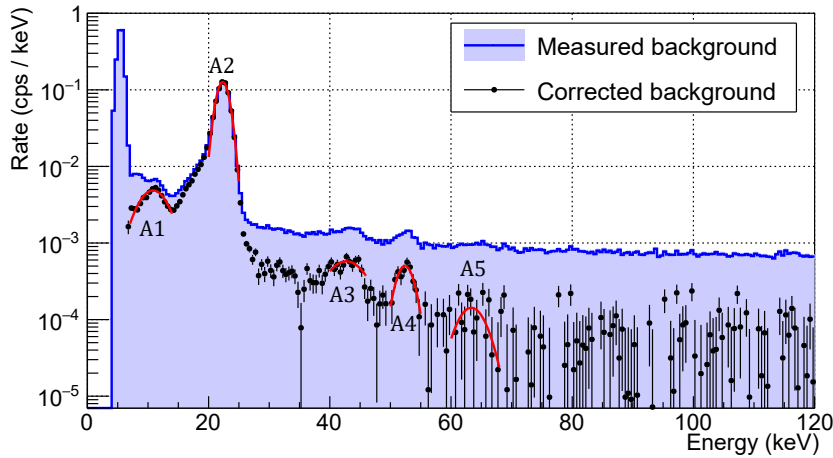


Figure 6.4.: Energy spectrum of the SDS-IIa long-term background measurement (blue line) and corrected for the intrinsic detector background (black points). Five characteristics in the estimated spectrometer background are shown. These are the ion peak (A1), electron peak (A2), pile-up peak (A3), ^{210}Pb L-shell (A4) and M-shell conversion line (A5).

detector [Sch14], they are measured with a reduced energy of (10.87 ± 0.04) keV. Peak A2 corresponds to the standard ROI. The retarding potential accelerates low-energy background electrons, which are produced in the sensitive flux volume, towards the detector. The fitted peak position is (22.277 ± 0.002) keV, the expected one is 22.72 keV. This shift is caused by the energy loss of electrons in the dead-layer at the detector surface. Pile-up effects in the detector cause peak A3. If more than one electron strikes the detector within the shaping length L in the same pixel (see chapter 3.2), the electrons cannot be separated and are counted as one event. The rate of the electron ROI dominates the overall background rate. Consequently, it is most likely that two uncorrelated background electrons of the electron ROI arrive within a small time range $\Delta T \leq L$ at the detector and cause pile-up. The recorded energy of two electrons with striking energy E_0 is given by

$$E = 2E_0 \left(1 - \frac{\Delta T}{2L}\right) \text{ [Sch14].}$$

The mean value of E_0 is the mean energy in the default ROI of 22.27 keV. Therefore, the peak position of A3 is approximately twice the striking energy of the standard ROI peak. The influence of the inter-arrival time ΔT on the recorded energy broadens the peak in comparison to A2.

Peak A4 has a mean energy of (52.4 ± 0.1) keV, which is equal to an initial electron energy of approximately 29.7 keV. A4 corresponds to the electron L-shell conversion line at (30.152 ± 0.001) keV [Cen18], accompanying the β -decay of ^{210}Pb in the spectrometer. The fifth peak A5 is a region of elevated rate and also caused by the decay of ^{210}Pb . The M-shell conversion electrons are expected at (65.240 ± 0.001) keV [Cen18]. The fitted mean peak position is (65 ± 1) keV [Har15].

The post acceleration electrode was set to its nominal value of 10 kV in the SDS-IIIc long-term measurement. Consequently, it is expected that A1, A2, A4 and A5 are shifted with 6 keV to higher energies. Since A3 is the pile-up peak of A2, the expected shift on A3 is 12 keV. Therefore, A2 and A3 are expected at the same energy of approximately 58 keV. In the SDS-IIIc measurement the magnetic field was set to a higher value compared to the setting of SDS-IIa. This results in a smaller sensitive flux tube volume and thus in a lower total background rate. Smaller rates lead to a decrease of peak A1 and A2. This

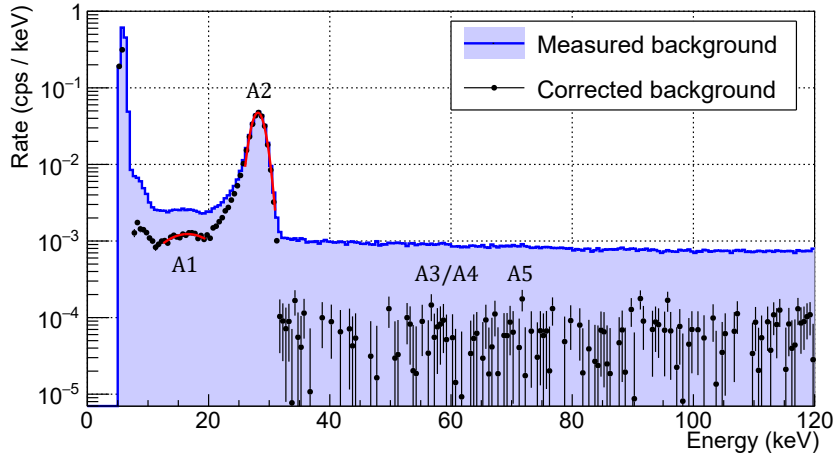


Figure 6.5.: Energy spectrum of the SDS-IIIc long-term background measurement (blue line) and corrected for the intrinsic detector background (black points). The measured rate per keV is lower in comparison to the SDS-IIa measurement, which is mainly due to a smaller sensitive flux tube volume. Furthermore, only the ion (A1) and standard electron peak are visible (A2), whereas the superposition of pile-up peak and L-shell conversion electrons (A3/A4) disappears. Also the M-shell conversion line A5 of ^{210}Pb is superimposed by statistical fluctuations.

yields to a lower probability for pile-up events and therefore also to a smaller peak A3/A4. The number of measured L- and M-shell conversion electrons of ^{210}Pb is also expected to decrease with the smaller sensitive flux volume of the main spectrometer. Hence, also there are smaller peaks expected.

Figure 6.5 presents the measured energy spectrum of SDS-IIIc. Events with smaller energies than 10 keV are classified as detector noise and are not taken into account. The ion peak A1 is measured at (16.5 ± 0.3) keV, which is in accordance with the expectation value. The electron peak A2 is expected at 28.7 keV and measured at (28.055 ± 0.002) keV. The magnetic field setting reduces both peaks in the rate by approximately factor two in comparison to figure 6.4.

The two further expected peaks in the energy spectrum at approximately 58 keV and 71 keV are not visible.

As previously mentioned, the expected peak A3/A4 at 58 keV is a superposition of the L-shell conversion line and the pile-up peak. The peak should therefore be larger than the statistical fluctuations and should be visible in the energy spectrum. However, in addition to the reduced pile-up probability, one further effect has to be taken into account. The magnetic field strength in the main spectrometer is larger in the SDS-IIIc measurement in comparison to SDS-IIa. This results in a higher magnetic shielding. The ^{210}Pb shell conversion electrons are emitted from the inner spectrometer surfaces. Hence, the probability for the conversion electrons to reach the sensitive flux volume decreases with increasing magnetic shielding. This effect reduces A3/A4 further, leading to its disappearance.

Already in the SDS-IIa measurement with larger sensitive flux volume and lower intrinsic shielding, the M-shell conversion line is not visible as a peak but as a region with elevated rate. Therefore it is reasonable, that A5 is superimposed by statistical fluctuations.

6.4. Pixel Distribution

The rate in the electron ROI as well as in the ion ROI is not uniformly distributed over the detector but shows some characteristics. These characteristics are described and investigated for each ROI in the following.

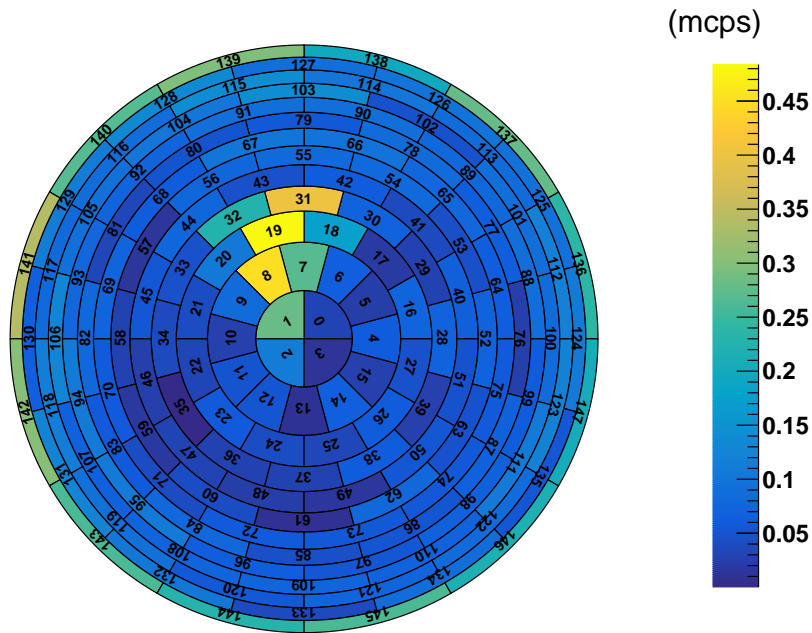


Figure 6.6.: Rate distribution in the ion ROI after correcting for the intrinsic detector background. Few pixels dominate the total rate in the ion ROI. The outermost detector ring shows an increase of the rate, which is not expected.

6.4.1. Pixel Disitribution in the Ion ROI

The ion ROI is defined from 13 keV to 19 keV in this analysis. A total rate of (29.9 ± 0.1) mcps is measured for this ROI in the SDS-IIIc long-term measurement. Figure 6.6 presents the pixel distribution for this energy range. The pixel distribution contains two unexpected features.

The first feature is, that few pixels measure a major part of the rate. Especially the pixels 1, 7, 8, 19 and 31 are highlighted in the measured rate in comparison to the other pixels. Figure 6.7 displays the energy distribution of pixel 8 (red data points) and 10 (blue data points), to investigate why few pixels measure a doubled rate in comparison to neighbouring pixels. The distributions show that the ion peak only exists in pixel 8 whereas in pixel 10 a constant rate versus energy is measured. Other highlighted pixels show the same characteristics in comparison to neighbouring pixels. Consequently, the H^- -anions are only measured in the highlighted pixels.

A similar behaviour of the ion pixel distribution already occurred in the SDS-IIa long-term background measurement. However, the measured structure in there is rotated by 90° in clockwise direction [FLHE14]. In both measurements, the magnetic field lines connect a closed valve with the detector. In the SDS-IIa measurement, the magnetic field lines lead to the valve between pre- and main spectrometer, in SDS-IIIc to the valve between pre-spectrometer and the transport section. In case the H^- -anions are produced on the inner surface of a valve, they have to overcome the retarding potential of 18.6 keV, as they are negatively charged. However, H^- -anions with starting energies in this range can be excluded. Consequently, the rotation in the ion distribution is not due to different valves. Further investigations concerning the distribution of the anions in the main spectrometer and their production mechanism are required.

The second unexpected feature is an elevated rate in the outermost detector ring in comparison to neighbouring rings. Similar to above, the ion ROI is further investigated by comparing the energy distribution of two neighbouring pixels. The energy distributions display, that the elevated rate is due to a flat increase of the rate in the ion energy region

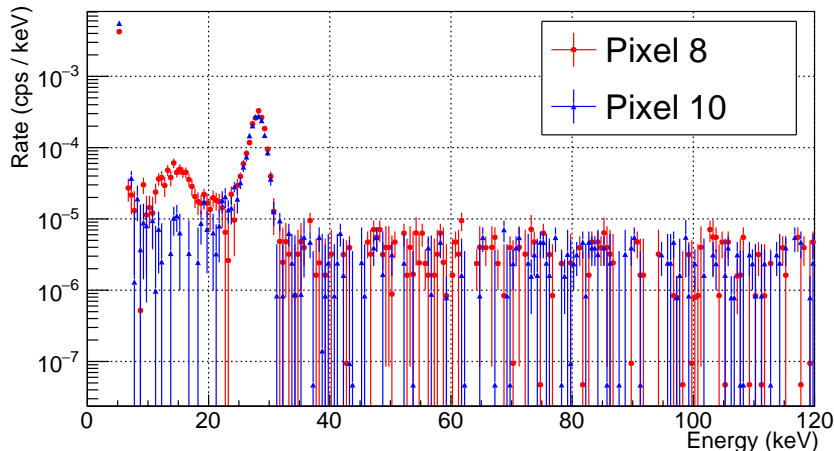


Figure 6.7.: Energy spectrum of the SDS-IIIc long-term background measurement of pixel 8 (red) and pixel 10 (blue) after correcting for the intrinsic detector background. Pixel 8 measures an ion peak, whereas pixel 10 shows a constant behaviour of rate versus energy in this region. The two distributions correspond to each other in the rate for energies larger than the ion ROI.

(see figure 6.9).

Backscattering of electrons is proposed as one possible explanation for this elevation of the rate [Frä18a]. Background electrons with an energy of approximately 28 keV backscatter at the detector and deposit each time only a part of their energy in the detector (see chapter 3.2). This would at first result in a smaller rate in the electron ROI in the outermost detector ring and secondly in an elevated rate below the electron ROI peak. Hence, this would also concern the rate in the electron ROI. A reduced rate in the outermost detector ring in the electron ROI is measured (see chapter 6.4.2) which underlines the backscattering hypothesis. Nevertheless, it is not reasonable, that backscattering mainly affects the outermost detector ring. Detailed detector simulations to this topic are planned.

Another possible explanation for the drop of the rate is a damage of the detector wafer. This is discussed in the following by example of the measured rate in the electron ROI.

6.4.2. Pixel Distribution in the Electron ROI

The rate in the standard electron ROI is determined to (287.7 ± 0.4) mcps, figure 6.8 displays the corresponding pixel distribution. Similar to the ion pixel distribution, two unexpected features occur in the electron pixel distribution. A drop of the rate at the outermost detector ring is shown as well as a surplus of events on the upper right side of the detector in contrast to the lower left.

One possible explanation for the drop of the rate in the outermost detector ring might be backscattering, as mentioned above. Detailed detector simulations need to test this hypothesis.

A more reasonable explanation for the measured drop of the rate is a damage of the detector wafer in the course of a Penning trap measurement. A Penning discharge occurred in this measurement with rates greater than 2 Mcps at the detector [Kip17]. Figure 6.9 compares the energy spectrums of pixel 128 and 140 for an explanation of the effects of the detector damages. Pixel 128 measures a rate of approximately 2.4 mcps in the standard ROI, whereas in the neighbouring pixel the rate is determined to approximately 1.4 mcps. The plot demonstrates, that the two electron ROI peaks are shifted against each other. Pixel 128 has a peak position of (27.81 ± 0.02) keV, pixel 140 (26.93 ± 0.05) keV. Consequently, a significant difference exists in the electron peak position of pixel 128 and pixel 140.

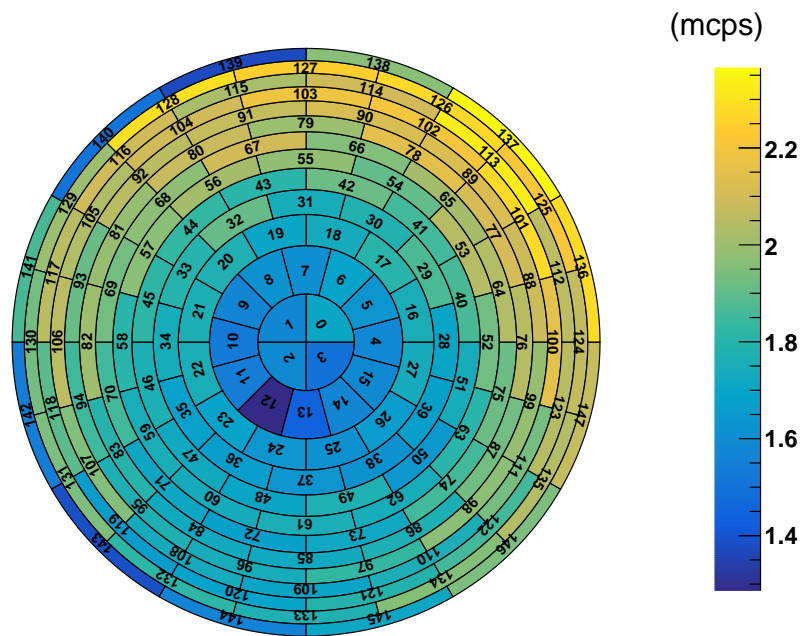


Figure 6.8.: Rate distribution in the electron ROI after correcting for the intrinsic detector background. The measured rate distribution has a radial and an azimuthal component. The drop of the rate at the outermost detector ring at the upper left side is not expected.

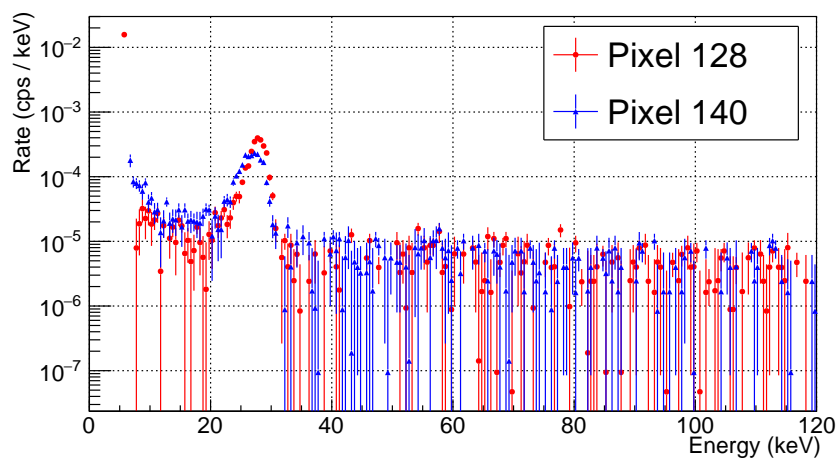


Figure 6.9.: Energy spectrum of the SDS-IIIc long-term background measurement of pixel 128 (red) and pixel 140 (blue) after correcting for the intrinsic detector background. The electron peak position of the two pixels are shifted from each other, which is likely to be related to damages of the wafer of the detector. Pixel 140 shows a larger rate for energies below the electron ROI which could be related to backscattering processes of electrons or to the damage of the detector wafer.

Additionally, the width of the electron peak is increased in pixel 140 ((1.87 ± 0.05) keV) relative to 128 ((1.35 ± 0.03) keV). A correlation analysis between the peak width and position results in a strong correlation with $\rho = -0.7$ [Frä18b]. This indicates that both effects have the same source. A long-term background measurement of the spectrometer background in mid 2017 shows a stable peak position and width of all pixels of the detector [RTBF17]. The SDS-IIIc long-term background measurement displays a large deviation of the peak positions and widths compared to the stability of the measurement performed in mid 2017. The change of the detector behaviour is traced back to the previously mentioned Penning discharge [Frä18b].

A correlation analysis is performed to test if the electron peak position of a pixel is connected to the determined rate in this pixel. A strong correlation is expected in case the shift on the peak position dominates the measured rate. The analysis results in a nearly vanishing correlation factor of $\rho = 0.1$. Consequently, the measured rate in the electron ROI is not dominated by the damage of the detector but by the intrinsic spectrometer background distribution.

The second unexpected feature is, that on the upper right side of the detector a larger rate is measured than on the lower left (see figure 6.8). Additionally, it seems that the minima of the rate distribution is not centred on the bulls-eye of the detector but at pixel 12, thus shifted to the lower left. The major part of the spectrometer background is produced by Rydberg atoms accompanying the decay of ^{210}Pb (see chapter 4.6). ^{210}Pb is implanted in the spectrometer surfaces as a result of the decay of ^{222}Rn and should therefore be isotropically distributed over the whole spectrometer surfaces. The spectrometer is radially symmetric in its cross-section. The magnetic flux tube, which guides the background electrons from the sensitive flux volume to the detector is also radially symmetric. Hence, it is expected that the spectrometer background distribution is only dependent on the radius and independent of the azimuth angle.

The azimuth angle distribution of the SDS-IIIc long-term background measurement is plotted to investigate the surplus of events at the upper right side of the detector. The calculation of the azimuth angle distribution needs the exact positions of the measured events. It is only known, in which pixel the respective event is measured, the exact position of the event is unknown. To assign an exact position, each event is placed randomly in the pixel in which it is measured. Figure 6.10 displays the resulting azimuth angle distribution.

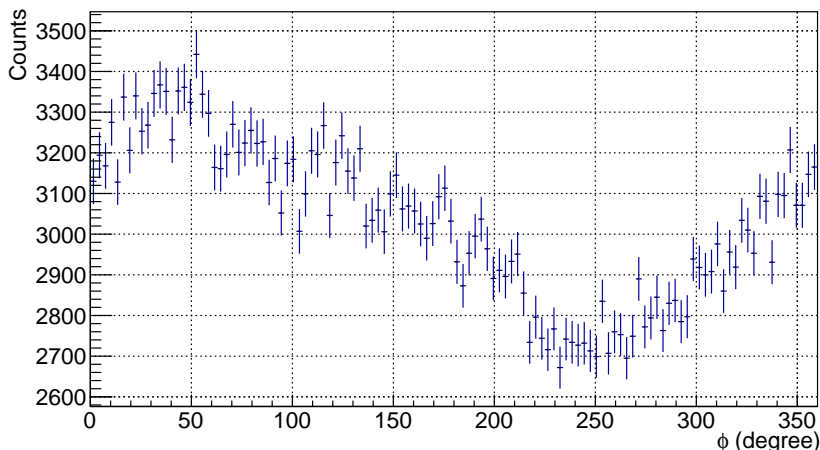


Figure 6.10.: Azimuth angle distribution of the SDS-IIIc long-term background measurement. An azimuth angle of $\phi = 0^\circ$ corresponds to the position of 3 o'clock at the detector, with increasing ϕ the position changes counterclockwise. The measured azimuth angle distribution cannot be explained by isotropy.

An isotropic distribution is expected for a background profile which is only dependent on the radius. However, the azimuth angle distribution is not isotropic, it rather has a sinusoidal shape. The distribution shows a surplus of events for an azimuth angle below 90° , which corresponds to the upper right side of the detector. A deficit of events is measured at approximately $\phi = 240^\circ$, which corresponds to the lower left side. The surplus of events relative to the mean value is quantified to approximately 14%. Thus, the azimuth angle distribution confirms the impression, that the rate distribution is also dependent on the azimuth angle. However, this azimuth angle dependence cannot be explained by the production mechanism of the background electrons.

One possible explanation for the anisotropy in the azimuth angle distribution is a misalignment in the mechanical set-up of the main spectrometer vessel relative to the detector. In case the centre of a radially symmetric distribution is shifted in comparison to the centre of a detector, a sinusoidal shape is measured in the azimuth angle distribution of the detector. The size of the shift thereby influences the amplitude of the sinusoidal shape. An analytical description shows, that a sinusoidal shape only occurs if the shift at the detector is small compared to the extensions of the detector [Frä06]. The misalignment in the spectrometer and detector section is discussed in more detail in chapter 7.

6.5. Conclusions

The goal of the SDS-IIIc long-term background measurement is to enable a characterisation of the spectrometer background in an electric and magnetic field configuration similar to neutrino mass measurements. The magnetic field strength in the analysing plane is 6 G, the inner electrode offset amounts to 200 V.

The volume-normalised rate of SDS-IIIc is elevated in comparison to former measurements in the flux tube of the 6 G-setting. The increase is likely to be attributed to changed storage conditions for electrons in the main spectrometer. Additionally, a contribution of ^{219}Rn emanation from the NEG material of the pre-spectrometer is possible.

The time development and statistical model of the background rate shows unexpected features. The runs-test proves, that the fluctuations of the rate on time scales of $\mathcal{O}(100\text{ s})$ cannot be assumed to be temporal random, thus an underlying trend is likely. In contrast, the rate is almost randomly distributed on time scales of $\mathcal{O}(4\text{ h})$. The measured rate has outliers to higher rates, which cannot be explained by statistical fluctuations. It is likely, that several simultaneously stored electrons cause these higher rates by ionisation of residual gas. Nevertheless it is assumed in first-order approximation that the overall rate is Poissonian distributed.

A stability analysis of relevant hardware parameters indicate, that all parameters are stable on the percent level. Correlation analyses of the slow-control parameters with the measured electron rate show that the hardware parameters seem to have vanishing influence on the rate.

The characteristic peaks of the background energy spectrum are examined. The peak caused by ions and the one caused by electrons are close to the expected positions. The L-shell and M-shell conversion line electrons accompanying the β -decay of ^{210}Pb are effectively shielded.

The pixel distribution of the ion ROI displays, that the rate in this ROI is focused on few pixels. The cause for this behaviour remains unknown. The outermost detector ring shows an elevated rate in comparison to the neighbouring detector ring, which is likely due to a damage of the detector wafer. Similar indications for a damage are found in the pixel distribution of the electron ROI. Additionally, the azimuth angle distribution of the electron ROI might point to misalignment of the spectrometer vessel in comparison to the detector.

7. Alignment Studies

In the SDS-I measurement campaign, 22 detector pixels could not be used due to mechanical misalignment in the KATRIN set-up. Thereby, the flapper valve in the pinch magnet produced a shadowing effect, which blocked parts of the $191\text{ T}\cdot\text{cm}^2$ flux tube. The misalignment occurred due to the complex connection procedure of the detector system to the main spectrometer. Several measures were carried out before the SDS-II phase to improve the alignment [Har15].

Nevertheless, the measured background pixel distribution in SDS-IIc still indicates a misalignment between the main spectrometer vessel and the detector (see chapter 6.4). This chapter therefore investigates possible misalignments of several KATRIN components relative to the detector in the spectrometer and detector section. The three examined alignments are important for the neutrino mass measurements and for the spectrometer background model.

Chapter 7.1 determines the alignment between the magnetic main axis of the main spectrometer and the detector by using radon decays. This alignment is required to calculate the centre of the magnetic flux tube at the detector, which guides the β -decay electrons of tritium from the source to the detector.

Subsequent the alignment of the inner electrode geometry and the magnetic flux tube is determined in chapter 7.2. The inner electrodes fine-shape the retarding potential in the main spectrometer. The investigated alignment therefore equals the position of the flux tube in comparison to the retarding potential.

The last chapter 7.3 quantifies the misalignment between the spectrometer vessel and the detector, which is important for the background model. Additionally, this analysis enables a cross-check of the existing background model.

7.1. Alignment of the Flux Tube

This chapter calculates the mean position of the magnetic flux tube on the detector. The position of the flux tube on the detector can influence the mean position of the β -decay electrons on the detector in neutrino mass measurements. Radon rings are used, to determine the centre of the magnetic flux tube.

The NEG material, which is installed in both KATRIN spectrometers to achieve the good vacuum conditions, emanates the radioactive radon isotope ^{219}Rn (see chapter 4.4). High-energy electrons accompany the α -decay of radon. These electrons are trapped in axial direction in the main spectrometer in a magnetic bottle (see chapter 4.1). A trapped electron follows the magnetic field lines in the main spectrometer on a small cyclotron path. Additionally, a magnetron drift around the magnetic main axis takes place. The trapped electron loses energy until it breaks the storage condition. The cross-section for inelastic scattering with residual gas increases with decreasing electron energy. Therefore, the dominant cooling-down mechanism for the trapped electrons is inelastic scattering. Secondary electrons are generated via ionisation in the inelastic scatter processes. Those

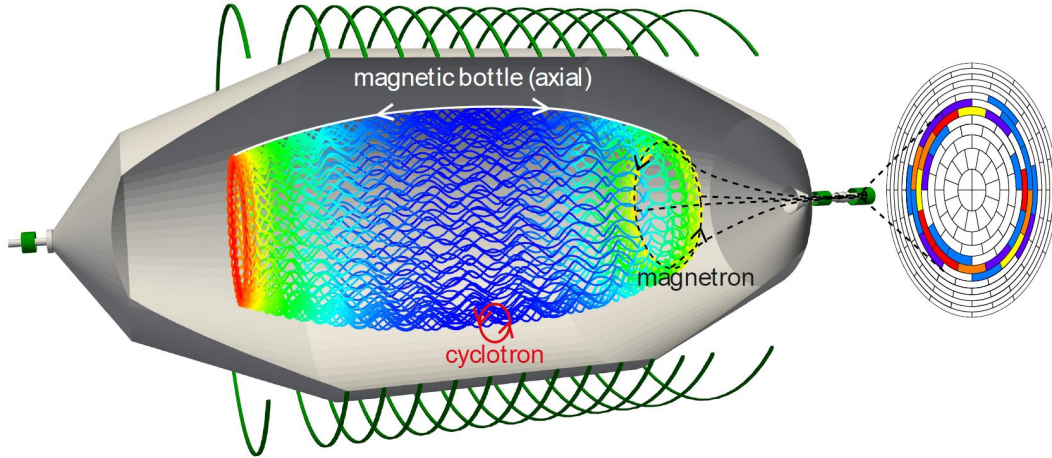


Figure 7.1.: Trajectory of trapped electrons in the main spectrometer. The magnetic mirrors at both exits of the spectrometer trap the electrons in axial direction. The trapped electron performs a slow magnetron drift around the magnetic main axis of the spectrometer, which is superimposed by the cyclotron motion. The stored electrons go through a cooling-down mechanism, in which they produce secondary electrons at the same magnetron radius. These secondary electrons can leave the trap and form a ring-like structure on the detector [Har15].

secondary electrons follow the same magnetron radius as the primary and can also be trapped depending on their kinematics. If they are trapped, they can produce further electrons, which follow the same magnetron radius. Hence, one high-energy electron produces up to hundreds of secondary electrons, which follow the same magnetron motion around the magnetic main axis of the spectrometer [Har15]. This results in a ring-like structure of secondary electrons on the detector. The radius of the circular shape is the magnetron radius projected onto the detector. The centre of the measured ring corresponds to the magnetic main axis of the spectrometer and therefore also to the centre of the magnetic flux tube. Figure 7.1 shows schematically the trajectory of trapped electrons and the resulting ring-like structure on the detector.

Ring-like structures were produced in large numbers in a dedicated measurement in December 2017 [Frä17d]. The goal of this measurement is to quantify a possible misalignment between the magnetic main axis and the detector. Therefore two changes in the experimental setting are made in comparison to the nominal setting. First, the baffles are warmed up to room temperature to increase the number of radon decays in the main spectrometer. Second, the pressure in the main spectrometer is elevated by three orders of magnitude to 2.5×10^{-9} mbar. This enables a separation of uncorrelated background events from correlated events by trapped electrons, as explained in the following.

The magnetic bottle of the main spectrometer can trap high-energy electrons for several hours, due to the excellent vacuum conditions [MDF⁺13]. This makes it difficult to relate a single event to a certain radon decay. The storage time of the high-energy electron decreases to the range of seconds by elevating the pressure by three orders of magnitude. The decrease in the storage time is due to an increasing probability for inelastic scattering with residual gas [Wan13]. Single radon decays therefore appear as a short burst of correlated secondary electrons, which can be identified by the inter-arrival time of the events [Har15].

Figure 7.2 shows the inter-arrival time distribution of the measurement of December '17. The distribution for inter-arrival times greater than 0.5 s follows an exponential function. This is expected for Poissonian rates. A surplus of events with respect to the Poissonian model is measured at smaller inter-arrival times. Clustered bursts of secondary electrons

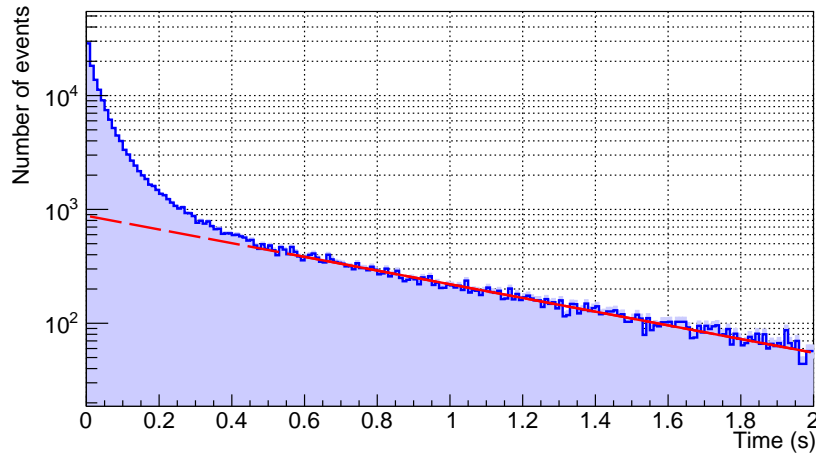


Figure 7.2.: Inter-arrival time distribution for the high pressure measurement of December '17 with warm baffles in the electron ROI. For larger inter-arrival times than 0.5s, the inter-arrival time distributions follows an exponential behaviour as expected for Poissonian rates. The distribution to smaller inter-arrival times is dominated by correlated events of radon decays.

as a result of radon decays cause this surplus. The correlated electrons dominate the distribution for inter-arrival times smaller than 0.4s (note the logarithmic y-axis).

The burst of a radon decay is identified with a cluster analysis by the *Kasper* software. The time window is set to $t_0 = 0.4\text{s}$ in the analysis, as clustered events dominate the inter-arrival time distribution for times smaller than t_0 . The algorithm of the cluster analysis starts from the first measured event and calculates, whether the consecutive event has a smaller inter-arrival time than t_0 . If not, the first event is identified as a single, uncorrelated event. The first two events are identified as correlated events if the inter-arrival time is smaller than t_0 . In the next step, the algorithm examines whether the inter-arrival time between the second and the third event is smaller than t_0 . If this is true, the third event is added to the cluster. If not, the cluster consists only of the two first events. Based on this scheme, the algorithm analyses all measured events in the electron ROI.

The following analysis takes only clusters into account, which contain 12 or more events. A Monte Carlo simulation demonstrates that for this threshold a purity of 99.3% of correlated events is given.

It is expected, that the identified bursts form a ring-like structure on the detector (see detector in figure 7.1). A circle fit calculates the radius and the position of the centre for each burst. The fit routine is implemented in *Kasper* and based on the Hough Transform [BAL].

In the following, a so-called “black-and-white” analysis is performed. Therefore, the analysis includes each pixel, which measures at least one event in the respective cluster, with the same weighting. If a pixel is hit more often, it is probably related to the fact that the trapped primary electron has little energy in the corresponding volume. The cross-section for inelastic scattering increases with decreasing energy. Hence, the production of secondary electrons is more probable.

The ring fit needs the exact position of each event. However, only the coordinates of the pixel, which measures the event, is known. This is the highest experimental resolution in KATRIN. 40 events are randomly placed in each pixel, which is hit by secondary electrons in the cluster, to generate the exact event position. A high number of artificial events is chosen due to two reasons. First, the probability of the fitter to determine the ring

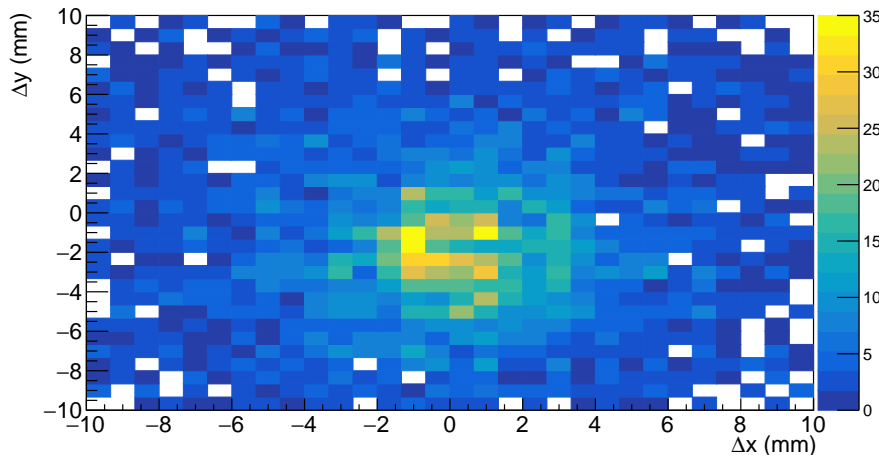


Figure 7.3.: Positions of the centres of the fitted radon rings. The resulting distribution has the mean values $\Delta x = (0.09 \pm 0.08)$ mm and $\Delta y = (-1.74 \pm 0.10)$ mm. The width of the distribution is $\sigma_x = (4.0 \pm 0.1)$ mm and $\sigma_y = (4.6 \pm 0.1)$ mm.

structure increases with the number of events. Second, the influence of the artificial event position generation decreases with more events.

In total 3925 radon rings, consisting of more than 12 events, are identified. Figure 7.3 shows the distribution of the coordinates of the fitted centres. The mean position of the distribution and thus also the position of the flux tube at the detector is $\Delta x = (0.09 \pm 0.08)$ mm and $\Delta y = (-1.74 \pm 0.10)$ mm. The width of the distribution results from smearing due to the individual cyclotron motion of the secondary electrons. Hence, the width of the distribution is of no interest for this misalignment study.

7.2. Alignment of the Retarding Potential

The inner electrodes fine-shape the retarding potential. Therefore, the inner electrodes comb structure position is an indication for the position of the retarding potential. Consequently, calculating the structure position enables a quantification of the misalignment between the retarding potential and the magnetic flux tube. A possible misalignment influences the transmission properties of the main spectrometer for β -electrons.

Low-energy background electrons are produced at the inner electrode comb structure. An appropriate magnetic field guides these electrons to the detector [Sch14]. Hence, the circular comb structure is projected onto the detector (see figure 7.4). The centre of the circular projection of the comb structure on the detector is determined by a ring fit. However, the magnetic field projects the structures onto the detector. Thus, the misalignment of the magnetic main axis of the main spectrometer versus the detector, determined in chapter 7.1, affects the centre of the projected comb structure at the detector. Nevertheless, only the misalignment of the retarding potential relative to the magnetic flux tube is of interest for the neutrino mass measurements in KATRIN. This is equal to the centre of the inner electrode comb structure relative to the magnetic main axis of the main spectrometer at the detector.

The comb structure is projected onto the detector by an asymmetric field setting. The upstream magnet of the main spectrometer is switched off for this purpose. The magnetic field lines thus lead from the spectrometer vessel to the detector. The LFCS fine-shapes the magnetic field and projects exactly one comb structure onto the detector. Seven different comb structures are sequentially mapped onto the detector in a dedicated measurement [Frä17a]. The following analysis does not take the last comb structure into account due

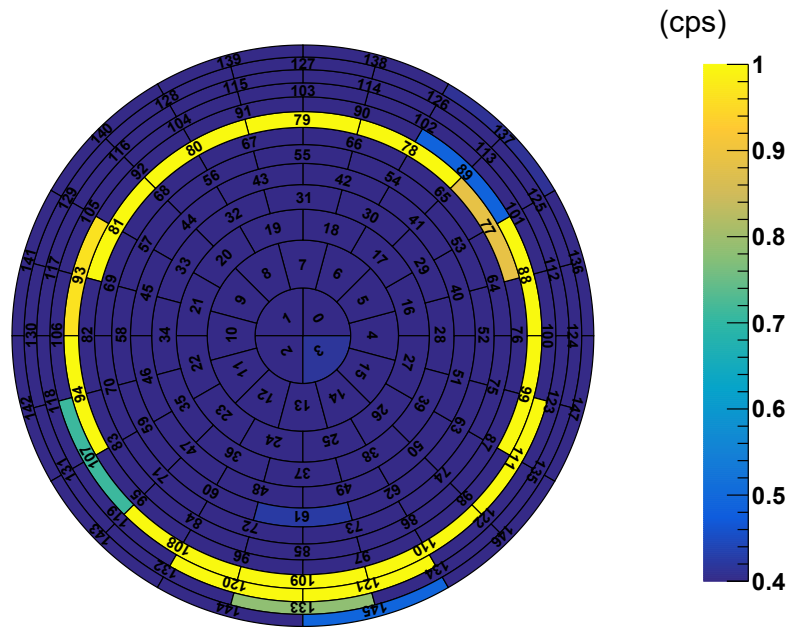


Figure 7.4.: Ring structure on the detector due to secondary electron emission from the inner electrode comb structure. The centre of the ring on the detector is fitted to $\Delta x = -0.3$ mm and $\Delta y = -3.9$ mm.

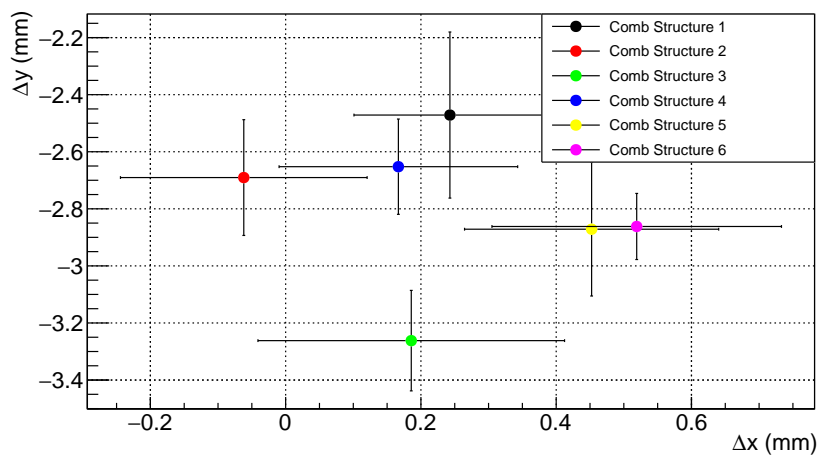


Figure 7.5.: Positions of the centres of the circles of the inner electrode comb structure. In first-order approximation, the comb structures are in accordance with each other, which results in a constant shift between beamline and inner electrode comb structure. The mean position of the inner electrode comb structures at the detector is $\Delta x = (0.25 \pm 0.07)$ mm and $\Delta y = (-2.80 \pm 0.08)$ mm.

to additional collisions of the flux tube with the spectrometer vessel. Each of the six electrode comb structures is scanned with 21 different magnetic field settings to increase the resolution.

The analysis is performed similar to chapter 7.1 in a black-and-white analyses. Figure 7.5 displays the mean centres of the fitted circles for each comb structure. The uncertainty on the mean centre is calculated in simulations with bootstrap [Fel85].

The different inner electrode comb structures vary in their position at the detector. However, they are approximately in accordance with each other within the statistical uncertainty. Thus, the comb structures of the main spectrometer are not tilted in comparison to the magnetic flux tube in first-order approximation. However, a constant shift versus the flux tube is measured. The flux tube is located at $(\Delta x, \Delta y) = (0.09 \text{ mm}, -1.74 \text{ mm})$ at the detector (see chapter 7.1), the comb structures are in mean located at $(0.25 \text{ mm}, -2.80 \text{ mm})$. Consequently, the retarding potential is misaligned versus the magnetic flux tube. The misalignment in x-direction amounts to $(-0.16 \pm 0.11) \text{ mm}$ at the detector, in y-direction to $(1.06 \pm 0.12) \text{ mm}$.

7.3. Alignment of the Main Spectrometer Vessel

The misalignment of the main spectrometer vessel itself relative to the detector is investigated in this chapter. Therefore, the distribution of the spectrometer background electrons is examined in detail. Assuming a homogeneous distribution of the ^{210}Pb contamination on the inner spectrometer surfaces, it is expected that the spectrometer background distribution is radially symmetric (see chapter 4.6). The magnetic flux tube, which guides the background electrons to the detector, is designed to be radially symmetric. Hence, it is expected that the detector measures a radially symmetric spectrometer background. A deviation of this radially symmetric background might point towards misalignment (see chapter 6.4.2) and can be used to quantify this misalignment.

Therefore, chapter 7.3.1 analyses the data of long-term background measurements to quantify a possible misalignment between the spectrometer vessel and the detector. Additionally, it is tested whether the measured features are due to misalignment. The background distribution is further examined in chapter 7.3.2 for a cross-check with the existing background model.

7.3.1. Quantification of Misalignment

The main spectrometer background was measured in the SDS-IIa phase over a time range of approximately one week in 2014 [FLHE14]. The upper graph of figure 7.6 shows the pixel distribution at the detector for this long-term measurement. The pixel view indicates a deviation from the expected radially symmetric distribution. A surplus of measured events at the upper left side of the detector exists in comparison to the lower right. Additionally, the minima of the distribution seems to be shifted to the lower right side instead of being focused at the bulls-eye of the detector.

An appropriate tool for testing the radial symmetry of a distribution is the analysis of the azimuth angle. The azimuth angle distribution is calculated to show, that the measured distribution at the detector is not radially symmetric. The calculation of this distribution is performed as described in chapter 6.4.2. An azimuth angle of $\phi = 0^\circ$ corresponds to the position of 3 o'clock at the detector. The position changes counterclockwise with increasing ϕ . The lower graph of figure 7.6 displays the measured azimuth angle distribution. A radially symmetric background should result in an isotropic distribution. However, the measured distribution is not isotropic, it follows a sinusoidal shape. The peak of the distribution is around 150° , which corresponds to a surplus of events at the upper left detector side. The surplus of events relative to the mean value is approximately 16%.

The thesis of F. Fränkle [Frä06] shows in an analytical calculation, that a sinusoidal shape of the azimuth angle distribution can be caused by a misalignment between the detector and

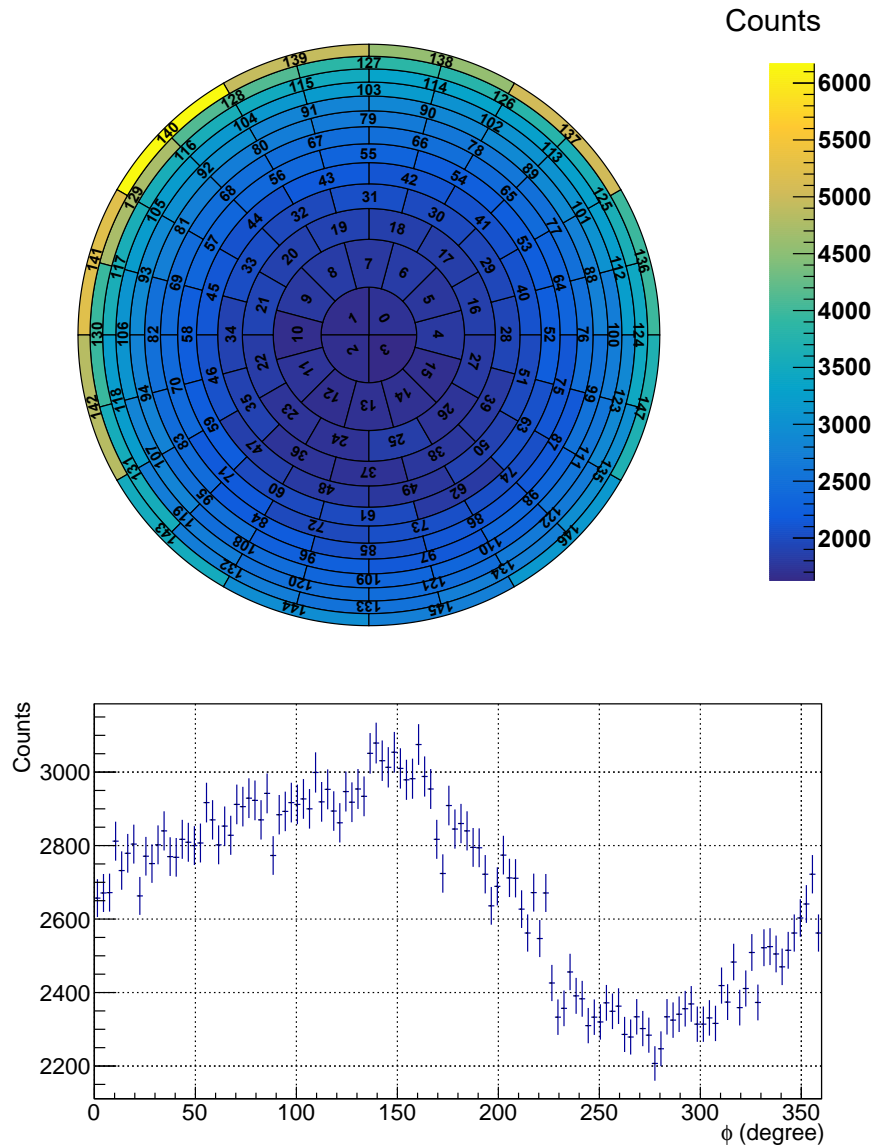


Figure 7.6.: Pixel distribution of the SDS-IIa long-term background measurement (upper graph) and corresponding azimuth angle distribution (lower graph). A radially symmetric distribution of the background electrons from the main spectrometer is expected, however the pixel distribution in the upper graph does not show this behaviour. At the upper left side of the detector a surplus of events is seen and less events in the lower right. This is confirmed by the azimuth angle distribution in the lower plot.

a radially symmetric distribution. To test, if the measured distribution can be explained by misalignment, it is searched for an effective shift. This shift is applied to all measured events, to get a radially symmetric background. Simultaneously this shift is equivalent to the projected misalignment between main spectrometer and detector.

As mentioned previously, it seems like the distribution is shifted to the lower right. Hence, effective shifts towards upper left are primarily tested. In y -direction shifts between 2 mm and 5.5 mm are tested, in x -direction shifts between -2 mm and 1 mm with a step size of 0.08 mm. The azimuth angle distribution is calculated for each applied shift and without the three outermost detector rings. A lack of events appears at the lower side of the detector by shifting all events upwards. Hence, the outermost rings would distort the azimuth angle distribution. The width of the three outermost rings corresponds to the maximally tested

shift of 5.85 mm.

The azimuth angle distributions is compared with the hypothesis of isotropy for each applied shift. The χ^2 -test and the runs-test are used for comparison. The χ^2 -test investigates whether the azimuth angle distribution is in accordance with isotropy within the statistical uncertainty. The runs-test examines the sequence of the values for isotropy (see chapter 6.1.2). For the runs- as well as for the χ^2 -test, a distribution of test statistics arises for each applied shift. It is searched for the absolute minimum in the two distributions as the corresponding azimuth angle distribution shows the highest accordance with isotropy. Consequently, the shift, which is linked to this azimuth angle distribution, is the optimal shift to get a radially symmetric distribution in the detector.

It is necessary to simulate the exact positions of the measured events to calculate the azimuth angle distribution (see chapter 6.4.2). 200 different data sets are generated, based on the SDS-IIa measurement, to quantify the influence of the simulation. The runs-test and the χ^2 -test calculate for each data set the optimal shift. The distribution of the optimal shifts of the 200 data sets, determined by the χ^2 -test, are fitted by a two-dimensional Gaussian function. The resulting mean of the Gaussian function is the effective shift. The same routine is performed with the results of the runs-test.

The effective shift, calculated with the runs-test, amounts to $\Delta x = (-0.76 \pm 0.75)$ mm and $\Delta y = (4.98 \pm 0.72)$ mm. The χ^2 -test results in an effective shift of $\Delta x = (-1.07 \pm 0.19)$ mm and $\Delta y = (4.84 \pm 0.32)$ mm. Hence, both methods result in the same shift within the statistical uncertainty. A shift of approximately 5 mm in total to the upper left for all events is recommended, to get a radially symmetric background distribution in the detector. The χ^2 -test shows a more stable behaviour in the statistical uncertainty. Therefore, it will be focused only on the effective shift calculated by the χ^2 -test in the following.

The detector was realigned between the SDS-II and SDS-III measurement phase. Thus, it is reasonable that also the effective shift changes. It is therefore determined in the following for the data taken in the SDS-IIIb [RTBF17] and the SDS-IIIc long-term background measurements [Frä17e]. The effective shift for the background distribution of the SDS-IIIb measurement is $\Delta x = (0.56 \pm 0.37)$ mm and $\Delta y = (6.60 \pm 0.11)$ mm. Thus, a shift of all events to the upper right side is recommended with the new alignment. The direction of the shift remains the same in the SDS-IIIc measurement with respect to SDS-IIIb. However, the size of the shift changes to $\Delta x = (1.76 \pm 0.52)$ mm and $\Delta y = (8.89 \pm 0.58)$ mm. The alignment of the detector relative to the spectrometer vessel remained constant between these two measurements. Nevertheless, different magnetic field settings were used in the two measurements: in SDS-IIIb a 2.7 G-setting was used, in SDS-IIIc a 6 G-setting. These two measurements with the same alignment but a different magnetic field setting are used to determine, if the sinusoidal shape of the azimuth angle distribution is caused by misalignment or due to unknown background sources.

The major part of the background electrons is produced in the cylindrical section of the main spectrometer due to its large volume. If the sinusoidal shape is caused by misalignment, it is therefore a misalignment of the cylindrical section of the spectrometer vessel relative to the detector. The misalignment is constant in this section, since the spectrometer vessel is not tilted versus the beamline in first-order approximation (see chapter 7.2). The analysing plane lays within the cylindrical section of the main spectrometer and therefore represents this section. The magnetic field setting of the respective measurement defines the projection of the analysing plane on the detector. If misalignment causes the shape of the azimuth angle distribution, the effective shifts of the SDS-IIIb and SDS-IIIc measurements should result in the same shift in the analysing plane. However, different shifts in the analysing plane indicate a physical azimuthal component of the background distribution in the main spectrometer and therefore an incomplete background model.

The extensions in the analysing plane of both magnetic field settings are calculated with the software *Kassiopeia*. The projection of the effective SDS-IIIb shift results in

a shift of $\Delta x = (5.6 \pm 3.2)$ cm and $\Delta y = (59.7 \pm 0.9)$ cm in the analysing plane. The projected effective shift of the SDS-IIIc data is calculated to $\Delta x = (11.1 \pm 3.3)$ cm and $\Delta y = (56.1 \pm 3.6)$ cm. In x-direction the two shifts are not compatible. Nevertheless, they both show a large statistical uncertainty. The shifts in y-direction are compatible. It is assumed, that the two shifts are the same in first-order approximation, as the difference in x-direction is not significant with 95 % CL. This underlines the hypothesis, that the sinusoidal shape of the azimuth angle distribution is caused by misalignment of the detector relative to the spectrometer vessel. The misalignment is quantified to $\Delta x = (-8.4 \pm 4.5)$ cm and $\Delta y = (-57.9 \pm 3.7)$ cm in the analysing plane.

7.3.2. Cross-Check with Background Model

The background model assumes that the azimuth angle distribution is isotropic after correcting it for the misalignment of the main spectrometer vessel relative to the detector. The effective shift, calculated in chapter 7.3.1, delivers this correction.

The upper graph of figure 7.7 displays the electron background distribution of the SDS-IIa measurement after applying the effective shift. The pixel distribution seems to be radially symmetric. However, the azimuth angle distribution (lower graph of figure 7.7) is not compatible with isotropy. Nevertheless, the shift reduces the anisotropy from 16 % to 5 %. The azimuth angle distribution shows a surplus of events at approximately 0° and 180° . The periodicity indicates, that the azimuth angle distribution is described by a sinusoidal function with two oscillations over 360° . Hence, the 200 generated data sets to calculate the effective shift of the SDS-IIa data are investigated with respect to these two peaks. The events are shifted by the effective shift and the resulting azimuth angle distribution is fitted with the sinusoidal function. The function describes the distribution in 180 of the 200 data sets with 95 % CL. The remaining 20 data sets also show the two peaks in the azimuth angle distribution. The mean peaks of the fit functions are at $2.8^\circ \pm 1.2^\circ$ and $182.8^\circ \pm 1.2^\circ$. Consequently, the background distribution shows a quadrupole structure after applying the shift. A surplus of events is measured from the left and right side of the detector and less from top and bottom.

The data of the SDS-III measurements show the same quadrupole structure after applying the effective shift. The peaks in the azimuth angle distribution are also at 2° and 182° . Consequently, the quadrupole structure might be caused by a systematic error in the analysis or due to physical reasons.

One possible reason for this quadrupole structure is, that it is arising as an artefact of an incomplete shift. For the explanation, a certain “true” misalignment between vessel and detector \vec{m}_0 is assumed. In case the effective shift is determined not exactly to \vec{m}_0 but to a slightly deviating shift, this could result in a distorted azimuth angle distribution and lead to the quadrupole structure. This theory is examined with a Monte Carlo simulation. The simulation shows, that an incomplete shift does not result in a quadrupole structure in the azimuth angle distribution. Consequently, the quadrupole structure seems to be caused by physical reasons.

One physical reason for the quadrupole structure is a deformation of the magnetic flux tube. The magnetic flux tube is fine-shaped by the LFCS. The LFCS air-coils are designed as circles. However, gravitational effects might deform them into an elliptical shape. This would result in a deformation of the magnetic flux tube. The magnetic flux tube leads the background electrons to the perfectly circular detector. Hence, a deformation of the flux tube results in distorted projection of the background electrons. Consequently, a quadrupole structure might be formed. Simulations regarding this topic are ongoing. Studies to possible deformations of the LFCS air-coils are given in [EBB⁺18] and [KAT18b].

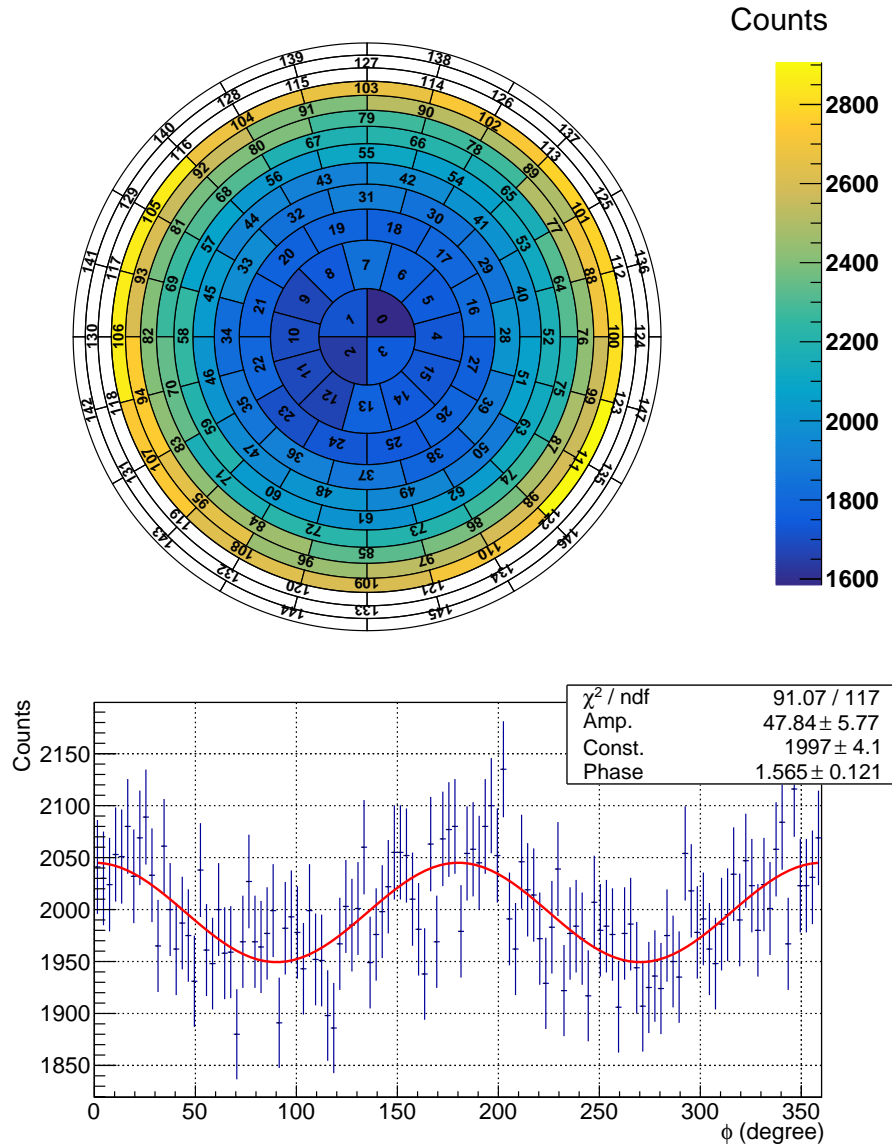


Figure 7.7.: Pixel distribution of the shifted background (upper graph) and corresponding azimuth angle distribution (lower graph). The pixel distribution of the detector seems to be radially symmetric, however, the resulting azimuth angle distribution does not seem to be compatible with isotropy. A sinusoidal function with two oscillations over 360° describes the azimuth angle distribution.

7.4. Conclusions

This chapter summarises efforts to determine the alignment between different KATRIN components. The results of the alignment studies are:

- The position of the magnetic flux tube on the detector is determined with radon rings. The centre of the flux tube is $\Delta x = (0.09 \pm 0.08)$ mm and $\Delta y = (-1.74 \pm 0.10)$ mm at the detector.
- The misalignment between the position of the retarding potential and the magnetic flux tube is quantified by projecting the inner electrode comb structure on the detector. The misalignment between these two important KATRIN components amounts to $\Delta x = (-0.16 \pm 0.11)$ mm and $\Delta y = (1.06 \pm 0.12)$ mm.
- The distribution of the spectrometer background electrons allows an alignment study of the detector relative to the centre of the main spectrometer vessel in the cylindrical sec-

tion. This misalignment amounts to $\Delta x = (-8.4 \pm 4.5)$ cm and $\Delta y = (-57.9 \pm 3.7)$ cm in the current KATRIN set-up. A quadrupole structure occurs in the azimuth angle distribution after correcting the measured background distribution for this misalignment. The quadrupole is probably of physical origin and needs to be taken into account in the KATRIN background model.

8. Summary and Outlook

KATRIN aims to achieve an unprecedented sensitivity of 0.2 eV (90 % CL) on the effective electron antineutrino mass. This thesis contributes to well characterised statistical and systematic uncertainties in the fields of rate estimation, background characterisation and component alignment.

The systematic uncertainty on the rate estimation are caused by detector read-out artefacts and physical processes (pile-up, charge-sharing and backscattering) in the detector section. By analysing data of the 2017 gaseous krypton campaign, the uncertainty in the standard analysis routine with ROI cut is shown to be between 5.89 % and 0.32 % depending on the rate range.

The rate correction factor is constant within each order of magnitude for the rate range of 10 to 10^4 cps. Therefore, the influence of detector effects can be treated as a constant inefficiency. The influence of the systematic uncertainty on rate estimation seems negligible for the neutrino mass determination.

A dependence of the background rate on the retarding potential near the endpoint of tritium presents a significant contribution to the systematic uncertainty budget of KATRIN. A statistically significant dependence ((10 ± 4) mcps/keV) or an indication ((4 ± 6) mcps/keV) is observed, depending on the magnetic field setting of the respective measurement. Consequently, the experimental findings contradict the assumption of the design report. A model which can explain the voltage dependence is proposed in this thesis: changing storage conditions of background electrons with varying retarding potential paired with a mechanism, which eliminates trapped electrons from the sensitive flux volume.

In between two background measurements a permanent increase of the background rate of 30 mcps occurred, which also results in a change of the dependence of the background rate on the retarding potential. The source of this effect needs to be examined in future works. At the moment it prohibits the calculation of final uncertainties on the neutrino mass measurement related to the background slope. As long as the source for the elevated background rate is not identified, the recommended method to treat the dependence is the inclusion as a free fit parameter in the KATRIN likelihood.

Background properties with an electric and magnetic field setting similar to the one used in future neutrino mass measurements are investigated with the data of the SDS-IIIc long-term background measurement.

A comparison of the SDS-IIIc measurement with former measurements shows an increase of 23 % in the volume-normalised rate for the flux tube of the SDS-IIIc magnetic field setting. This increase is probably explained by changed storage conditions for background electrons in the main spectrometer. An additional contribution to the background rate from ^{219}Rn emanation from the NEG material of the pre-spectrometer is likely, however further research is required to test this hypothesis.

The runs-test shows, that the time development of the measured rate is not random on small time-scales. In addition, statistical fluctuations cannot entirely explain measured

outliers to higher rates. These features cannot be explained by instabilities of the relevant hardware parameters, which fulfil the required stability criteria during the two weeks long measurement. Simultaneously stored electrons could cause both effects by ionisation of residual gas, which needs to be studied in future works.

The measured pixel distribution in the electron ROI delivers two results. First, there are indications for a damage of the detector wafer due to a former Penning discharge of the trap between the spectrometers. Second, the pixel distribution shows indications for misalignment between the spectrometer and the detector.

The alignments of the flux tube and the inner electrode system relative to the detector are determined with standard methods on recent data. The centre of the magnetic flux tube is shifted relative to the detector by (1.7 ± 0.1) mm. This can influence the mean position of the β -decay electrons at the detector.

Furthermore, a misalignment of the inner electrode system relative to the magnetic flux tube is found and determined to be (1.1 ± 0.1) mm at the detector. Consequently, the electric field might be shifted versus the magnetic flux tube, which influences the transmission properties of the main spectrometer.

A method to determine the alignment of the spectrometer vessel relative to the detector based on the measured background distribution is developed in this thesis. The effective shift of this misalignment is (58.5 ± 0.3) cm, measured in the analysing plane. Additionally, a small azimuthal component of the background distribution is found in this analysis, which is not expected in the background model.

Outlook: This thesis has determined the systematic uncertainty on rate estimation as well as the influence of a voltage dependent background on the KATRIN sensitivity. Additionally, the main spectrometer background was characterised in an electric and magnetic field setting similar to neutrino mass measurements. The misalignments of several important KATRIN components relative to the detector were quantified. Nevertheless, there are still unexplained effects, which have to be investigated in upcoming measurements.

The first tritium measurement phase of KATRIN starts in May 2018. It enables the quantification of the systematic uncertainty on rate estimation for count rates in the typical KATRIN range.

The STS-IIIa phase starts parallel to the first tritium measurements. The experimental results of measurements with the KATRIN e-gun in the course of STS-IIIa allow for an even more precise determination of the alignment of several components. Furthermore, the source of the azimuthal component of the spectrometer background can be investigated.

The first neutrino mass measurement phase of KATRIN starts at the end of 2018. The following open topics, raised by analyses performed in this thesis, have to be answered up to this point: source and optimal treatment of the voltage dependent background near the endpoint of tritium, influence of radon emanation from the NEG material of the pre-spectrometer on the background rate and identification of the source for the sudden increase of the background rate.

Appendix

A. Background in Measurements with the Condensed Krypton Source

During the krypton measurement phase in 2017, a condensed krypton source (CKrS) is used in KATRIN for calibration measurements. The CKrS is placed in the CPS. Consequently, krypton atoms, which escape from the source, can enter the pre-spectrometer, as no further reduction mechanisms against neutral particles exist between the CPS and the spectrometer section. Therefore, it is possible to examine the influence of radioactive atoms in the spectrometer section on the background rate with the data of the CKrS. The goal of this chapter is to quantify the influence of the CKrS on the background rate and to examine the stability of the rate.

Chapter A.1 summarises the most important properties of the CKrS for this study. In chapter A.2 the background caused by the CKrS while it is inserted in the beamline is investigated in detail. Afterwards, chapter A.3 presents the background rate of the CKrS over long time scales. The last chapter A.4 summarises investigations of the behaviour of the background after the extraction of the CKrS from the beamline.

A.1. The Condensed Krypton Source

The decay mechanism of $^{83\text{m}}\text{Kr}$ and its application purposes are described in 3.1. The CKrS consists of a graphite substrate with a diameter of 2 cm, which is cooled to 26 K. A thin sub-monolayer film of $^{83\text{m}}\text{Kr}$ is placed on this substrate. ^{83}Rb is implanted into a foil and placed in vacuum. Gaseous $^{83\text{m}}\text{Kr}$ is emanated from the foil, purified by a cold trap and quench-condensed on the graphite substrate [KAT05] [KAT18a].

The CKrS features high, stable and localised count rates, which can be used to scan the beamline precisely and within short time. The major disadvantage of the CKrS is the reproducibility of the source. A shift of the line position with a new $^{83\text{m}}\text{Kr}$ film on the substrate is possible [KAT05]. The properties of the current film can be checked by a laser ellipsometry system [BGS⁺13]. Three different films were used in the krypton measurement phase in 2017.

A.2. Background Rate with Injected CKrS

This chapter quantifies the influence of the CKrS on the background, while the source is in the beamline and during its extraction. The runs 33339, 333497 and 33524 are investigated in more detail.

There are collisions of the flux tube with the spectrometer vessel in the magnetic field setting, which is used during the condensed $^{83\text{m}}\text{Kr}$ campaign. Secondary electrons therefore dominate the measured rate in the corresponding detector pixels. Hence, the two outermost detector rings are excluded for the subsequent analyses. Two ROI cuts are applied in the following analyses: the standard ROI as described in chapter 2.3 and one for the direct transition of excited krypton to ground state. The corresponding electron peak is expected at 41 keV minus the binding energy of the electron in the shell and minor corrections. The post-acceleration electrode of the detector is set to its nominal value of 10 kV, therefore

this ROI ranges from 48 keV to 53 keV. This ROI will be called ROI41 in the following. Two background runs were taken prior to the injection of any tritium. The background rate in the electron ROI without any krypton is (481 ± 8) mcps, in the ROI41 it is (12 ± 1) mcps.

The retarding potential in the main spectrometer is set to 33 keV to investigate the background rate, while the CKrS is inserted in the beamline. This is the so-called “blocking mode”, since at this retarding potential the two conversion lines at approximately 9 keV and 32 keV are both blocked. The measured rate at this retarding potential is due to background electrons induced by the CKrS and due to a direct decay of excited krypton to its ground state.

The main spectrometer is set to blocking mode during run 33497. Figure A.1 shows several properties of this run. The measured energy distribution contains two characteristic peaks P1 and P2. P1 corresponds to the expected background electron peak at approximately 43 keV. P2 is caused by conversion electrons of the direct krypton decay.

The graph in the upper centre of figure A.1 shows the pixel distribution in the electron ROI. The measured electrons are focused at the bulls-eye of the detector. The pixel distribution without any krypton shows a minima of the rate at the bulls-eye and an increasing rate with the detector radius. Hence, the hotspot of the rate at the centre of the detector is a direct impact of the CKrS on the background electrons. The inter-arrival time distribution (see lower left graph of figure A.1) follows an exponential function with $p = 64\%$. This behaviour indicates a Poissonian rate in the electron ROI. The rate of the electrons is increasing versus time from 12.5 cps to 15.5 cps (see lower centre graph).

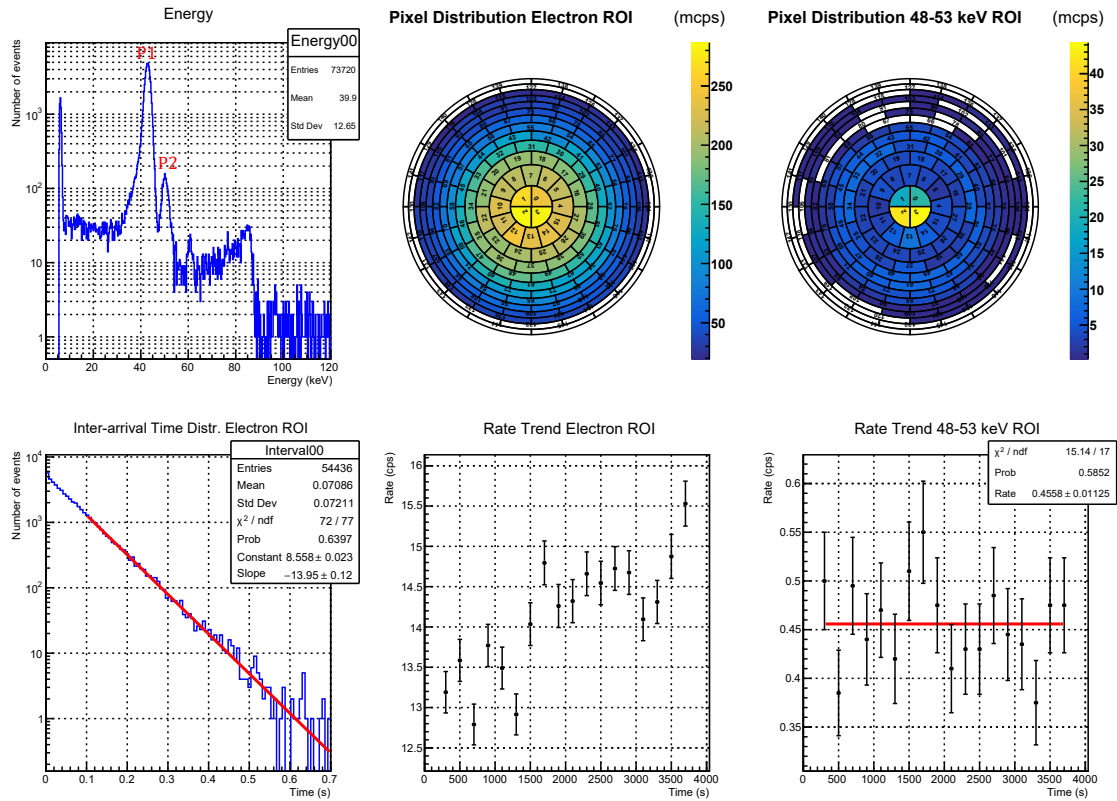


Figure A.1.: Overview plots for run 33497. In the upper left graph, the measured energy distribution is shown. The graphs in the upper centre and right display the pixel distribution in the electron ROI, respectively in the ROI41. The lower left graph presents inter-arrival time distribution, which is fitted by an exponential function. In the plots in the lower centre and right, the rate trend versus time for the electron ROI and the ROI41 are shown.

be drawn. First, the background rate in the electron ROI is elevated due to the CKrS by approximately two orders of magnitude in comparison to the reference runs without any krypton source. The elevation is mainly caused at the centre of the bulls-eye, which corresponds to the magnetic main axis of the spectrometer. Single krypton atoms can leave the CKrS due to out-gassing effects and enter the spectrometer section. During the likely decay of krypton in the spectrometer section, a high-energy conversion electron ($E_{\text{kin}} > 9 \text{ keV}$) is emitted. The conversion electron is with high probability trapped in the magnetic bottle. However, it goes through a cooling-down process and produces secondary electrons. The best storage conditions for a trapped electron are near the magnetic main axis of the spectrometer. Hence, also the secondary electrons are mainly produced near the main axis. This explains the surplus of events at the bulls-eye of the detector. The second conclusion is, that the background rate seems to increase with time. A more detailed investigation of the long-term temporal behaviour of the background rate is discussed in chapter A.3.

The upper right graph of figure A.1 shows the pixel distribution in the ROI41keV. A surplus of measured events forms a clearly defined hotspot in the bulls-eye, which is the projection of the CKrS on the detector. This indicates, that the ROI41keV is dominated by conversion electrons of the direct decay of the $I^P = 1/2^-$ -state of the $^{83\text{m}}\text{Kr}$ to the ground state. The rate in this ROI is constant at approximately $(456 \pm 11) \text{ mcps}$ (see lower right graph of figure A.1). The peak position of the ROI41keV is fitted to $(50.28 \pm 0.04) \text{ keV}$. This corresponds to an electron energy of $(40.16 \pm 0.04) \text{ keV}$. This value is in accordance with the expected conversion line energy for the direct krypton decay.

Run 33524 was taken approximately one day after the previously analysed run 33497. The CKrS was in full operating mode during these two runs. The spectrometer was set to blocking mode for the measurements during run 33524. The mean rate in the electron ROI is estimated to $(14.67 \pm 0.06) \text{ cps}$. Hence, the rate is statistically significant elevated in comparison to run 33497 ($(13.81 \pm 0.06) \text{ cps}$). There seems to be a connection between the

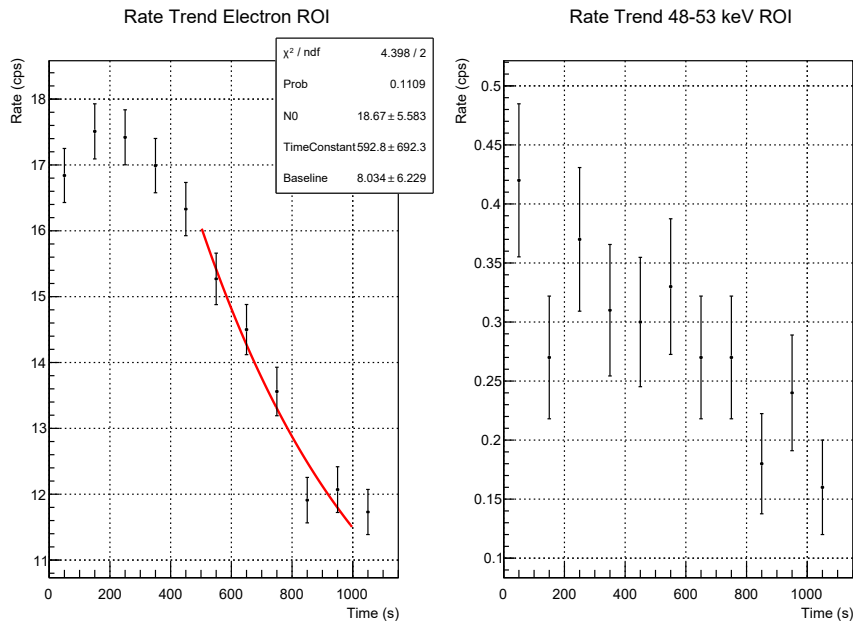


Figure A.2.: Rate versus time for both ROI during the extraction of the CKrS from the beamline. Both rate trends show a decline in the rate with time. This decline is fitted with an exponential function in the electron ROI. The fit results in a half-life of $(6 \pm 8) \text{ min}$.

background rate and the time, how long the CKrS is injected in the beamline.

It is expected, that the rate in the ROI41keV of run 33524 is the same as run 33497. The activity of the CKrS is assumed to be constant over such time ranges. The ROI41keV rate in run 33524 is (469 ± 11) mcps, which is in accordance with run 33497.

Figure A.2 displays the measured rate versus time for both ROIs for run 33582. The CKrS is extracted from the beamline during this run.

At the beginning of the run, the rate in the electron ROI is determined to approximately 17 cps. Hence, the rate is again elevated in comparison to 33524. The CKrS is extracted from the beamline at approximately 300 s after the start of the run. Afterwards, the rate decreases with an exponential shape. The decrease has a half-life of (6 ± 8) min. The fast decrease of the rate is likely due to the active pumping of the spectrometer, which removes krypton atoms from the spectrometers volume.

The rate in the ROI41keV also shows a decrease versus time. The shape of the decrease cannot be described further due to large statistical uncertainties.

Three conclusions are drawn in this chapter. First, an electron conversion line of the direct krypton decay to the ground state is seen. The measured electron energy of the conversion line is approximately (40.16 ± 0.04) keV. Second, the background rate in the electron ROI is elevated by two orders of magnitude in comparison to reference runs without the CKrS. The background rate is focused on the bulls-eye of the detector. Third, it seems that the background rate is increasing over the time, in which the CKrS is inserted in the beamline. The following chapter investigates the background rate over longer time scales.

A.3. Long-term Background Investigation

The behaviour of the background rate versus time is investigated by two different approaches. The first approach investigates the background rate in four different runs, in which the main spectrometer is set to blocking mode. The second approach tries to investigate the background rate in line scans of the $L_3 - 9.4$ conversion line.

The four different background runs 33339, 33497, 33524 and 33582 are investigated for the following analysis. Run 33339 was taken 15 min after the injection of the CKrS, 33497 after three days, 33524 after four days and 33582 after five days. The analysis uses only the first 300 s of run 33582, since the CKrS is extracted during the run.

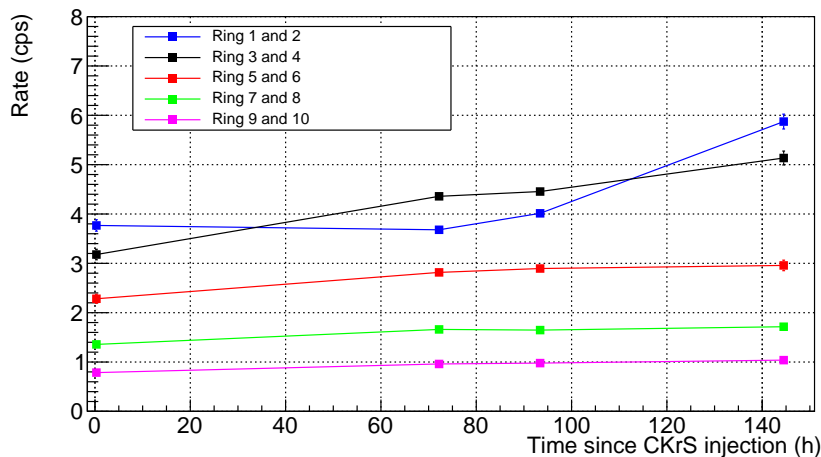


Figure A.3.: Ring-wise background rate versus time. All rings measure an increasing rate with time. The growth of the rate increases with decreasing detector radius.

Figure A.3 presents the ring-wise background rate versus time. The rate of all rings increases versus time. The growth of the rate increases towards the inner detector rings, which indicates a causality with the CKrS. As shown in A.2, the background caused by the CKrS is focused at the centre of the detector. Therefore a temporal effect of the CKrS on the background rate is expected to be focused at the centre of the detector. However, the validity of this analysis is limited due to low statistics. Line scans of the $L_3 - 9.4$ conversion line enable another approach.

Several line scans of the $L_3 - 9.4$ conversion line were taken during the CKrS campaign. Only one ^{83m}Kr film was used on the substrate of the CKrS during the last three days. In the last three days of the campaign, nine $L_3 - 9.4$ line scans were performed. Hence, the line position and rate can be assumed stable for these nine line scans. The conversion electrons of the CKrS are focused on the bulls-eye of the detector [KAT18a]. This might enable an analysis of the background rate for the last three days with the rate, which is measured in the outer detector rings.

Therefore it needs to be tested, if the rate of the four innermost detector rings is independent of the rate in the outer detector rings. Hence, a correlation analysis is performed of the four innermost detector rings with the detector rings 5-11. The vanishing correlation factor $\rho = -0.09$ indicates an independence of the rate measured in the two detector areas. An investigation of the background rate with the detector rings 5-11 is allowed.

However, the rate measured in these detector rings shows a constant behaviour versus time. Consequently, the temporal dependent background rate induced by the CKrS is focused on the four innermost detector rings. This is also indicated by the plot in figure A.3.

In summary, it is shown that the background rate caused by the CKrS increases with time. The increase is quantified to approximately 1.2 cps/day. This increase of the rate is focused on the four innermost rings of the detector.

A.4. Background after Extraction of CKrS

This chapter characterises the behaviour of the background after the extraction of the CKrS from the beamline. The runs 33300 up to 33311 are therefore investigated in more detail. These runs contain 12 h of measurement directly after the source extraction.

Figure A.4 shows the behaviour of the background in the first two hours after the extraction of the CKrS. The peak due to background electrons is measured at the expected position in the energy distribution (see upper left graph of figure A.4). However, the energy distribution shows also a peak in the ROI41keV despite the absence of the CKrS. This indicates remaining krypton in the beamline.

The pixel distribution in the electron ROI shows, that the background rate is focused on the bullseye of the detector. This surplus of rate at the centre is assumed to be caused by trapped conversion electrons of krypton decay (see chapter A.2). The storage time of trapped electrons can range up to several hours [MDF⁺13]. Thus, the pixel distribution is reasonable. The rate in the electron ROI is exponentially decreasing versus time in the first 2500 s of the run. The half-life of this decrease is (8 ± 1) min, which is likely to be related to the active pumping of the spectrometer section [Frä17c]. Out-gassed krypton atoms, which are in the spectrometer section, are actively pumped out of the spectrometer volume. Hence, the number of possible sources of background decreases, resulting in the decreasing rate. The decrease of the rate due to the active pump-out is dominant in the first 2500 s, afterwards another effect seems to dominate the rate. At that point, it can be assumed, that the major part of krypton atoms in the spectrometer is already pumped out of the active volume. The rate versus time after the 2500 s seems to follow another half-life. To summarise, there are two effects which cause a decrease of the rate versus time, which both have a different dependence on the time. These two effects lead to a deviation of the

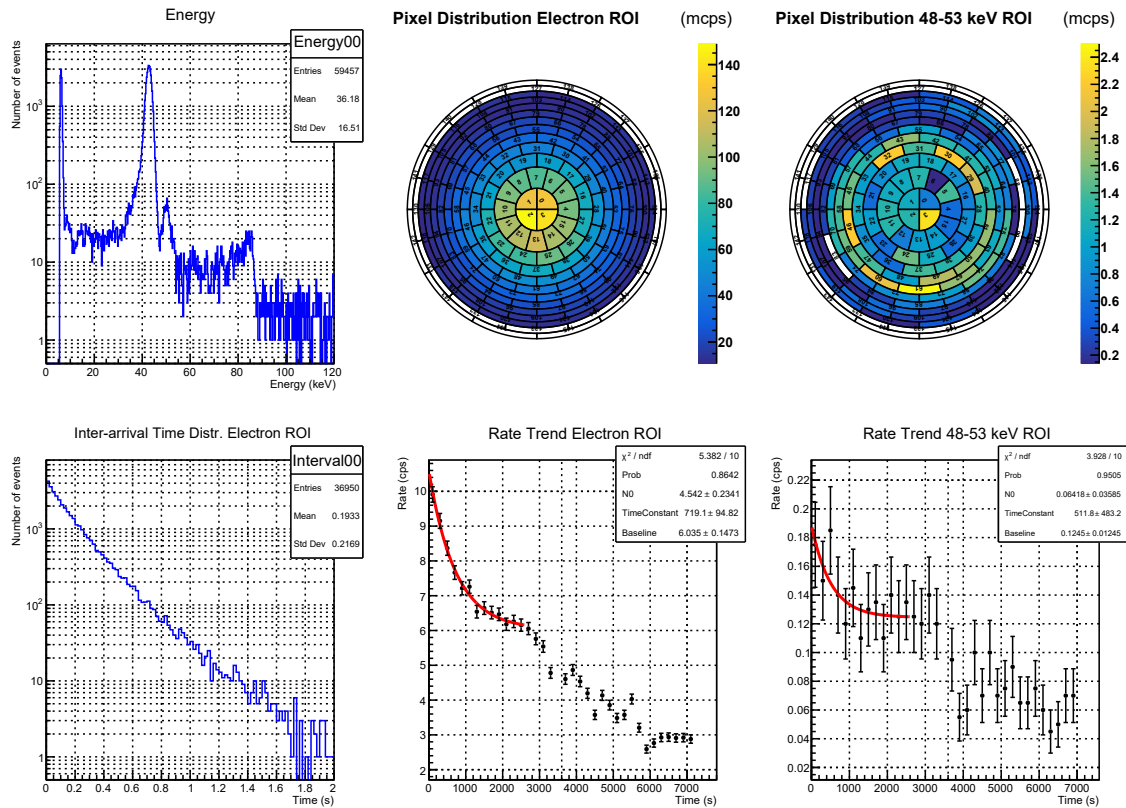


Figure A.4.: Behaviour of background in the first two hours after the extraction of the CKrS. The measured energy distribution contains the two peaks of the electron ROI and ROI41 keV (upper left). The graph in the upper centre shows the electron background distribution, which is focused at the centre of the detector. The pixel distribution of the ROI41keV does not show a clear trend, which is likely due to non-adiabatic effects (upper right). The inter-arrival time distribution does not follow a logarithmic function (lower left). The rate trend graphs for both ROI display an exponential decrease of the rate (lower centre and lower right).

expected exponential behaviour in the inter-arrival time distribution (see lower left graph). The pixel distribution in the ROI41keV shows several pixels with elevated rate (see upper right graph of figure A.4). The highlighted pixels are not only at the bulls-eye of the detector, but more randomly distributed over the whole detector. This pixel distribution might be caused by non-adiabatic effects. The high-energy conversion electrons of the direct krypton decay are not adiabatically guided by the magnetic field lines to the detector, resulting in this smeared pixel distribution. The rate trend graph in the ROI41keV (see lower right graph) shows a similar behaviour as the rate trend in the electron ROI. At first, an exponential decay of the rate is shown with a half-life of (6 ± 5) min. This decay is related to the active pump-out of the spectrometer, due to the time structure. After approximately 2500 s, another effect with a different time structure becomes dominant. This effect is examined in the following with the background runs 33302-33311.

Figure A.5 presents the overview plots for the run 33302-33311. Run 33302 starts two hours after the extraction of the CKrS, run 33311 ends 12 hours after its extraction. The measured energy distribution shows the electron background peak at approximately 42 keV, as expected. The peak due to direct krypton decay at 51 keV is only vaguely visible. The pixel distribution in the electron ROI shows the familiar hotspot of the rate at the bulls-eye. This points towards the presence of high-energy trapped conversion electrons. Consequently, krypton atoms might still be in the beamline, even after two hours of the

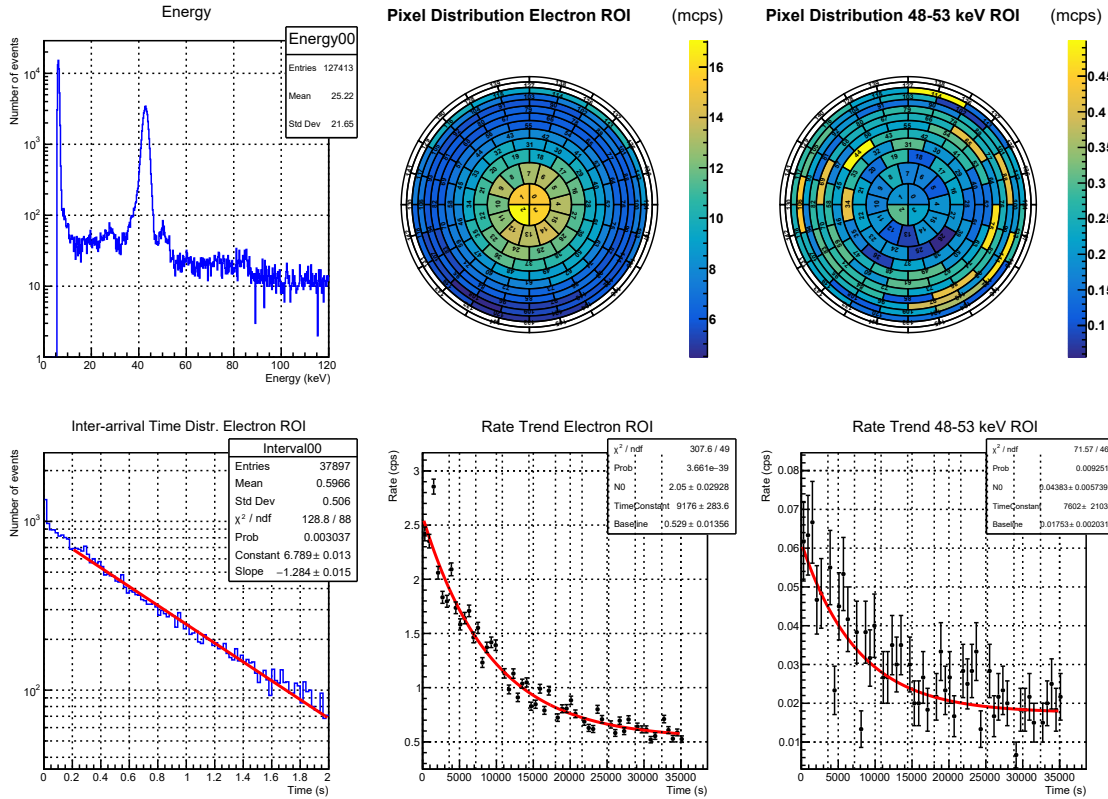


Figure A.5.: Overview plots for run 33302-33311 (2-11 hours after extraction of CkR_S from the beamline). The electron background peak is clearly visible in the measured energy distribution (upper left graph). The peak of direct decay is not clearly shown anymore. The pixel distribution in the electron ROI is focused at the bulls-eye of the detector (upper centre graph), whereas in the ROI41keV it is quite diffuse (upper right graph). The inter-arrival time distribution follows an exponential function (lower left graph). Both rate trend graphs show an exponential decrease of the rate (lower centre and right lower).

extraction of the CkR_S. The rate trend graph for the electron ROI confirms this hypothesis. The rate decreases exponentially with time. The fitted exponential curve results in an half-life of (1.76 ± 0.05) h, which is in accordance with the half-life of $^{83\text{m}}\text{Kr}$. A ring-wise analysis of the rate proves, that the decrease of the total rate is mainly due to a decrease in the inner detector rings. This is expected in case of remaining krypton, as krypton induced background is focused at the bulls-eye of the detector. Consequently, $^{83\text{m}}\text{Kr}$ is still in the beamline. The spectrometer section is excluded as place of the remaining krypton, as it is actively pumped. A krypton reservoir in the CPS is proposed in [Frä17c]. The baseline of the fit results in (529 ± 13) mcp/s, which is near the reference value of (481 ± 8) mcp/s without krypton. Consequently, it is expected that the background rate decreases to its nominal value.

The pixel distribution in the ROI41keV is diffuse due to non-adiabatic effects. The corresponding rate decreases exponentially versus time. The half-life is determined with a fit to (1.5 ± 0.4) h. The fitted half-life is therefore also in accordance with the half-life of krypton. This underlines the hypothesis of a krypton reservoir inside the beamline. The baseline of the fit is determined to (17 ± 2) mcp/s. Therefore it is also expected, that the background rate in this ROI decreases also to its nominal value.

A.5. Conclusions

The background rate in the electron ROI increases by two orders of magnitude due to the injection of the CKrS in the beamline. The additional background is caused by the propagation of out-gassed krypton atoms to the sensitive volumes of the spectrometer. The emitted conversion electrons, which accompany the decay of krypton, are trapped by the magnetic mirror and produce secondary electrons near the magnetic main axis of the spectrometer. The background induced by the CKrS is therefore focused at the bulls-eye of the detector.

Chapter A.3 shows, that the background rate is increasing with the time the CKrS is injected in the beamline. This increase is only seen in the inner four detector rings.

The rate decreases exponentially versus time after the extraction of the CKrS from the beamline. First, this decay follows a half-life in $\mathcal{O}(\text{min})$. This is due to pump-out of remaining krypton atoms from the spectrometer volume. The half-life of this decay changes after approximately one hour. The following decay has a half-life, which is in accordance with the half-life of $^{83\text{m}}\text{Kr}$. This decay indicates a krypton reservoir in the CPS. Due to the fitted baseline of the decay, it is assumed, that the background rate in the spectrometer section decreases to its nominal value.

A peak is measured, which is related to the direct decay of krypton from the $I^P = 1/2^-$ -state to the ground state. The fitted peak corresponds to an initial electron energy of (40.16 ± 0.04) keV.

B. KATRIN Numbers of Slow-Control Parameters

Table B.1.: Slow-control parameter and the corresponding KATRIN numbers. The first column lists the measured quantities. The exact sensor position is shown in the second column. The third column gives the corresponding KATRIN number, which can be used for further analysis by Kasper. A complete list of slow-control parameters is given in <http://katrin.kit.edu/katrin/kdb-admin.fcgi/sensors/>.

Parameter	Position Sensor	KATRIN Number
Magnetic field analysing plane (T)	Mid-Ring 9	433-RBY-1-7350-0003
	Mid-Ring 23	433-RBY-1-7310-0003
	Mid-Ring 30	433-RBY-1-7320-0003
Retarding voltage (V)	K-35	436-REU-0-0201-0001
MS temperature ($^{\circ}$ C)	Vessel	435-RTP-5-0075-0001
FPD temperature ($^{\circ}$ C)	Carousel	527-RTP-6-1285-0001
Vacuum pressure (mbar)	Extractor ion gauge	432-RPI-3-1110-0001
Baffle 1 temperature (K)	Top	435-RTP-5-1080-0001
	Bottom	435-RTP-5-1081-0001
	Center	435-RTP-5-1082-0001
	Inlet	435-RTP-5-1083-0001
Baffle 2 temperature (K)	Top	435-RTP-5-2080-0001
	Bottom	435-RTP-5-2081-0001
	Center	435-RTP-5-2082-0001
	Inlet	435-RTP-5-2083-0001
Baffle 3 temperature (K)	Top	435-RTP-5-3080-0001
	Bottom	435-RTP-5-3081-0001
	Center	435-RTP-5-3082-0001
	Inlet	435-RTP-5-3083-0001

Bibliography

- [AAA⁺89] Akrawy, MZ, G Alexander, J Allison, PP Allport, KJ Anderson, JC Armitage, GTJ Arnison, P Ashton, G Azuelos, JTM Baines, *et al.*: *Measurement of the Z0 Mass and Width with the OPAL Detector at LEP*. Physics Letters B, 231(4):530–538, 1989.
- [AAA⁺02] Ahmad, Q Retal, RC Allen, TC Andersen, JD Anglin, JC Barton, EW Beier, M Bercovitch, J Bigu, SD Biller, RA Black, *et al.*: *Direct evidence for neutrino flavor transformation from neutral-current interactions in the Sudbury Neutrino Observatory*. Physical review letters, 89(1):011301, 2002.
- [AAA⁺14] Abgrall, N, Estanislao Aguayo, Frank T Avignone, Alexander S Barabash, FE Bertrand, M Boswell, V Brudanin, Matthew Busch, AS Caldwell, Y D Chan, *et al.*: *The majorana demonstrator neutrinoless double-beta decay experiment*. Advances in High Energy Physics, 2014, 2014.
- [AAA⁺16] An, Fengpeng, Guangpeng An, Qi An, Vito Antonelli, Eric Baussan, John Beacom, Leonid Bezrukov, Simon Blyth, Riccardo Brugnera, Margherita Buizza Avanzini, *et al.*: *Neutrino physics with JUNO*. Journal of Physics G: Nuclear and Particle Physics, 43(3):030401, 2016.
- [ABB⁺11] Aseev, V.N., A.I. Belev, A.I. Berlev, E.V. Geraskin, A.A. Golubev, N.A. Likhovid, V.M. Lobashev, A.A. Nozik, V.S. Pantuev, V.I. Parfenov, A.K. Skasyrskaya, F.V. Tkachov, and S.V. Zadorozhny: *Upper limit on the electron antineutrino mass from the Troitsk experiment*. Physical Review D, 84:112003, 2011.
- [ABB⁺15] Amsbaugh, J.F., J. Barrett, A. Beglarian, T. Bergmann, H. Bichsel, L.I. Bodine, J. Bonn, N.M. Boyd, T.H. Burritt, Z. Chaoui, S. Chilingaryan, T.J. Corona, P.J. Doe, J.A. Dunmore, S. Enomoto, J. Fischer, J.A. Formaggio, F.M. Fränkle, D. Furse, H. Gemmeke, F. Glück, F. Harms, G.C. Harper, J. Hartmann, M.A. Howe, A. Kaboth, J. Kelsey, M. Knauer, A. Kopmann, M.L. Leber, E.L. Martin, K.J. Middleman, A.W. Myers, N.S. Oblath, D.S. Parno, D.A. Peterson, L. Petzold, D.G. Phillips II, P. Renschler, R.G.H. Robertson, J. Schwarz, M. Steidl, D. Tcherniakhovski, T. Thümmler, T.D. Van Wechel, B.A. VanDevender, S. Vöcking, B.L. Wall, K. L. Wierman, J.F. Wilkerson, and S. Wüstling: *Focal-plane detector system for the KATRIN experiment*. Nuclear Instruments and Methods in Physics Research Section A: Accelerators, Spectrometers, Detectors and Associated Equipment, 778:40–60, 2015.
- [Abe08] Abe, S. et al. (KamLAND Collaboration): *Precision Measurement of Neutrino Oscillation Parameters with KamLAND*. Physical Review Letters, 100:221803, 2008.
- [Abe12] Abe, Y. et al. (Double Chooz Collaboration): *Reactor $\bar{\nu}_e$ disappearance in the Double Chooz experiment*. Physical Review D, 86:052008, 2012.

- [Ada13] Adamson, P. et al. (MINOS Collaboration): *Measurement of Neutrino and Antineutrino Oscillations Using Beam and Atmospheric Data in MINOS*. Physical Review Letters, 110:251801, 2013.
- [Ade14] Ade, P. et al. (Planck Collaboration): *Planck 2013 results. XVI. Cosmological parameters*. Astronomy and Astrophysics, 571:66, 2014.
- [Ago13] Agostini, M. et al. (GERDA Collaboration): *Results on Neutrinoless Double- β Decay of ^{76}Ge from Phase I of the GERDA Experiment*. Physical Review Letters, 111:122503, 2013.
- [Aha13] Aharmim, B. et al. (SNO Collaboration): *Combined analysis of all three phases of solar neutrino data from the Sudbury Neutrino Observatory*. Physical Review C, 88:025501, 2013.
- [AHH⁺92] Anselmann, P, W Hampel, G Heusser, J Kiko, T Kirsten, E Pernicka, R Plaga, U Rönn, M Sann, C Schlosser, et al.: *Solar neutrinos observed by GALLEX at Gran Sasso*. Physics Letters B, 285(4):376–389, 1992.
- [AHH⁺94] Anselmann, P, W Hampel, G Heusser, J Kiko, T Kirsten, M Laubenstein, E Pernicka, S Pezzoni, U Rönn, M Sann, et al.: *GALLEX results from the first 30 solar neutrino runs*. Physics Letters B, 327(3-4):377–385, 1994.
- [Ahn12] Ahn, J. K. et al. (RENO Collaboration): *Observation of Reactor Electron Antineutrinos Disappearance in the RENO Experiment*. Physical Review Letters, 108:191802, 2012.
- [An,12] An, F. P. et al. (Daya Bay Collaboration): *Observation of Electron-Antineutrino Disappearance at Daya Bay*. Physical Review Letters, 108:171803, 2012.
- [And11] Andreotti, E. et al. (CUORICINO collaboration): *^{130}Te neutrinoless double-beta decay with CUORICINO*. Astroparticle Physics, 34(11):822–831, 2011.
- [B⁺10] Beck, Marcus et al.: *The KATRIN experiment*. In *Journal of Physics: Conference Series*, volume 203, page 012097. IOP Publishing, 2010.
- [Bah94] Bahcall, John N: *Two solar neutrino problems*. Physics Letters B, 338(2-3):276–281, 1994.
- [BAL] BALLARD, D.H.: *{GENERALIZING} {THE} {HOUGH} {TRANSFORM} {TO} {DETECT} {ARBITRARY} SHAPES**.
- [Bas14] Basunia, M. Shamsuzzoha: *Nuclear Data Sheets for $A = 210$* . Nuclear Data Sheets, 121:561 – 694, 2014, ISSN 0090-3752. <http://www.sciencedirect.com/science/article/pii/S0090375214006589>.
- [BBB⁺87] Bionta, R. M., G. Blewitt, C. B. Bratton, D. Casper, A. Ciocio, R. Claus, B. Cortez, M. Crouch, S. T. Dye, S. Errede, G. W. Foster, W. Gajewski, K. S. Ganezer, M. Goldhaber, T. J. Haines, T. W. Jones, D. Kielczewska, W. R. Kropp, J. G. Learned, J. M. LoSecco, J. Matthews, R. Miller, M. S. Mudan, H. S. Park, L. R. Price, F. Reines, J. Schultz, S. Seidel, E. Shumard, D. Sinclair, H. W. Sobel, J. L. Stone, L. R. Sulak, R. Svoboda, G. Thornton, J. C. van der Velde, and C. Wuest: *Observation of a neutrino burst in coincidence with supernova 1987A in the Large Magellanic Cloud*. Phys. Rev. Lett., 58:1494–1496, Apr 1987. <https://link.aps.org/doi/10.1103/PhysRevLett.58.1494>.
- [BBB⁺12] Babutzka, M., M. Bahr, J. Bonn, B. Bornschein, A. Dieter, G. Drexlin, K. Eitel, S. Fischer, F. Glück, S. Grohmann, M. Hötzel, T.M. James, W. Käfer,

- M. Leber, B. Monreal, F. Priester, M. Röllig, M. Schlösser, U. Schmitt, F. Sharipov, M. Steidl, M. Sturm, H.H. Telle, and N. Titov: *Monitoring of the operating parameters of the KATRIN Windowless Gaseous Tritium Source*. New Journal of Physics, 14(10):103046, 2012.
- [BBC⁺11] Babutzka, M, J Barrett, TJ Corona, J Formaggio, D Furse, *et al.*: *The comprehensive guide to KASSIOPEIA*, 2011.
- [BBD⁺99] Bonn, J, L Bornschein, B Degen, EW Otten, and Ch Weinheimer: *A high resolution electrostatic time-of-flight spectrometer with adiabatic magnetic collimation*. Nuclear Instruments and Methods in Physics Research Section A: Accelerators, Spectrometers, Detectors and Associated Equipment, 421(1):256–265, 1999.
- [BBG⁺96] Bennett, Charles L, Anthony J Banday, Krzysztof M Górski, G Hinshaw, P Jackson, P Keegstra, A Kogut, George F Smoot, David T Wilkinson, and Edward L Wright: *Four-year COBE* DMR cosmic microwave background observations: maps and basic results*. The Astrophysical Journal Letters, 464(1):L1, 1996.
- [Beh17] Behrens, J.: *Sensitivity calculations for 70% beamline fields*, 2017. <https://neutrino.ikp.kit.edu:8080/SDS-Measurements+Phase+3/62>.
- [Ben15] Benato, Giovanni: *Effective Majorana mass and neutrinoless double beta decay*. The European Physical Journal C, 75(11):563, Nov 2015, ISSN 1434-6052. <https://doi.org/10.1140/epjc/s10052-015-3802-1>.
- [BGS⁺13] Bauer, S., B. Grees, D. Spitzer, M. Beck, R. Bottesch, H. W. Ortjohann, B. Ostrick, T. Schäfer, H. H. Telle, A. Wegmann, M. Zbořil, and C. Weinheimer: *Ellipsometry with polarisation analysis at cryogenic temperatures inside a vacuum chamber*. Review of Scientific Instruments, 84(12):123103, 2013. <https://doi.org/10.1063/1.4838555>.
- [BHH⁺03] Bennett, Charles L, M Halpern, G Hinshaw, N Jarosik, A Kogut, M Limon, SS Meyer, L Page, DN Spergel, GS Tucker, *et al.*: *First-Year Wilkinson Microwave Anisotropy Probe (WMAP)* Observations: Preliminary Maps and Basic Results*. The Astrophysical Journal Supplement Series, 148(1):1, 2003.
- [Bla06] Blaum, Klaus: *High-accuracy mass spectrometry with stored ions*. Physics Reports, 425(1):1–78, 2006.
- [BP34] Bethe, Hans and Rudolph Peierls: *The 'neutrino'*. Nature, 133(3362):532, 1934.
- [BPT80] Beamson, G., H.Q. Porter, and D.W. Turner: *The collimating and magnifying properties of a superconducting field photoelectron spectrometer*. Journal of Physics E: Scientific Instruments, 13(1):64, 1980.
- [Bro05] Browne, E.: *Nuclear Data Sheets for A=212*. Nuclear Data Sheets, 104(2):427 – 496, 2005, ISSN 0090-3752. <http://www.sciencedirect.com/science/article/pii/S0090375205000037>.
- [CDE18] Canright, Jared, Peter Doe, and Sanshiro Enomoto: *Performance of the New Detector Veto and SDS3-Christmas Muon Analysis*, 2018. https://fuzzy.fzk.de/bscw/bscw.cgi/1196899?op=preview&back_url=1196694.
- [Cen18] Center), (National Nuclear Data: *NuDat (Nuclear Structure and Decay Data*, 2018. <http://www.nndc.bnl.gov/nudat2/>.
- [CFKS09] Cycon, Hans L, Richard G Froese, Werner Kirsch, and Barry Simon: *Schrödinger operators: With application to quantum mechanics and global geometry*. Springer, 2009.

- [CGR06] Choi, J. H., J. R. Guest, and G. Raithel: *Magnetic trapping of strongly-magnetized Rydberg atoms*. The European Physical Journal D - Atomic, Molecular, Optical and Plasma Physics, 40(1):19–26, Oct 2006, ISSN 1434-6079. <https://doi.org/10.1140/epjd/e2006-00086-2>.
- [Cha14] Chadwick, J: *Intensitätsverteilung im magnetischen Spectrum der β -Strahlen von radium B + C*. Verhandl. Dtsch. Phys. Ges., 16:383, 1914. <http://cds.cern.ch/record/262756>.
- [Che85] Chen, Herbert H: *Direct approach to resolve the solar-neutrino problem*. Physical Review Letters, 55(14):1534, 1985.
- [Cow88] Cowsik, R: *Neutrino masses and flavors emitted in the supernova SN1987A*. Physical Review D, 37(6):1685, 1988.
- [Cra12] Crasemann, Bernd: *Atomic inner-shell processes*. Elsevier, 2012.
- [DGG⁺62] Danby, G., J M. Gaillard, K. Goulianos, L. M. Lederman, N. Mistry, M. Schwartz, and J. Steinberger: *Observation of High-Energy Neutrino Reactions and the Existence of Two Kinds of Neutrinos*. Phys. Rev. Lett., 9:36–44, Jul 1962. <https://link.aps.org/doi/10.1103/PhysRevLett.9.36>.
- [DHMW13] Drexlin, G., V. Hannen, S. Mertens, and C. Weinheimer: *Current Direct Neutrino Mass Experiments*. Advances in High Energy Physics, 2013, 2013.
- [Dre05] Drexlin, Guido et. al. (Katrin Collaboration): *KATRIN-direct measurement of a sub-eV neutrino mass*. Nuclear Physics B-Proceedings Supplements, 145:263–267, 2005.
- [DTSJ06] Doss, Natasha, Jonathan Tennyson, Alejandro Saenz, and Svante Jonsell: *Molecular effects in investigations of tritium molecule β decay endpoint experiments*. Physical Review C, 73(2):025502, 2006.
- [EBB⁺18] Erhard, M., J. Behrens, S. Bauer, A. Beglarian, R. Berendes, G. Drexlin, F. Glück, R. Gumbsheimer, J. Hergenhan, B. Leiber, S. Mertens, A. Osipowicz, P. Plischke, J. Reich, T. Thümmeler, N. Wandkowsky, C. Weinheimer, and S. Wüstling: *Technical design and commissioning of the KATRIN large-volume air coil system*. Journal of Instrumentation, 13(02):P02003, 2018. <http://stacks.iop.org/1748-0221/13/i=02/a=P02003>.
- [Eno17] Enomoto, Sanshiro: *Persönliche Korrespondenz*. 2017.
- [FB18] Fränkle, Florian and Fabian Block: *background dependence on the retarding potential*. internal KATRIN elog [online], 2018. <https://neutrino.ikp.kit.edu:8080/SDS-Measurements+Phase+3/68>.
- [FBD⁺11] Fränkle, F.M., L. Bornschein, G. Drexlin, F. Glück, S. Görhardt, W. Käfer, S. Mertens, N. Wandkowsky, and J. Wolf: *Radon induced background processes in the KATRIN pre-spectrometer*. Astroparticle Physics, 35(3):128 – 134, 2011, ISSN 0927-6505. <http://www.sciencedirect.com/science/article/pii/S0927650511001290>.
- [FBH⁺16] Fränkle, F. M., L. Bornschein, F. Harms, J. Wolf, P. Ranitzsch, T. Thümmeler, and N. Trost: *Contamination of main spectrometer with ^{212}Pb* . internal KATRIN elog [online], 2016. <https://neutrino.ikp.kit.edu:8080/SDS-Measurements+Phase+3/17>.
- [Fel85] Felsenstein, Joseph: *Confidence limits on phylogenies: an approach using the bootstrap*. Evolution, 39(4):783–791, 1985.

- [Fer34] Fermi, E.: *Versuch einer Theorie der β -Strahlen*. Zeitschrift für Physik, 88(3–4):161–177, 1934.
- [FFH⁺03] Fukuda, S, Y Fukuda, T Hayakawa, E Ichihara, M Ishitsuka, Y Itow, T Kajita, J Kameda, K Kaneyuki, S Kasuga, *et al.*: *The super-kamiokande detector*. Nuclear Instruments and Methods in Physics Research Section A: Accelerators, Spectrometers, Detectors and Associated Equipment, 501(2-3):418–462, 2003.
- [FGV⁺14] Fränkle, F.M., F. Glück, K. Valerius, K. Bokeloh, A. Beglarian, J. Bonn, L. Bornschein, G. Drexlin, F. Habermehl, M.L. Leber, A. Osipowicz, E.W. Otten, M. Steidl, T. Thümmel, C. Weinheimer, J.F. Wilkerson, J. Wolf, and S.V. Zadorozhny: *Penning discharge in the KATRIN pre-spectrometer*. Journal of Instrumentation, 9(7):P07028, 2014.
- [FHB18] Fränkle, F. M., J. Heizmann, and WJ. Baek: *reproducibility of SDS3 “Christmas Measurement”*. internal KATRIN elog [online], 2018. <https://neutrino.ikp.kit.edu:8080/SDS-Measurements+Phase+3/75>.
- [FHI⁺98] Fukuda, Y, T Hayakawa, E Ichihara, K Inoue, K Ishihara, H Ishino, Y Itow, T Kajita, J Kameda, S Kasuga, *et al.*: *Evidence for oscillation of atmospheric neutrinos*. Physical Review Letters, 81(8):1562, 1998.
- [FK17] Fränkle, F.M. and KATRIN Collaboration: *Background processes in the KATRIN main spectrometer*. Journal of Physics: Conference Series, 888(1):012070, 2017. <http://stacks.iop.org/1742-6596/888/i=1/a=012070>.
- [FLHE14] Fränkle, F. M., J. Linek, S. Hickford, and E. Ellinger: *Radon background with increased pressure and warm baffles*. internal KATRIN elog [online], 2014. <https://neutrino.ikp.kit.edu:8080/SDS-Measurements+Phase+2/51>.
- [FMJ⁺14] Fabian, Marcel, Johannes, Sanshiro, Moritz, and Jan: *BG08.01 Intrinsic FPD Background - 210Pb Investigations*. internal KATRIN elog [online], 2014. <https://neutrino.ikp.kit.edu:8080/SDS-Measurements+Phase+2/9>.
- [Frä06] Fränkle, Florian: *Erste Messungen der elektromagnetischen Eigenschaften des KATRIN Vorspektrometers*. Diploma Thesis, Universität Karlsruhe (TH), 2006. <http://www.katrin.kit.edu/publikationen/dth-fraenkle.pdf>.
- [Frä10] Fränkle, Florian M.: *Background Investigations of the KATRIN Pre-Spectrometer*. PhD thesis, Karlsruher Institut für Technologie (KIT), 2010. <http://nbn-resolving.org/urn:nbn:de:swb:90-193929>.
- [Frä15] Fränkle, Florian: *Default SDS2 analysis parameters*, 2015.
- [Frä17a] Fränkle, F. M.: *Detailed alignment measurements between MS and FPD - part 2*. internal KATRIN elog [online], 2017. <https://neutrino.ikp.kit.edu:8080/SDS-Measurements+Phase+3/63>.
- [Frä17b] Fränkle, F. M.: *FPD background at nominal magnetic field*. internal KATRIN elog [online], 2017. <https://neutrino.ikp.kit.edu:8080/SDS-Measurements+Phase+3/34>.
- [Frä17c] Fränkle, F. M.: *Krypton Decays Inside The Main Spectrometer*. internal KATRIN elog [online], 2017. <https://neutrino.ikp.kit.edu:8080/KryptonJuly17/69>.
- [Frä17d] Fränkle, F. M.: *Radon background with increased pressure and warm baffles*. internal KATRIN elog [online], 2017. <https://neutrino.ikp.kit.edu:8080/SDS-Measurements+Phase+3/64>.

- [Frä17e] Fränkle, F. M.: *SDS3 “Christmas Measurement”*. internal KATRIN elog [online], 2017. <https://neutrino.ikp.kit.edu:8080/SDS-Measurements+Phase+3/67>.
- [Frä17f] Fränkle, Florian: *voltage dependence of background between -18 kV and -19 kV*. internal KATRIN elog [online], 2017. <https://neutrino.ikp.kit.edu:8080/SDS-Measurements+Phase+3/60>.
- [Frä18a] Fränkle, F. M.: *Overview on recent SDS3 measurements*. 34th KATRIN Collaboration Meeting, 2018. <https://fuzzy.fzk.de/bscw/bscw.cgi/d1196073/95-TRP-6413-P3-FFraenkle.pdf>.
- [Frä18b] Fränkle, F. M.: *Persönliche Korrespondenz*. 2018.
- [Frä18c] Fränkle, F. M.: *Residual radon background with both spectrometers and cold baffles*. internal KATRIN elog [online], 2018. <https://neutrino.ikp.kit.edu:8080/SDS-Measurements+Phase+3/80>.
- [FSP⁺08] Firstenberg, O., M. Shuker, R. Pugatch, D. R. Fredkin, N. Davidson, and A. Ron: *Theory of thermal motion in electromagnetically induced transparency: Effects of diffusion, Doppler broadening, and Dicke and Ramsey narrowing*. Phys. Rev. A, 77:043830, Apr 2008. <https://link.aps.org/doi/10.1103/PhysRevA.77.043830>.
- [FTV12] Forero, D. V., M. Tórtola, and J. W. F. Valle: *Global status of neutrino oscillation parameters after Neutrino-2012*. Phys. Rev. D, 86:073012, Oct 2012. <https://link.aps.org/doi/10.1103/PhysRevD.86.073012>.
- [Gal05] Gallagher, Thomas F: *Rydberg atoms*, volume 3. Cambridge University Press, 2005.
- [Gan13] Gando, A. et al. (KamLAND-Zen Collaboration): *Limit on Neutrinoless $\beta\beta$ Decay of ^{136}Xe from the First Phase of KamLAND-Zen and Comparison with the Positive Claim in ^{76}Ge* . Physical Review Letters, 110:062502, 2013.
- [GBB⁺10] Gil, W., J. Bonn, B. Bornschein, R. Gehring, O. Kazachenko, J. Kleinfeller, and S. Putselyk: *The Cryogenic Pumping Section of the KATRIN Experiment*. IEEE Transactions on Applied Superconductivity, 20(3):316–319, 2010.
- [GDL⁺13] Glück, Ferenc, Guido Drexlin, Benjamin Leiber, Susanne Mertens, Alexander Osipowicz, Jan Reich, and Nancy Wandkowsky: *Electromagnetic design of the KATRIN large-volume air coil system*. arXiv preprint arXiv:1304.6569, 2013.
- [Geo15] Georgii, Hans Otto: *Stochastik : Einführung in die Wahrscheinlichkeitstheorie und Statistik*, 2015, ISBN 978-3-11-035970-1; 978-3-11-038686-8. <http://www.degruyter.com/viewbooktoc/product/428666>; <http://dx.doi.org/10.1515/9783110359701>; <https://doi.org/10.1515/9783110359701>.
- [GER16] Gaisser, T.K., R. Engel, and E. Resconi: *Cosmic Rays and Particle Physics*. Cambridge University Press, 2016, ISBN 9781316598436. <https://books.google.de/books?id=nHFNDAAAQBAJ>.
- [GNO10] Glukhov, IL, EA Nekipelov, and VD Ovsiannikov: *Blackbody-induced decay, excitation and ionization rates for Rydberg states in hydrogen and helium atoms*. Journal of Physics B: Atomic, Molecular and Optical Physics, 43(12):125002, 2010.
- [GP12] Giuliani, Andrea and Alfredo Poves: *Neutrinoless double-beta decay*. Advances in High Energy Physics, 2012, 2012.

- [Hae81] Haefer, René A: *Kryo-vakuumtechnik*. Springer, 1981.
- [Har15] Harms, Fabian: *Characterization and Minimization of Background Processes in the KATRIN Main Spectrometer*. PhD thesis, Karlsruher Institut für Technologie (KIT), 2015. <http://nbn-resolving.org/urn:nbn:de:swb:90-500274>.
- [Hax95] Haxton, WC: *The solar neutrino problem*. Annual Review of Astronomy and Astrophysics, 33(1):459–503, 1995.
- [HF15] Harms, F. and F. M. Fränkle: *measurement of intrinsic FPD background at nominal magnetic field*. internal KATRIN elog [online], 2015. <https://neutrino.ikp.kit.edu:8080/SDS-Measurements+Phase+2/174>.
- [Hig64] Higgs, P.W.: *Broken symmetries, massless particles and gauge fields*. Physics Letters, 12(2):132 – 133, 1964, ISSN 0031-9163. <http://www.sciencedirect.com/science/article/pii/0031916364911369>.
- [HKK⁺87] Hirata, K., T. Kajita, M. Koshiba, M. Nakahata, Y. Oyama, N. Sato, A. Suzuki, M. Takita, Y. Totsuka, T. Kifune, T. Suda, K. Takahashi, T. Tanimori, K. Miyano, M. Yamada, E. W. Beier, L. R. Feldscher, S. B. Kim, A. K. Mann, F. M. Newcomer, R. Van, W. Zhang, and B. G. Cortez: *Observation of a neutrino burst from the supernova SN1987A*. Phys. Rev. Lett., 58:1490–1493, Apr 1987. <https://link.aps.org/doi/10.1103/PhysRevLett.58.1490>.
- [HLAE07] Host, O., O. Lahav, B.F. Abdalla, and K. Eitel: *Forecasting neutrino masses from combining KATRIN and the CMB observations: Frequentist and Bayesian analyses*. Physical Review D, 76:113005, 2007.
- [Jam80] James, F: *Interpretation of the shape of the likelihood function around its minimum*. Computer Physics Communications, 20(1):29–35, 1980.
- [Jan15] Jansen, Alexander: *The Cryogenic Pumping Section of the KATRIN Experiment - Design Studies and Experiments for the Commissioning*. PhD thesis, Karlsruher Institut für Technologie (KIT), 2015. <http://nbn-resolving.org/urn:nbn:de:swb:90-471467>.
- [Jil15] Jiles, David: *Introduction to magnetism and magnetic materials*. CRC press, 2015.
- [JK94] Jordanov, Valentin T and Glenn F Knoll: *Digital synthesis of pulse shapes in real time for high resolution radiation spectroscopy*. Nuclear Instruments and Methods in Physics Research Section A: Accelerators, Spectrometers, Detectors and Associated Equipment, 345(2):337–345, 1994.
- [KAT05] KATRIN collaboration: *KATRIN Design Report*. FZKA scientific report, 7090, 2005. <http://bibliothek.fzk.de/zb/berichte/FZKA7090.pdf>.
- [KAT18a] KATRIN Collaboration: *First transmission of electrons and ions through the KATRIN beamline*. arXiv preprint arXiv:1802.04167, 2018.
- [KAT18b] KATRIN Collaboration: *Technical Documents*, 2018. <https://fuzzy.fzk.de/bscw/bscw.cgi/898530>.
- [KBB⁺05] Kraus, C., B. Bornschein, L. Bornschein, J. Bonn, B. Flatt, A. Kovalik, B. Ostrick, E.W. Otten, J.P. Schall, T. Thümmeler, and C. Weinheimer: *Final results from phase II of the Mainz neutrino mass search in tritium β decay*. The European Physical Journal C - Particles and Fields, 40(4):447–468, 2005.
- [Kip17] Kippenbrock, Luke: *Electron peak position during Penning trap measurements*. KATRIN Detector Call, 2017. <https://neutrino.ikp.kit.edu/katrin/images/f/fc/Kippenbrock6Nov2017.pdf>.

- [KL13] King, Stephen F and Christoph Luhn: *Neutrino mass and mixing with discrete symmetry*. Reports on Progress in Physics, 76(5):056201, 2013.
- [Kle14] Kleesiek, Marco: *A Data-Analysis and Sensitivity-Optimization Framework for the KATRIN Experiment*. PhD thesis, Karlsruher Institut für Technologie (KIT), 2014. <http://nbn-resolving.org/urn:nbn:de:swb:90-433013>.
- [KMMS13] Kopp, Joachim, Pedro AN Machado, Michele Maltoni, and Thomas Schwetz: *Sterile neutrino oscillations: the global picture*. Journal of High Energy Physics, 2013(5):50, 2013.
- [Kor17] Korzeczek, Marc: *KATRIN detection efficiency*, 2017.
- [Kor18] Korzeczek, Marc: *Persönliche Korrespondenz*. 2018.
- [KUA⁺08] Kodama, K, N Ushida, C Andreopoulos, N Saoulidou, G Tzanakos, P Yager, B Baller, D Boehnlein, W Freeman, B Lundberg, *et al.*: *Final tau-neutrino results from the DONuT experiment*. Physical Review D, 78(5):052002, 2008.
- [LBB⁺12] Lukić, S, B Bornschein, L Bornschein, G Drexlin, A Kosmider, K Schlösser, and A Windberger: *Measurement of the gas-flow reduction factor of the KATRIN DPS2-F differential pumping section*. Vacuum, 86(8):1126–1133, 2012.
- [Leb10] Leber, Michelle L.: *Monte Carlo Calculations of the Intrinsic Detector Backgrounds for the Karlsruhe Tritium Neutrino Experiment*. PhD thesis, University of Washington, 2010. http://www.npl.washington.edu/sites/default/files/webfiles/theses/MLL_Thesis.pdf.
- [Lei14] Leiber, Benjamin: *Investigations of background due to secondary electron emission in the KATRIN-experiment*. PhD thesis, Karlsruher Institut für Technologie (KIT), 2014. <http://nbn-resolving.org/urn:nbn:de:swb:90-424154>.
- [LP12] Lesgourgues, Julien and Sergio Pastor: *Neutrino mass from cosmology*. Advances in High Energy Physics, 2012, 2012.
- [LU00] Lucas, Larry L and Michael P Unterweger: *Comprehensive review and critical evaluation of the half-life of Tritium*. Journal of research of the National Institute of Standards and Technology, 105(4):541, 2000.
- [M⁺15] Mertens, Susanne *et. al.* (KATRIN Collaboration) *et al.*: *Status of the KATRIN Experiment and Prospects to Search for keV-mass Sterile Neutrinos in Tritium β -decay*. Physics Procedia, 61:267–273, 2015.
- [Maj08] Majorana, Ettore: *Teoria simmetrica dell'elettrone e del positrone*. Il Nuovo Cimento (1924-1942), 14(4):171, Sep 2008. <https://doi.org/10.1007/BF02961314>.
- [Mar80] Marciano, William J: *Neutrino masses: theory and experiment*. Comments Nucl. Part. Phys., 9(DOE-EY-2232B-207):169–184, 1980.
- [MBB⁺12] Mertens, S, A Beglarian, L Bornschein, G Drexlin, F M Fränkle, D Furse, F Glück, S Görhardt, O Krömer, B Leiber, K Schlösser, T Thümmel, N Wandkowsky, and S Wüstling: *Stochastic heating by ECR as a novel means of background reduction in the KATRIN spectrometers*. Journal of Instrumentation, 7(08):P08025, 2012. <http://stacks.iop.org/1748-0221/7/i=08/a=P08025>.
- [McC15] McCutchan, E.A.: *Nuclear Data Sheets for A = 83*. Nuclear Data Sheets, 125:201 – 394, 2015, ISSN 0090-3752. <http://www.sciencedirect.com/science/article/pii/S0090375215000034>.

- [MDF⁺13] Mertens, S., G. Drexlin, F.M. Fränkle, D. Furse, F. Glück, S. Görhardt, M. Hötzel, W. Käfer, B. Leiber, T. Thümmler, N. Wandkowsky, and J. Wolf: *Background due to stored electrons following nuclear decays in the KATRIN spectrometers and its impact on the neutrino mass sensitivity*. *Astroparticle Physics*, 41:52 – 62, 2013, ISSN 0927-6505. <http://www.sciencedirect.com/science/article/pii/S0927650512001892>.
- [Mer12] Mertens, Susanne: *Study of Background Processes in the Electrostatic Spectrometers of the KATRIN experiment*. PhD thesis, Karlsruher Institut für Technologie (KIT), 2012. <http://digbib.ubka.uni-karlsruhe.de/volltexte/1000027058>.
- [MNS62] Maki, Ziro, Masami Nakagawa, and Shoichi Sakata: *Remarks on the unified model of elementary particles*. *Progress of Theoretical Physics*, 28(5):870–880, 1962.
- [MNS⁺07] Masood, Samina S, Salah Nasri, Joseph Schechter, MA Tortola, JWF Valle, and Christian Weinheimer: *Exact relativistic β decay endpoint spectrum*. *Physical Review C*, 76(4):045501, 2007.
- [MP04] Mohapatra, Rabindra N and Palash B Pal: *Massive neutrinos in physics and astrophysics*, volume 72. World scientific, 2004.
- [MPHG17] Mertens, Susanne, Anna Pollithy, Daniel Hilk, and Ferenc Glück: *Rydberg Day*. 2017.
- [MS86] Mikheyev, SP and A Yu Smirnov: *Resonant amplification of ν oscillations in matter and solar-neutrino spectroscopy*. *Il Nuovo Cimento C*, 9(1):17–26, 1986.
- [MSac80] Mohapatra, Rabindra N. and Goran Senjanović: *Neutrino Mass and Spontaneous Parity Nonconservation*. *Phys. Rev. Lett.*, 44:912–915, Apr 1980. <https://link.aps.org/doi/10.1103/PhysRevLett.44.912>.
- [Noe50] Noether, Gottfried Emanuel: *Asymptotic Properties of the Wald-Wolfowitz Test of Randomness*. *The Annals of Mathematical Statistics*, 21(2):231–246, 1950, ISSN 00034851. <http://www.jstor.org/stable/2236903>.
- [OBW06] Otten, E.W., J. Bonn, and Ch. Weinheimer: *The Q -value of tritium β -decay and the neutrino mass*. *International Journal of Mass Spectrometry*, 251(2–3):173–178, 2006.
- [Ost09] Ostrick, Beatrix: *Eine kondensierte $^{83\text{m}}\text{Kr}$ -Kalibrationsquelle für das KATRIN-Experiment*. PhD thesis, Westfälische Wilhelms-Universität Münster, 2009. <http://nbn-resolving.de/urn:nbn:de:hbz:6-91519454708>.
- [Ott94] Otten, E.W.: *The Mainz neutrino mass experiment*. *Progress in Particle and Nuclear Physics*, 32:153 – 171, 1994, ISSN 0146-6410. <http://www.sciencedirect.com/science/article/pii/0146641094900167>.
- [P⁺16] Patrignani, C. *et al.*: *Review of Particle Physics*. *Chin. Phys.*, C40(10):100001, 2016.
- [Par07] Partridge, Robert B: *3K: the cosmic microwave background radiation*, volume 25. Cambridge University Press, 2007.
- [PBB⁺92a] Picard, A, H Backe, H Barth, J Bonn, B Degen, Th Edling, R Haid, A Hermanni, P Leiderer, Th Loeken, *et al.*: *A solenoid retarding spectrometer with high resolution and transmission for keV electrons*. *Nuclear Instruments and Methods in Physics Research Section B: Beam Interactions with Materials and Atoms*, 63(3):345–358, 1992.

- [PBB⁺92b] Picard, A., H. Backe, H. Barth, J. Bonn, B. Degen, Th. Edling, R. Haid, A. Hermanni, P. Leiderer, Th. Loeken, A. Molz, R.B. Moore, A. Osipowicz, E.W. Otten, M. Przyrembel, M. Schrader, M. Steininger, and C. Weinheimer: *A solenoid retarding spectrometer with high resolution and transmission for keV electrons*. Nuclear Instruments and Methods in Physics Research Section B: Beam Interactions with Materials and Atoms, 63(3):345–358, 1992.
- [Pea00] Pearson, Karl: *X. On the criterion that a given system of deviations from the probable in the case of a correlated system of variables is such that it can be reasonably supposed to have arisen from random sampling*. The London, Edinburgh, and Dublin Philosophical Magazine and Journal of Science, 50(302):157–175, 1900. <https://doi.org/10.1080/14786440009463897>.
- [Pea34] Pearson, Karl: *On a New Method of Determining "Goodness of Fit"*. Biometrika, 26(4):425–442, 1934, ISSN 00063444. <http://www.jstor.org/stable/2331988>.
- [PKW64] Pauli, W.E.F., R. Kronig, and V.F. Weisskopf: *Collected scientific papers*. Interscience, New York, NY, 1964. Offener Brief an die Gruppe der Radioaktiven bei der Gauvereinstagung zu Tübingen (datiert 4. Dez. 1930).
- [Pol18] Pollithy, Anna: *Characterizing the residual background in KATRIN*, 2018. https://fuzzy.fzk.de/bscw/bscw.cgi/1196180?op=preview&back_url=1196020.
- [Pon68] Pontecorvo, Bruno: *Neutrino experiments and the problem of conservation of leptonic charge*. Sov. Phys. JETP, 26(984-988):165, 1968.
- [Pov15] Povh, Bogdan: *Particles and Nuclei : An Introduction to the Physical Concepts*, 2015, ISBN 978-366-24632-1-5. <http://swbplus.bsz-bw.de/bsz434884561cov.htm><http://dx.doi.org/10.1007/978-3-662-46321-5>.
- [PW65] Penzias, Arno A and Robert Woodrow Wilson: *A measurement of excess antenna temperature at 4080 Mc/s*. The Astrophysical Journal, 142:419–421, 1965.
- [QV15] Qian, X and P Vogel: *Neutrino mass hierarchy*. Progress in Particle and Nuclear Physics, 83:1–30, 2015.
- [RBS⁺91] Robertson, R. G. H., T. J. Bowles, G. J. Stephenson, D. L. Wark, J. F. Wilkerson, and D. A. Knapp: *Limit on ν_e^- mass from observation of the β decay of molecular tritium*. Phys. Rev. Lett., 67:957–960, Aug 1991. <https://link.aps.org/doi/10.1103/PhysRevLett.67.957>.
- [RCDJ85] Rowley, JK, BT Cleveland, and R Davis Jr: *The chlorine solar neutrino experiment*. In *AIP conference proceedings*, volume 126, pages 1–21. AIP, 1985.
- [Rei97] Reines, F.; Cowan C.: *The Reines-Cowan experiments: Detecting the Poltergeist*, 1997. <http://library.lanl.gov/cgi-bin/getfile?00326606.pdf>.
- [Ren11] Renschler, Pascal: *KESS - A new Monte Carlo simulation code for low-energy electron interactions in silicon detectors*. PhD thesis, Karlsruher Institut für Technologie (KIT), 2011. <http://digbib.ubka.uni-karlsruhe.de/volltexte/1000024959>.
- [RK88] Robertson, Robert Graham Hamish and DA Knapp: *Direct measurements of neutrino mass*. Annual Review of Nuclear and Particle Science, 38(1):185–215, 1988.
- [Rob84] Robins, William P: *Phase noise in signal sources: theory and applications*, volume 9. IET, 1984.

- [Rod12] Rodejohann, Werner: *Neutrinoless double-beta decay and neutrino physics*. Journal of Physics G: Nuclear and Particle Physics, 39(12):124008, 2012.
- [RTBF17] Rodenbeck, C., T. Thuemmler, F. Block, and F. M. Fränkle: *100h+ background run for reference setting*. internal KATRIN elog [online], 2017. <https://neutrino.ikp.kit.edu:8080/SDS-Measurements+Phase+3/38>.
- [SBD⁺13] Slezák, M., S. Bauer, O. Dragoun, M. Erhard, K. Schlösser, A. Špalek, D. Vénos, and M. Zbořil: *Electron line shape of the KATRIN monitor spectrometer*. Journal of Instrumentation, 8(12):T12002, 2013.
- [Sch14] Schwarz, Johannes S.: *The Detector System of the KATRIN Experiment - Implementation and First Measurements with the Spectrometer*. PhD thesis, Karlsruher Institut für Technologie (KIT), 2014. <http://nbn-resolving.org/urn:nbn:de:swb:90-427724>.
- [SS91] Shi, X and David N Schramm: *Solar neutrinos and the MSW effect for three-neutrino mixing*. 1991.
- [SSR⁺13] Schlösser, M., H. Seitz, S. Rupp, P. Herwig, C.G. Alecu, M. Sturm, and B. Bornschein: *In-Line Calibration of Raman Systems for Analysis of Gas Mixtures of Hydrogen Isotopologues with Sub-Percent Accuracy*. Analytical Chemistry, 85(5):2739–2745, 2013.
- [Stu10] Sturm, Michael: *Aufbau und Test des Inner-Loop-Systems der Tritiumquelle von KATRIN*. PhD thesis, Karlsruher Institut für Technologie (KIT), 2010. <http://digbib.ubka.uni-karlsruhe.de/volltexte/1000019355>.
- [Sue15] Suekane, Fumihiko: *Neutrino Oscillations : A Practical Guide to Basics and Applications*, 2015, ISBN 978-443-15546-2-2. <http://swbplus.bsz-bw.de/bsz429162251cov.htm><http://dx.doi.org/10.1007/978-4-431-55462-2>.
- [Thü17] Thümmeler, Thomas: *Status of the Spectrometer and Detector Section*, 2017. <https://fuzzy.fzk.de/bscw/bscw.cgi/d1186202/95-TRP-6307-P2-ThThuemmler.pdf>.
- [Thü18] Thümmeler, Thomas: *Status of the Spectrometer and Detector Section*, 2018. <https://fuzzy.fzk.de/bscw/bscw.cgi/d1195984/95-TRP-6410-P2-TThuemmler.pdf>.
- [TM15] Tipler, Paul Allen and Gene Mosca: *Physik für Wissenschaftler und Ingenieure*, volume [Hauptbd.]: Physik für Wissenschaftler und Ingenieure : [der Begleiter bis zum Bachelor] of *Lehrbuch*. Springer Spektrum, Berlin, 7. dt. aufl. edition, 2015, ISBN 978-3-642-54165-0. <http://swbplus.bsz-bw.de/bsz415641888cov.htm>;http://deposit.d-nb.de/cgi-bin/dokserv?id=4697110&prov=M&dok_var=1&dok_ext=htm;<http://d-nb.info/1052687636/04>, Arbeitsbuch hierzu u.d.T.: Mills, David: Arbeitsbuch zu Tipler/Mosca Physik.
- [Tro15] Trost, N.: *first measurements with pinch and detector magnet at nominal field*. internal KATRIN elog [online], 2015. <https://neutrino.ikp.kit.edu:8080/SDS-Measurements+Phase+2/149>.
- [Tro18] Trost, Nikolaus: *Status of the Rydberg Model*, 2018. https://neutrino.ikp.kit.edu/katrin/images/8/8f/Trost_rydberg_day_final.pdf.
- [Val09] Valerius, Kathrin: *Spectrometer-related background processes and their suppression in the KATRIN experiment*. PhD thesis, Westfälische Wilhelms-Universität Münster, 2009. <http://nbn-resolving.de/urn:nbn:de:hbz:6-28479494638>.

- [Val10] Valerius, K: *The wire electrode system for the KATRIN main spectrometer*. Progress in Particle and Nuclear Physics, 64(2):291–293, 2010.
- [VBN⁺16] Vermul, GT, TJ Bowles, JS Nico, WA Teasdale, DL Wark, JF Wilkerson, BT Cleveland, R Davis Jr, T Daily, K Lande, *et al.*: *JN Abdurashitov, EL Faizov, VN Gavrin, AO Gusev, AV Kalikhov, TV Knodel, II Knysenko, VN Kornoukhov, IN Mirmov, AM Pshukov, AM Shalagin, AA Shikhin, PV Timofeyev, EP Veretenkin, VM*. In *Neutrino 94: Proceedings of the 16th International Conference on Neutrino Physics and Astrophysics, Eilat, Israel, 29 May-3 June 1994*, page 60. Elsevier, 2016.
- [VHB⁺11] Valerius, K, H Hein, H Baumeister, M Beck, K Bokeloh, J Bonn, F Glück, H W Ortjohann, B Ostrick, M Zbořil, *et al.*: *Prototype of an angular-selective photoelectron calibration source for the KATRIN experiment*. Journal of Instrumentation, 6(01):P01002, 2011.
- [Wal15] Waldi, Roland: *Statistische Datenanalyse : Grundlagen und Methoden für Physiker*, 2015, ISBN 978-366-24714-5-6. <http://swbplus.bsz-bw.de/bsz433316632cov.htm><http://dx.doi.org/10.1007/978-3-662-47145-6>.
- [Wan13] Wandkowsky, Nancy: *Study of background and transmission properties of the KATRIN spectrometers*. PhD thesis, Karlsruher Institut für Technologie (KIT), 2013. <http://digbib.ubka.uni-karlsruhe.de/volltexte/1000036631>.
- [WBB⁺87] Wilkerson, J. F., T. J. Bowles, J. C. Browne, M. P. Maley, R. G. H. Robertson, J. S. Cohen, R. L. Martin, D. A. Knapp, and J. A. Helfrich: *Limit on $\bar{\nu}_e$ Mass from Free-Molecular-Tritium Beta Decay*. Phys. Rev. Lett., 58:2023–2026, May 1987. <https://link.aps.org/doi/10.1103/PhysRevLett.58.2023>.
- [WDF⁺13] Wandkowsky, N., G. Drexlin, F.M. Fränkle, F. Glück, S. Groh, and S. Mertens: *Validation of a model for radon-induced background processes in electrostatic spectrometers*. Journal of Physics G: Nuclear and Particle Physics, 40(8):085102, 2013.
- [Wei67] Weinberg, Steven: *A Model of Leptons*. Phys. Rev. Lett., 19:1264–1266, Nov 1967. <https://link.aps.org/doi/10.1103/PhysRevLett.19.1264>.
- [Wen10] Wendell, R. et al. (Super-Kamiokande Collaboration): *Atmospheric neutrino oscillation analysis with subleading effects in Super-Kamiokande I, II, and III*. Physical Review D, 81:092004, 2010.
- [Wik06] Wikipedia: *Standard Model of Elementary Particles*. 2006. https://en.wikipedia.org/wiki/Standard_Model#/media/File:Standard_Model_of_Elementary_Particles.svg, [Online; accessed 04-December-2017].
- [Wik17] Wiki, KATRIN: *Resources — KATRIN Wiki*, 2017. <https://neutrino.ikp.kit.edu/katrin/index.php?title=Resources&oldid=8630>, [Online; accessed 13-January-2018].
- [Wol78] Wolfenstein, Lincoln: *Neutrino oscillations in matter*. Physical Review D, 17(9):2369, 1978.
- [Wol09] Wolf, J.: *Size Matters: The Vacuum System of the KATRIN Neutrino Experiment*. Journal of the Vacuum Society of Japan, 52(5):278–284, 2009.
- [Wol10] Wolf, Joachim et. al. (Katrin Collaboration): *The KATRIN neutrino mass experiment*. Nuclear Instruments and Methods in Physics Research Section A:

- Accelerators, Spectrometers, Detectors and Associated Equipment, 623(1):442–444, 2010.
- [WW40] Wald, Abraham and Jacob Wolfowitz: *On a test whether two samples are from the same population*. The Annals of Mathematical Statistics, 11(2):147–162, 1940.
- [WW43] Wald, A. and J. Wolfowitz: *An Exact Test for Randomness in the Non-Parametric Case Based on Serial Correlation*. The Annals of Mathematical Statistics, 14(4):378–388, 1943, ISSN 00034851. <http://www.jstor.org/stable/2235925>.
- [Zub98] Zuber, Kai: *On the physics of massive neutrinos*. Physics Reports, 305(6):295–364, 1998.
- [Zub12] Zuber, Kai [VerfasserIn]: *Neutrino physics*, [2012], ISBN 978-1-283-30928-8; 978-1-4200-6472-8. <http://lib.myilibrary.com?id=330928>.

Acknowledgements

Herzlichen Dank an alle, die mich beim Entstehen dieser Arbeit in der vorliegenden Fassung unterstützt und diese erst möglich gemacht haben. Mein besonderer Dank gilt

- Prof. Dr. G. Drexlin für die Möglichkeit, dass ich meine Masterarbeit im spannenden und abwechslungsreichen Umfeld des KATRIN Experiments schreiben durfte und für jegliche Unterstützung in dieser Zeit.
- Prof. Dr. G. Quast dafür, dass er freundlicherweise das Korreferat dieser Arbeit übernommen hat.
- Dr. Florian Fränkle für die ausgezeichnete wissenschaftliche Betreuung der Arbeit, die hilfreichen Erklärungen bei Problemen aller Art sowie das Korrekturlesen meiner Arbeit.
- Moritz Machatschek für die Einführung- und Vertiefungskurse in KaFit, die zahlreichen Hilfestellungen in Sachen Programmierung, für die Korrektur meiner Texte und die lustigen Monate im gemeinsamen Büro in der Anfangszeit.
- Dr. Fabian Harms für die sehr gute und sympathische Betreuung in den ersten sechs Monaten der Masterarbeit sowie das offene Ohr für Probleme aller Art.
- Prof. Dr. Sanshiro Enomoto and Marc Korzeczek for the introduction to detector systematics, the provision of simulations and the ideas relating the quantification of the systematic uncertainties of rate estimation.
- Kathrin Valerius, Susanne Mertens, Caroline Rodenbeck, Jan Behrens, Marco Deffert, Wonqook Choi, Thomas Thümmeler und Ferenc Glück stellvertretend für das gesamte Analysis-Team für die wertvollen wissenschaftlichen Diskussionen.
- Woo-Jeong Baek für die angenehme gemeinsame Zeit im Büro, die Einführung in das wissenschaftliche Englisch und die sprachlichen Korrekturen.
- Hendrik Seitz-Moskaliuk für die LaTeX-Tipps und für das zuverlässige Eintreiben von ausstehendem Kuchen.
- Der gesamten KATRIN-Gruppe für die gemeinsame Arbeit und die anregenden Diskussionen, sowie die schöne Zeit beim Mittagessen, den Freitagseminaren oder auf Konferenzen und Workshops.

Ein weiteres Dankeschön gilt meinen Eltern Ellen und Thomas Block, die mir das Physik-Studium ermöglicht, mir in allen Situationen den Rücken gestärkt und mich immer unterstützt haben. Des Weiteren möchte ich mich bei meinem Bruder Lukas Block für die Tipps beim Programmieren sowie für die Hilfestellungen beim Verfassen dieser Arbeit bedanken. Ein besonderes Dankeschön geht an meine Freundin Nadine Kloss, die meine anstrengenden Launen während der Schreibphase ertragen musste und es immer wieder geschafft hat, mich aufzumuntern.